2016

Model Nanocatalysts with Tunable Reactivity: Tailoring the Structure and Surface Chemistry of Nanomaterials for Energy and Alternative Fuels Catalysis

Hemma Mistry
University of Central Florida

MODEL NANOCATALYSTS WITH TUNABLE REACTIVITY: TAILORING THE STRUCTURE AND SURFACE CHEMISTRY OF NANOMATERIALS FOR ENERGY AND ALTERNATIVE FUELS CATALYSIS

by

HEMMA MISTRY

B.S. University of California, Berkeley, 2010

A dissertation submitted in partial fulfillment of the requirements
for the degree of Doctor of Philosophy
in the Department of Physics
in the College of Sciences
at the University of Central Florida
Orlando, Florida

Fall Term
2016

Major Professor: Beatriz Roldan Cuenya

ABSTRACT

One of the most pressing challenges of our time is meeting growing global energy demands while limiting human impact on the environment. To meet this challenge, new catalysts are needed to enable carbon neutral energy production processes and low cost synthesis of alternative fuels. In order to design new catalysts for such processes, fundamental understanding is needed on how the structural and chemical properties of nanostructured materials influences their surface chemistry. In this dissertation, I explore how the properties of nanoparticles, such as particle size, shape, composition, and chemical state, can be used to tune their reactivity. For this work, model nanoparticles were synthesized with well-defined structural and chemical properties, and a variety of surface science approaches were used for catalyst characterization. In particular, emphasis was placed on understanding the changes which may occur in the catalyst structure and chemical state during a reaction using advanced *in situ* techniques and correlating these changes to reactivity. After exploring how nanostructuring the catalyst surface can be used to tune reactivity and how dynamic changes can occur to nanocatalysts in reactive environments, these general principles are applied to a model reaction, the electroreduction of carbon dioxide, which is a promising process for synthesizing valuable products using renewable energy while consuming waste carbon dioxide. I explore the mechanisms behind how catalyst particle size, composition, and oxidation state can be used to improve activity and tune selectivity towards different carbon dioxide reduction products. Such fundamental mechanistic insights are critically needed to design efficient catalysts for this reaction.

ACKNOWLEDGMENTS

I would like to thank my advisor, Professor Beatriz Roldan Cuenya for her support and her confidence in me throughout my PhD. I feel lucky to have been one of her students, and working with her for the last five years has transformed my career. I would also like to thank my coworkers in the Roldan group both at UCF and Ruhr-University Bochum for their friendship and guidance. Also, I am grateful to the technical staff that supported me and helped make this work possible. I also acknowledge the collaborators who contributed to the work in this dissertation and beamline support staff who assisted with the synchrotron measurements.

Finally, I am deeply grateful to my family, who have supported me throughout my career, and my partner for his continued love and respect.

TABLE OF CONTENTS

LIST OF FIGURES

LIST OF TABLES

LIST OF ABBREVIATIONS

2D	2 dimensional
3D	3 dimensional
AFM	Atomic force microscopy
AP-XPS	Ambient pressure X-ray photoelectron spectroscopy
CO_2RR	CO_2 electroreduction reaction
CN	Coordination number
CV	Cyclic voltammetry
DFT	Density functional theory
EDS	Energy dispersive X-ray spectroscopy
EXAFS	Extended X-ray absorption fine structure
FCC	Face centered cubic
FIB	Focused ion beam
FID	Flame ionization detector
GC	Gas chromatography
HAADF	High angle annular dark field
HER	Hydrogen evolution reaction
HERFD	High energy resolution fluorescence detection
HOPG	Highly oriented pyrolytic graphite
HPLC	High performance liquid chromatography
HRTEM	High resolution transmission electron microscopy
HSA	Hemispherical electron energy analyzer

IMFP	Inelastic mean free path
KE	Kinetic energy
LSV	Linear sweep voltammetry
MCD	Multichannel detector
ML	Monolayer
NHE	Normal hydrogen electrode
NP	Nanoparticle
OER	Oxygen evolution reaction
OLEMS	On-line electrochemical mass spectrometry
ORR	Oxygen reduction reaction
P2VP	Poly(2-vinylpyridine)
PDS	Potential determining step
PS	Polystyrene
RHE	Reversible hydrogen electrode
RT	Room temperature
SAED	Selected area electron diffraction
SEM	Scanning electron microscopy
SHE	Standard hydrogen electrode
STEM	Scanning transmission electron microscopy
TCD	Thermal conductivity detector
TEM	Transmission electron microscopy
TPD	Temperature programmed desorption

UHV	Ultra high vacuum
VOC	Volatile organic compound
XAFS	X-ray absorption fine structure
XANES	X-ray absorption near edge structure
XPS	X-ray photoelectron spectroscopy

CHAPTER ONE: INTRODUCTION

Motivation

One of the most pressing challenges for science and technology in our time is to meet growing demands for energy and fuels in a sustainable and economical manner. Advancements in catalytic chemical conversion are needed not only to more efficiently utilize our limited supply of fossil fuel feedstocks, but to reduce our reliance on these sources through the efficient synthesis and conversion of alternative fuels. Many promising catalytic reactions are being explored which could enable a carbon-neutral energy economy, for example, catalytic water splitting to generate H_2 feedstock for fuel cells, and the photo- or electro-catalytic conversion of CO_2 to liquid fuels powered by renewable energy. However, to realize these technologies on an industrial scale, catalysts are still needed which are inexpensive and energy efficient. Basic knowledge is lacking into fundamental reaction mechanisms and processes which occur at the complex nanoscale surface of these catalysts. These are difficult problems to approach, since a catalyst surface may contain a variety of active sites at which molecules can react, and these may evolve during a reaction. Furthermore, many of these catalytic processes occur under conditions such as high pressure, high temperature, or in the presence of a solvent, making it a challenge to measure a working catalyst using conventional surface characterization techniques in realistic conditions. To make strides forward in this direction, advances in atom-precise catalyst engineering are needed, along with advanced methods for time- and space- resolved *operando* characterization of a catalyst in its working state. The ultimate goal is the design of new catalysts for clean energy production whose reactivity can be controllably tuned through precise alteration of their structure and surface chemistry. In this dissertation, I explore how structural properties

can be used to tune reactivity in model catalysts and how these catalysts evolve under realistic reaction conditions, and I apply these principles to develop catalysts with tunable activity and selectivity for the CO_2 electroreduction reaction.

Mechanisms behind Nanocatalyst Reactivity

In the last few decades, tremendous progress has already been made in understanding how the nanoscale structural and surface chemical properties of catalyst particles affect their reactivity.[1] A well-studied structural parameter for many reactions is the influence of nanoparticle (NP) size. Changing the NP size will alter the population of terrace, edge, or corner sites at the catalyst surface, and in general, lower coordinated sites will bind more strongly to reactants, influencing the activity and selectivity of a reaction.[2-4] For very small particles, e.g. for Au NPs below 2.7 nm in size,[5] quantum size effects may play a role, in which the electronic structure of the surface atoms is confined, leading to non-metallic behavior.[6] For larger NPs, new synthesis techniques have allowed the synthesis of shape-selected NPs in which the type of surface facets can control reactivity.[7-10] The study of shape-dependence for smaller, nanometer sized NPs is much more challenging due to difficulties in not only synthesizing but also resolving shapes at this length scale. In Part I of this thesis, I present a study of the shape-dependent reactivity of sub-nanometer Pt NPs with well-defined shape resolved using advanced characterization techniques.[11]

Another structural parameter which must be considered is the NP-support interaction. The support can play a critical role in stabilizing the structure of metal NPs, since strongly interacting supports may prevent NPs from sintering during a reaction. This is a critical consideration for carbon-supported electrocatalysts, since carbon interacts weakly with metal

NPs which may allow them to sinter during a reaction, and the carbon supports themselves may degrade under corrosive conditions such as those needed for the oxygen evolution reaction. The support interaction may also stabilize particular NP shapes.[12] For example, a strong interaction between the metal and support may stabilize a 2D NP shape, and when this interaction is weakened, i.e. by chemisorbed molecules on the NP, the NP shape may evolve to become 3D.[13,14] Other phenomena which can occur when a metal NP interacts with its support include charge transfer, spillover of reactants, or encapsulation of the NP by the support, all of which can play a critical role in nanocatalyst reactivity.[15]

Many catalysts are composed of more than one metal element, which adds a further layer of complexity to their behavior. Adding a secondary metal to a NP may alter its reactivity through a ligand, or electronic effect, in which alloying with neighboring atoms of a different element changes the electronic properties of a metal atom in the NP.[16-18] Another mechanism behind compositional effects on reactivity is geometrical effects, i.e. the arrangement of the two different metals within the NP. One such geometrical effect is strain, in which the lattice parameter of the host metal is altered by introducing different metal atoms with a different lattice constant. According to the d-band model, compressive strain induces a down-shift in the d-band center of a transition metal, weakening its interaction with adsorbates, while expansive strain has the opposite effect.[16,19,20] The d-band center has proved to be a powerful descriptor for explaining and predicting changes in reactivity for model systems,[21,22] particularly epitaxially deposited layers which are under strain.[23,24] However, care must be taken since in some instances for model systems, shifts in the d-band center predicted by the theory do not agree with those measured experimentally.[25] Another geometric effect, known at the “ensemble effect”, involves

the creation of active sites at the surface by isolating active centers of the host metal by dilution with an inactive secondary metal.[26-29] In this scenario, unwanted side reactions which occur on extended surfaces of the host metal are terminated, improving selectivity to a desired reaction which only occurs on isolated sites of the host metal. Alternatively, bimetallic catalysts may have improved behavior due a bifunctional mechanism, in which the secondary metal acts independently to provide an alternative active site, perhaps facilitating a different reaction step than the host metal atoms.[30] These mechanisms behind composition-dependent reactivity will depend strongly on the compositional structure of the catalyst, for example if the catalyst is an alloy with randomly mixed metal atoms, a well-ordered intermetallic structure, a core-shell structure with different shell thicknesses, or a NP containing grains of different metals.

Dynamical Changes in Working Catalysts

Not only do the size, shape, support and composition of the catalyst correlate strongly with each other to influence reactivity, but these parameters may change drastically under reaction conditions. Despite efforts to synthesize nanostructures with well-defined properties, it must always be considered that the properties may evolve under different environments. Such changes can include changes in NP size through sintering,[31-35] evolution of the NP shape,[13,14] changes in the oxidation state of the surface,[36-39] or compositional restructuring in bimetallic catalysts.[40-42] To resolve such changes, it is critical to use characterization techniques for measuring a catalyst *in situ* or *operando* during a reaction. Furthermore, the measurements must be time-resolved, to capture the evolution of the catalyst over the course of a reaction, and measurements should be performed at different length scales, to capture changes at the nanoscale, at the mesoscale, on the surface and throughout the bulk of the catalyst. Ideally,

online measurements of the reaction activity and selectivity should also be performed to correlate the parameters of the working catalyst with its reactivity. Advances in synchrotron-based X-ray spectroscopy methods such as X-ray absorption fine structure (XAFS) and X-ray photoelectron spectroscopy (XPS) have allowed great breakthroughs in the characterization of catalysts under working conditions. This dissertation explores the chemisorption or reaction-driven dynamic changes which can occur in model nanocatalysts using *in situ* and *operando* synchrotron techniques. In Chapters 4 and 7, I show how XAFS can be used to monitor structural and electronic changes in catalysts under realistic environments using *in situ* reaction cells. Also, in Chapter 6, I present an ambient pressure XPS (AP-XPS) study of segregational trends in bimetallic catalysts under reactive environments.

CO_2 Electroreduction – A Model Reaction

As part of the search for new clean energy technologies, a reaction that has been of emerging interest in recent years is the electroreduction of CO_2. CO_2 conversion is of high interest since recycling waste CO_2 from current industrial processes could help to close the carbon cycle, and valuable high energy density products such as alcohols can potentially be synthesized from the reduction of CO_2. However, CO_2 is an extremely stable molecule, and efficient catalysts are needed to make CO_2 conversion an energy efficient process. The electrocatalytic reduction of CO_2 would be an ideal process, since it could be powered by renewable, intermittent energy sources such as wind and solar, it occurs under mild conditions (ambient pressure and temperature), and it can be carried out in aqueous electrolyte, and unlike the thermochemical process, it does not require H_2 as a feedstock. However, in order to make this reaction viable, more efficient, stable, and inexpensive catalysts working at lower

overpotentials are needed. Copper has received the most attention as a metal catalyst for this reaction, since it is the only metal which has appreciable selectivity towards hydrocarbon products, however high overpotentials are needed to run the reaction, and problems exist with catalyst stability.[43,44] In order to develop new catalysts for this reaction, fundamental knowledge is needed on how the basic structural and chemical properties of CO_2 electroreduction catalysts can be used to tune their reactivity.

This dissertation explores how tailoring the structural and chemical properties of a nanocatalyst surface can be used to tune its reactivity and uses CO_2 electroreduction as a model reaction to demonstrate these principles. Chapter 2 describes the methods used, including the colloidal synthesis of model nanoparticles with controlled shape and size, and their characterization using surface science and synchrotron techniques. Next, Part I of the dissertation focuses on the size- and shape-dependent reactivity of Pt NPs supported on γ-Al_2O_3 for heterogeneous reactions. Chapter 3 describes how NP size and shape can determine the reactivity of these catalysts for 2-butanol oxidation, while Chapter 4 shows how these NPs may undergo a dynamic shape transformation under a realistic high pressure H_2 environment. In Part II of this dissertation, I explore how NP size, composition, and chemical state can be used to tune the reactivity of nanostructures to achieve more active, selective, and stable catalysts for CO_2 electroreduction. Chapter 5 explores size effects for both Au NPs and Cu NPs, demonstrating the critical dependence of CO_2 electroreduction on NP size. Chapter 6 focuses on AuCu bimetallic NPs, showing how their reactivity depends on both size and composition, and that segregation and structural rearrangement play a critical role in the reactivity of these bimetallic catalysts. Finally, Chapter 7 explores how the nanostructure and oxidation state of Cu catalysts can be tune

to achieve high CO_2 electroreduction efficiency for a valuable product, ethylene. This dissertation provides key insights into using nanocatalyst size, shape, composition, and oxidation state to tailor the reactivity of nanostructured materials. These insights are critical for the design of new nanomaterials for energy and alternative fuels catalysis.

CHAPTER TWO: EXPERIMENTAL METHODS

Colloidal Synthesis

In order to study the influence of nanostructural parameters such as size, shape, composition, or oxidation state on catalytic reactivity, a requirement is the use of well-defined, model NPs. Several well-established techniques exist for synthesizing monodisperse NPs, such as the use of cluster sources with mass selection[45-47] or colloidal methods.[48-50] In the studies presented here, an inverse micelle encapsulation technique employing diblock copolymers was used. This technique allows a particularly high degree of control over NP properties such as size, shape, dispersion, and composition, and in particular, it allows for synthesis of very small nanostructures below 1 nm in size. It is also facile and can be used for different metals and support materials, making it versatile for different catalytic applications.

In this technique, diblock copolymers are used to form inverse micelles in solution, which act as nanoreactors for the formation of metal nanoparticles. Specifically, poly(styrene-b-2-vinyl pyridine) (PS-b-P2VP) is used, in which the P2VP end is hydrophilic and the PS end is hydrophobic. When dissolved in a non-polar solvent such as toluene, the P2VP ends form nano-cages with uniform size. After dissolution of the polymers in toluene, metal salts are added to the solution and stirred for several days. The metal ions fill the core of the micelles by coordinating to the P2VP groups. The ratio of the number of metal atoms in solution to the number of P2VP groups (referred to as the loading) can be varied in order to change the size of the resulting nanoparticles. In addition, more than one metal salt can be added to create bimetallic NPs with a desired ratio of the two metals.

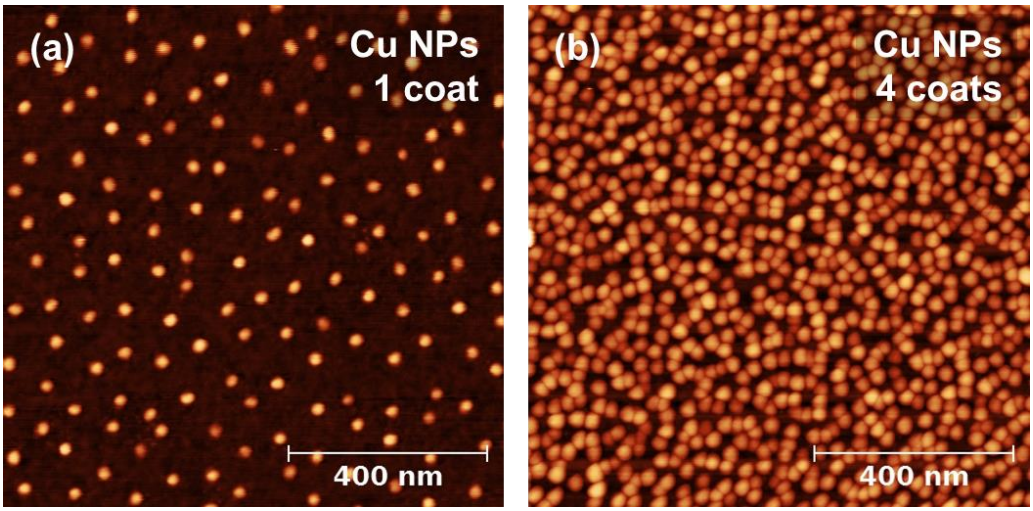

Figure 1. Cu NPs synthesized via inverse micelle encapsulation using PS-P2VP diblock copolymers dipcoated onto a silicon wafer, resulting in a monolayer of monodisperse, hexagonally arranged NPs. (a) One coat of Cu NPs after O_2 plasma treatment to remove polymers, and (b) four coats of Cu NPs, with O_2 plasma treatment after each coat.

After preparation, the metal-loaded micelles can be deposited onto planar supports by dipcoating. Due to the interaction between PS ends of the polymers, the micelles hexagonally arrange on the support resulting in an array of uniformly sized and spaced structures, as shown in Figure 1. The molecular weight of the PS end of the polymer can be varied in order change the interparticle spacing. In addition, the substrate can be dipcoated multiple times, which reduces the interparticle distance while maintaining a monolayer coverage, see Figure 1. Alternatively, to synthesize powder supported catalysts, the micelle solution can be deposited on the support via wet impregnation. After deposition, the polymers can be removed using O_2, H_2, or N_2 plasma, leaving the metal NP surface bare and available for reactivity studies. The plasma treatments can be chosen to tune the chemical state of the resulting metal nanoparticles. While O_2 plasma

removes the polymer most efficiently, N_2 or H_2 plasmas can be used to avoid damaging carbon support materials such as HOPG or carbon foil. N_2 plasma can furthermore be used to introduce N doping into carbon support materials, which is known to improve electrochemical reactivity for some reactions.[51-54]

Atomic Force Microscopy

AFM was used to characterize the morphology of the micellar NPs used in this dissertation. AFM is a scanning probe technique in which a sharp probe interacts with the surface of the sample, and the forces between the probe and sample are measured. Different forces may exist between the probe and sample, for example, magnetic, electrostatic, or torsional forces, all of which may be probed using AFM to gain information on the surface properties of the sample. In this dissertation, to measure the surface morphology, the van der Waals force is measured. Figure 2a shows the forces which exist when the probe is brought within about 20 nm of the sample surface, and also indicated are the common AFM modes of operation. In non-contact mode, the probe does not make contact with the surface, which is ideal for delicate samples or for probing longer range forces. However, in this mode measurements may be affected by the thin water layer which exists on surfaces under ambient conditions which causes the tip to stick to the sample surface. In contact mode, the probe is brought close to the sample within the range where strong repulse forces exist. Due to the strong interaction between the tip and sample, this mode may cause damage to delicate samples. The third mode is tapping mode, in which the probe makes intermittent contact with the surface, which allows for measuring the surface with higher resolution and without sticking or causing damage.

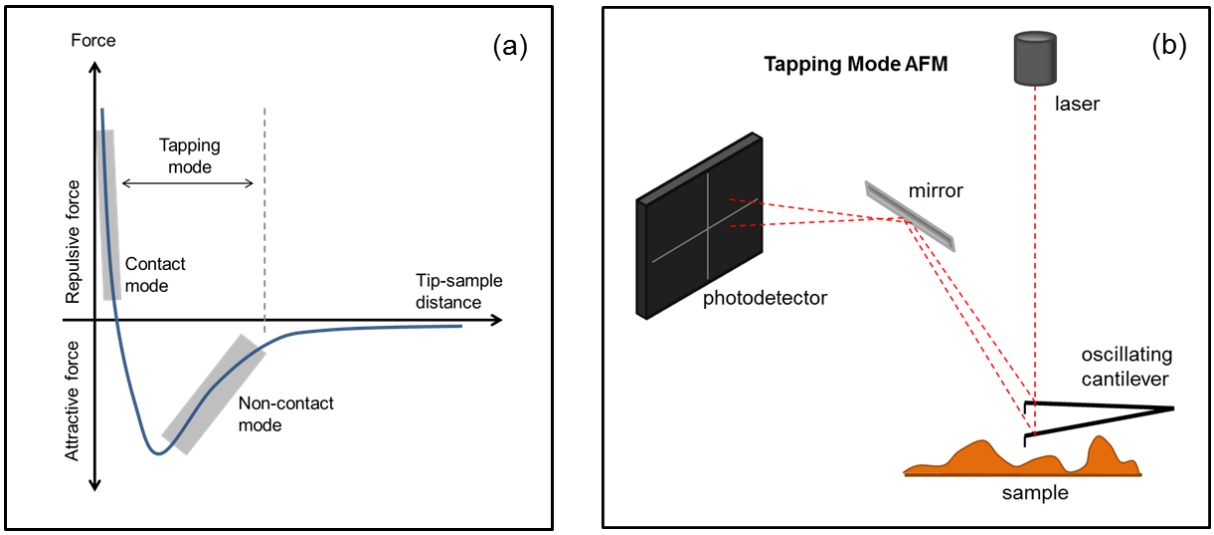

Figure 2. (a) Van der Waals force curve, and measurement regions for different modes of AFM. (b) Schematic of tapping mode AFM. A laser is directed onto an oscillating cantilever. The tip of the cantilever taps the sample surface, and forces between the tip and sample cause a change in the amplitude of oscillation of the cantilever. The laser is reflected from the cantilever onto a mirror, then to a four quadrant photodetector.

Figure 2b shows a schematic of the basic operation of tapping mode AFM. The probe is attached to a flexible cantilever, which is driven by a piezo close to its resonant frequency. A laser reflects from the back of the cantilever and onto a four quadrant photodetector. The signal from the detector is fed to a computer. As the probe is scanned across the sample surface, it interacts with the surface and changes the amplitude of oscillation of the cantilever. This change is detected by the photodetector and controls a feedback loop, which adjusts the z position of the cantilever to maintain the original amplitude. The changes in z position of the cantilever give the changes in height of features on the sample surface. It should be kept in mind that the AFM probe has a finite width, around 8 nm for the probes used in this dissertation (Aspire CT-300).

Since the width of the AFM tip will be convoluted with the width of features on the sample, the lateral resolution of AFM images is poor. However, since only the very tip of the AFM probe interacts with the sample surface, the height resolution is more accurate.

X-Ray Photoelectron Spectroscopy

XPS is a surface sensitive technique that can provide quantitative information on the elemental composition and chemical state of a sample. The working principle of XPS is based on the photoelectric effect. X-rays with a fixed energy $h\nu$ (1486.6 eV for an Al Kα source) are irradiated on a sample and can excite core electrons. The kinetic energy (E_{KE}) of these photoelectrons is measured and can be used to determine the binding energy (E_{BE}) of the ejected photoelectrons according to

$$E_{KE} = h\nu - E_{BE} - \phi_{Analyzer}\,, \tag{1}$$

where $\phi_{Analyzer}$ is the work function of the electron energy analyzer. Figure 3 shows a schematic of this process. The binding energies of the detected photoelectrons can be referenced to known values for each element to determine the composition of the sample.

The peaks in XPS spectra are labelled using spectroscopic notation as nl_j, where n is the principle quantum number (n = 1, 2, 3…), l is the orbital angular momentum (s = 0, p = 1, d = 2, f = 3), and j is the total angular momentum ($j = |l + s|, s = \pm\frac{1}{2}$). Due to the spin-orbit interaction, p, d, and f electrons are split into two energy levels (e.g. $2p_{1/2}$ and $2p_{3/2}$, as shown in Figure 3) and will appear as a doublet in the XPS spectrum. The binding energy difference between the two peaks is known as the spin-orbit splitting. The areas of the peaks in the doublet will depend on the number of electrons that can occupy each level. For example, two electrons

will be in the $2p_{1/2}$ state and four will be in the $2p_{3/2}$ state, so the ratio between the two areas will be 1:2, while for the $3d_{3/2}$ and $3d_{5/2}$ state, the ratio would be 2:3.

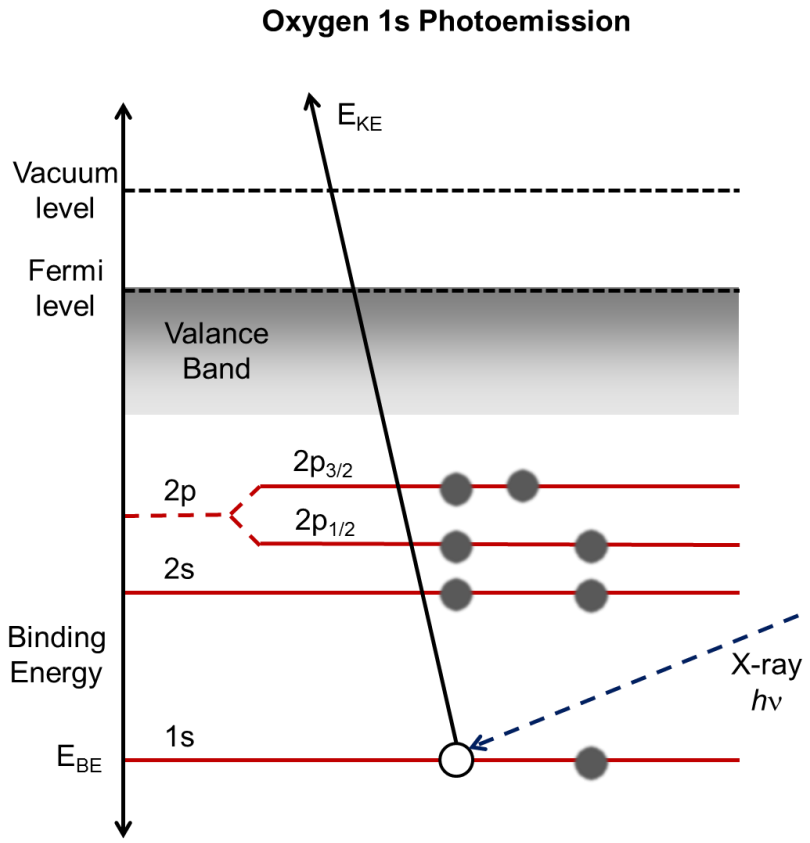

Figure 3. Schematic of photoelectron excitation during XPS. X-rays irradiate the sample and excite core level photoelectrons, whose kinetic energy is detected by the analyzer. The spectroscopic notation used in XPS is indicated.

In addition to the elemental composition, information can be gained on the chemical state of the surface using XPS. When an element exists in a different oxidation state, the XPS peaks will be shifted in binding energy due to the reduction of screening of the nucleus by the missing

electrons. Shifts will also be caused by the bonding environment, for example, shifts in the carbon 1s peak will be measured due to bonding between C and O. Quantitative information can be determined on the chemical state of the sample by comparing these shifts with reference values. When measuring NPs, it should also be kept in mind that binding energy shifts may exist which depend on particle size due to initial and final state effects.[55-58] Finally, artificial binding energy shifts may exist due to differential charging as electrons are depleted from the surface, and care must be taken to avoid this by properly grounding the sample. For insulating samples, an electron flood gun can be used to supply electrons to the sample surface.

In this dissertation, lab-based XPS measurements were performed in an ultra-high vacuum (UHV) chamber with base pressure 2×10^{-10} mbar pressure. The chamber is equipped with an X-ray source providing Al Kα radiation (1486.6 eV) and a monochromator containing an ellipsoidal quartz crystal mirror which narrows the width of the energy distribution and focuses the X-ray beam for high energy resolution measurements and smaller spot size. The photoelectrons from the sample are detected by a hemispherical electron energy analyzer (HSA). Before the analyzer is a lens system, which collects the electrons, retards their velocity, and focuses them onto a slit to the analyzer. The electrons then travel around the HSA, across which an electric field is applied so that only electrons with a particular kinetic energy (pass energy) can reach a specific position on the opposite side of the hemisphere. Here the electrons are detected at a multichannel detector (MCD), containing several channeltrons which multiply the signal from the detected electrons. To measure a spectrum, the lens system voltages are scanned to collect electrons with different kinetic energies and retard their energy to meet the HSA pass energy.

XPS measurements can also be performed using synchrotron X-rays for higher resolution and higher intensity measurements. In addition, the energy of the synchrotron X-rays is easily tunable, which allows photoelectrons with different escape depth from the sample to be measured. Recently, the capability to perform synchrotron XPS measurements under ambient gas conditions has been developed, such as the setup at beamline X1A1 at the National Synchrotron Light Source (NSLS I) at Brookhaven National Laboratory (BNL). In this system, up to 1 Torr of gas can be introduced to the measurement chamber during XPS acquisition. In order to protect the detector, which requires UHV conditions, differential pumping is added to the lens system to reduce the pressure before the detector. Also, to reduce scattering of the photoelectrons in the gas atmosphere, the distance between the sample and the lens system entrance is kept small.

X-Ray Absorption Fine Structure Spectroscopy

Another X-ray spectroscopy technique used in this dissertation is X-ray absorption fine structure spectroscopy (XAFS). XAFS is a synchrotron-based technique which can be used to probe the local structure and chemical state of atoms of a particular element in a catalyst. In this method, monochromatic X-rays are irradiated on the sample and scanned in energy around the binding energy of a core electron of a particular element. As in XPS, the X-rays may excite photoelectrons when they exceed the binding energy of this electron. However, in XAFS, the emitted photoelectrons are not measured, but the X-rays which are transmitted through the sample (or which fluoresce from the sample) are measured in order to derive the absorption coefficient. For XAFS measured in transmission, the absorption coefficient is derived according to Beer's law:

$$I_t = I_0 e^{-\mu t} \ , \tag{2}$$

where I_0 is the intensity of the incident X-rays, I_t is the intensity of the transmitted X-rays, and t is the thickness of the sample.

Figure 4(a) shows the absorption coefficient $\mu(E)$ as a function of X-ray energy for a Ag foil measured at the Ag K edge. An edge jump can be seen when the X-ray reaches the binding energy of the core electron, E_0. The region of the spectrum around E_0 is known as the X-ray absorption near edge structure (XANES) region, and the shape of the oscillations can be compared to reference data to determine the oxidation state and coordination geometry of the absorbing atom. The extended X-ray absorption fine structure spectroscopy (EXAFS) region is also marked in Figure 4(a). In this region beyond the edge, small oscillations exist in the XAFS spectrum. These oscillations are due to constructive and destructive interference between the outgoing photoelectron wave and the wave which backscatters off neighboring atoms. This interference influences the probability of the transition taking place and results in oscillations in the absorption coefficient. These oscillations contain information about the number of neighboring atoms to the absorbing atom, the type of neighbors (which element), and the distance to them, all of which can be extracted through careful data analysis.

Figure 4 gives an overview of how EXAFS data is extracted and analyzed. In order to isolate the EXAFS oscillations, $\chi(E)$, a smooth background function $\mu_0(E)$ which represents the absorption spectrum of an isolated atoms with no neighbors must be subtracted from the data, and the data is normalized to go from 0 to 1 by dividing by the edge jump $\Delta\mu_0(E)$:

$$\chi(E) = \frac{\mu(E) - \mu_0(E)}{\Delta\mu_0(E)} \tag{3}$$

The Athena software was used in this dissertation to calculate and subtract the isolated atom background function. A smooth pre-edge and post-edge line (marked in Figure 4(a)) must be

defined for this calculation. One calculated, $\chi(E)$ can be plotted in *k* space ($k = \sqrt{\frac{2m(E-E_0)}{\hbar^2}}$) as shown in Figure 4(b) and is usually weighted by k^2 in order to emphasize the weaker oscillations at high *k*.

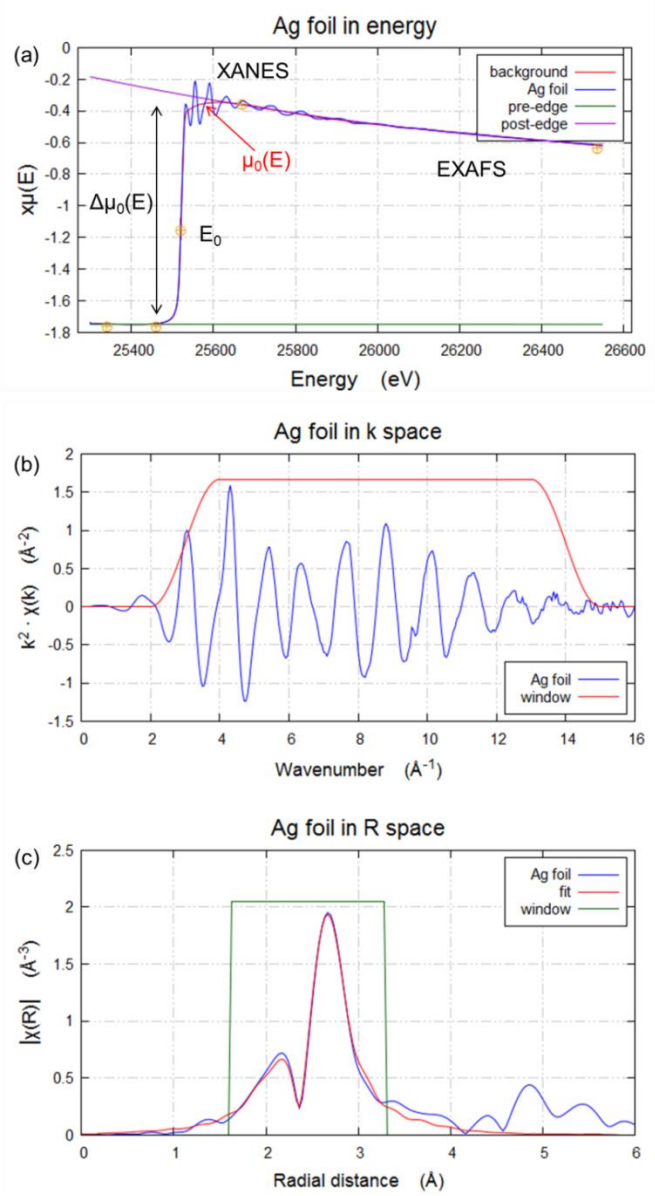

Figure 4. (a) Absorption coefficient of a Ag foil measured at the Ag K edge as a function of X-ray energy. (b) The EXAFS of the Ag foil plotted in k space. (c) The Fourier transform of the Ag foil EXAFS and fit plotted in R space.

Next, a range of the data with good quality in k space is selected to be Fourier transformed, with the result shown in Figure 4(c). The Artemis software[59] was used to fit the EXAFS data in R space. To fit the data, a theoretical EXAFS spectrum in generated using the FEFF code[60] based on a known structure, for example a FCC structure with the lattice parameter of Ag. The FEFF code is based on the EXAFS equation

$$\chi(k) = S_0^2 \sum_i N_i \frac{f_i(k)}{kR_i^2} e^{-2\sigma_i^2 k^2} e^{\frac{-2R_i}{\lambda(k)}} \sin(2kR_i + \delta_i(k)) \quad (4)$$

which can be derived from Fermi's Golden Rule and describes how the EXAFS oscillations depend on the number of neighbors of type i (N_i), the distance to those neighbors (R_i), and σ_i^2, the disorder in the neighbor distance. $f_i(k)$ is the scattering amplitude, $\delta_i(k)$ is the phase shift, $\lambda(k)$ is the inelastic mean free path (IMFP), and S_0^2 is the amplitude reduction factor, which accounts for multiple excitations at the adsorbing atom. The FEFF code will generate the scattering paths for a given structure, and those with the largest contribution to the EXAFS can be fit to the experimental data. From this analysis, N_i, R_i, and σ_i^2 can be fit. Figure 4(c) shows a single scattering Ag-Ag path fit to the experimental data of the Ag foil.

PART I. TUNING THE REACTIVITY OF PLATINUM NANOPARTICLES SUPPORTED ON ALUMINA

CHAPTER THREE: SIZE AND SHAPE EFFECTS IN THE CATALYTIC OXIDATION OF 2-BUTANOL OVER PLATINUM NANOPARTICLES

Introduction

The catalytic conversion of alcohols is a subject of broad interest because of the growing demand for environmentally cleaner industrial processes and fuels. Alcohols, or volatile organic compounds (VOCs), have been recognized as major components of air pollution.[61] The catalytic destruction of these compounds is a very promising approach because it requires operation temperatures much lower than those of thermal decomposition processes.[62-68] Moreover, industrially useful chemicals might be obtained through the partial oxidation of such alcohols.[69-73] For example, the partial oxidation of 2-butanol over metallic catalysts could provide a cleaner and more efficient route to the production of 2-butanone, or methyl ethyl ketone, an industrially useful solvent.[70]

Alcohols such as methanol, ethanol, and butanol are being considered as promising raw materials for hydrogen production via steam reforming or partial oxidation for use in fuel cells. Butanol may have certain advantages over methanol and ethanol because of its higher hydrogen content (higher energy density), lower vapor pressure, and lower risk of hazard generation during production.[74-76] Butanol is also emerging as an alternative to ethanol as a renewable biofuel for use in the transportation industry. Like ethanol, butanol can be produced through the fermentation of biomass. Isobutanol and 2-butanol are of special interest in gasoline blending because they can be used at concentrations in gasoline that are higher than those of ethanol.[74,77]

Adapted with permission from Mistry, H.; Behafarid, F.; Zhou, E.; Ono, L. K.; Zhang, L.; Roldan Cuenya, B. *ACS Catal.* **2014**, *4*, 109. Copyright 2014 American Chemical Society.

Because of the growing interest in butanol chemistry, understanding the parameters that influence catalytic performance in butanol reactions has become important for selectively designing more efficient catalysts. Following recent findings, parameters such as the nanoparticle (NP) structure (size and shape),[7,78-83] NP support,[83-87] and oxidation state of the active species[83,85,88-91] might play a role in the catalytic activity and selectivity of the supported metal NPs. Therefore, it is vital to synthesize NPs monodisperse in size, shape, and chemical composition to obtain reliable results on the respective influences of these parameters on catalytic performance.

2-Butanol oxidation over metallic catalysts is interesting both as a promising means of 2-butanone production through the partial oxidation pathway and as a model for VOC elimination through total oxidation to its combustion products. The interaction of 2-butanol with metallic surfaces has been described in several studies. Yan et al.[71] reported results of the oxidation of 2-butanol on oxygen-covered Au(111) surfaces. They found that at low oxygen coverages the oxidation was highly selective toward 2-butanone and that when the oxygen coverage was increased both partial oxidation and complete oxidation took place simultaneously.[71] Similar results were obtained by Li et al.,[92] who described the exclusive formation of 2-butanone on oxygen-covered Pd(100) surfaces. Fewer studies are, however, available on metal NPs. Hou et al.[70] investigated the oxidation of 2-butanol over 1:3 Au:Pd NPs and found 100% selectivity for 2-butanone at ~60 °C. The dehydrogenation of 2-butanol over Cu/SiO_2 xerogel catalysts was found to be structure-dependent by Lambert et al.[93] They observed almost no activity for highly dispersed catalysts with only a small particle size (~3 nm), while poorly dispersed catalysts with small and large (~15–30 nm) particles had the highest activity. For the Pt/Al_2O_3 system, the

dehydration of n-butanol was hindered by the presence of oxygen, which promoted dehydrogenation through oxidation.[94] Pure Pt or Pt-based catalysts were found to be more active than those based on Pd, Ru, Rh, Co, Au, Ag, Ir, or Ni for alcohol oxidation in the liquid and gas phases.[63,95] However, while no size dependency of the turnover frequency was detected during butanol oxidation for Pt/Al_2O_3 NP catalysts by Papaefthimiou et al.,[63] Wang et al.[95] observed the highest activities for their smallest Pt NPs (1.5–4.9 nm).

Particularly interesting is the influence of the NP shape on their reactivity.[96] For large NPs (>5 nm), this influence is mainly due to the existence of different crystalline facets associated with different NP shapes. For example, large Ag NPs (>50 nm) featuring mainly {100} facets were found to be one order of magnitude more active than truncated triangular NPs dominated by {111} facets for the oxidation of styrene.[80] However, for small NPs, the shape effect is limited not only to the specific crystallographic facets present but also to the role of highly undercoordinated atoms at corners and edges. For example, for the partial oxidation of 2-propanol to acetone, Mostafa et al.[79] found that NP shapes with a larger fraction of undercoordinated atoms at the NP surface lead to lower onset reaction temperatures, with the most active sites for that reaction being corners and edges. Narayan et al.[7] also correlated the number of corner and edge atoms on a nanocatalyst surface with increased activity. Ma et al.[97] described shape effects of Pd nanocubes for the hydrogenation of 2-methyl-3-buten-2-ol and observed that {111} facets were more active than {100} facets. Effects of shape on 2-butanol oxidation, however, have not yet been described.

In this study, we investigate the oxidation of 2-butanol over Pt NP catalysts supported on γ-Al_2O_3 prepared with narrow size distributions and well-defined geometries via inverse micelle

encapsulation. Transmission electron microscopy (TEM) and extended X-ray absorption fine structure spectroscopy (EXAFS) data were used to characterize the structure (size and shape) of these NP catalysts, and mass spectrometry was used to monitor their reactivity.

Experimental Methods

Platinum NPs with a narrow size distribution and well-defined shapes were prepared through inverse micelle encapsulation. The size and shape of the NPs were controlled by varying the metal loading (metal salt:P2VP ratio) and by using polymers with different head lengths (see Table 1). The solution was then mixed with nanocrystalline γ-Al_2O_3 powder with ~40 nm average grain size and stir-dried in air at ~60 °C. The encapsulating polymer was then removed from the γ-Al_2O_3-supported Pt NPs by annealing in O_2 at 375 °C for 24 h. A 1 wt. % Pt loading was used.

High-angle annular dark field scanning transmission electron microscopy (HAADF-STEM) images of the as-prepared samples were acquired after polymer removal by Lihua Zhang (Center for Functional Nanomaterials, BNL). The images were acquires with a JEOL2001F TEM instrument operating at 200 kV. The samples were prepared for TEM by suspending the Pt/Al_2O_3 powder in methanol, placing two drops of the solution on Cu grids with holey carbon film, and drying in air. Particle diameters were determined from the TEM images by taking the full width at half maximum of the intensity profile across each particle. The TEM images were acquired after NP reduction in H_2 at 375 °C. The maximal reaction temperature was kept below the pretreatment temperature, in this case, 300 °C, to ensure lack of NP sintering.

Table 1. Parameters used in the synthesis of size- and shape-controlled micellar Pt NPs: molecular weight of the PS-P2VP polymers, metal-salt to polymer-head ratio (loading), TEM diameters with error bars (standard deviation), the best model shape and the corresponding total number of atoms (N_t), the number of surface atoms normalized by N_t (N_s/N_t). The average number of broken bonds at the NP surface obtained from the three best shapes in agreement with the EXAFS coordination numbers and TEM diameter is also shown.

Sample	Polymer	Loading	TEM diameter (nm)	Model Shape	Best Shape N_t	Average N_s/N_t	Average Surface Broken Bonds
S1	PS(27700)-P2VP(4300)	0.1	1.0 ± 0.2		55	0.80 ± 0.05	5.3 ± 0.2
S2	PS(16000)-P2VP(3500)	0.1	1.0 ± 0.2		70	0.73 ± 0.02	5.0 ± 0.2
S3	PS(27700)-P2VP(4300)	0.2	1.0 ± 0.2		79	0.70 ± 0.05	4.5 ± 0.2

EXAFS measurements were taken at beamline X18B of the National Synchrotron Light Source at Brookhaven National Laboratory to characterize the initial NP structure. The as-prepared Pt NP/γ-Al_2O_3 samples were first pressed into pellets and then loaded into a reaction cell. The Pt-L_3 EXAFS data were acquired in H_2 (1:1 H_2:He ratio with a total flow rate of 25 mL/min) at room temperature after a 30 min *in situ* reduction in H_2 at 375 °C. Data processing was conducted using Athena and Artemis,[59] which are based on the IFEFFIT package.[98] Different scans were aligned to a Pt foil reference, and background was subtracted by fitting smooth curves to the pre- and post-edge data. To obtain first to fourth nearest neighbor (N1–N4) coordination numbers (CNs), theoretical signals were generated using the FEFF8 code[99] for a

model fcc Pt structure. This theoretical model included the most important Pt–Pt scattering paths from the absorbing atom to its nearest neighbors, including multiple-scattering paths. A description of the scattering paths used can be found in Refs. 100-102 along with details about the constraint of fitting parameters. R ranges of 1.9–6.0 Å and k ranges of approximately 2.5–17 $Å^{-1}$ were used in all fits. As described below, together with the TEM diameters, the EXAFS coordination numbers can be used to extract the shape of the NPs by comparison to model fcc Pt cluster structures.

Catalytic tests were conducted in a quartz packed-bed mass flow reactor. A K-type thermocouple positioned inside the bed at the catalyst level was used to monitor the temperature. Before the reaction was started, the catalysts were reduced using a 1:1 H_2/He mixture at 375 °C. The concentration of 2-butanol was controlled by passing He through a stainless steel bubbler. The reaction was conducted under oxygen-rich conditions (~20% O_2). All flows were controlled using MKS mass flow controllers. For each reaction, 50 mg of catalyst was used with a total flow rate of 50 mL/min. The concentration of reactants and products was monitored using a mass spectrometer (HPR 20 Hiden Inc.). The performance of each catalyst was studied at different temperatures ranging from 60 to 300 °C, and each test was repeated twice to ensure the reproducibility of the results.

Results

Figure 5a–c shows representative HAADF-STEM images of ligand-free Pt NP/γ-Al_2O_3 samples prepared via inverse micelle encapsulation acquired after NP reduction in H_2 at 375 °C. Histograms of the measured particle diameters for each sample show a narrow size distribution,

indicating that the preparation method provides a fine degree of size control (Figure 5d–f). The average TEM diameters are listed in Table 1 together with their standard deviation.

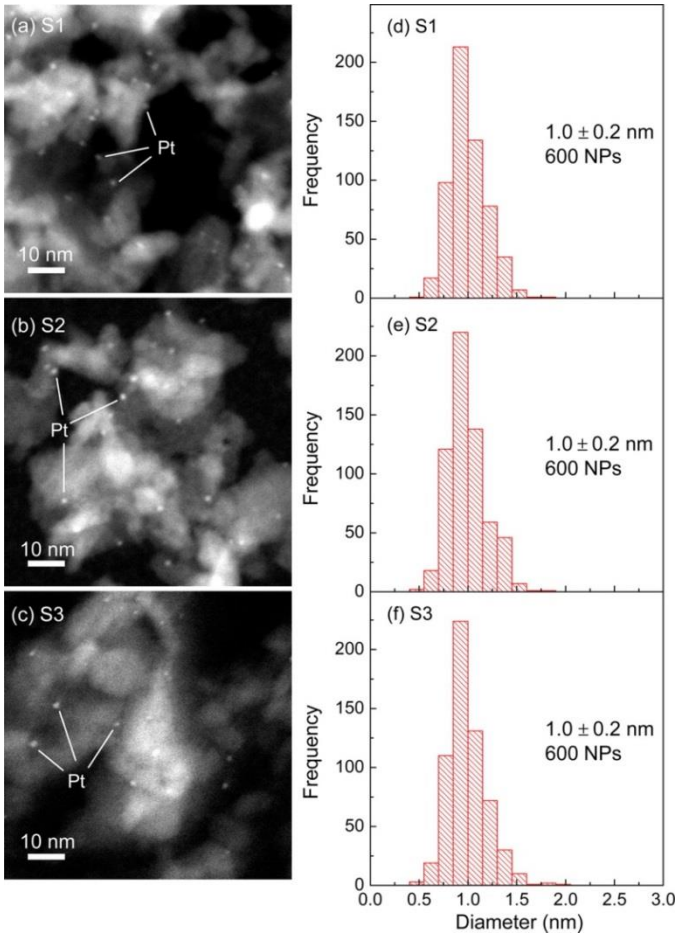

Figure 5. Representative HAADF-STEM images of Pt NPs on γ-Al_2O_3 in samples S1–S3 (a–c) acquired after removal of the encapsulating polymer and the corresponding diameter histograms (d–f).

Fourier transform EXAFS data plotted in r-space with k^2 weighting are shown in Figure 6 along with a spectrum obtained from a reference Pt foil. All measurements were taken in

hydrogen after NP reduction. In all samples studied, the NPs display a fcc structure and appear well-ordered by comparison with the bulk Pt reference (analogous features in the 4–6 Å r-space range). As described in detail in Refs. 100 and 101, to resolve the NP shape the spectra were fit using a multiple-scattering approach. Because of the high quality of the EXAFS data measured, information about the first to fourth nearest neighbor coordination numbers could be extracted from the EXAFS measurements. An example of a typical EXAFS spectrum of one of our as-prepared reduced samples (S3) together with its theoretical multiple-scattering fit is shown in the inset of Figure 6. The coordination numbers derived from this analysis for all samples are listed in Table 2. The experimentally determined coordination numbers along with the TEM diameters, taking error bars into account, were used to estimate the NP shape most prevalent in each sample by comparison with equivalent values from a database of ~4000 model fcc Pt NP shapes.[101] The three best model shapes representative of each sample were chosen by minimizing the difference between experimental and model coordination numbers and diameters, and the one providing the best agreement with the experimental parameters for each sample is included in Table 1. It should be noted that such shape determination can be reliably conducted only on narrowly distributed samples containing small NPs (<1.5 nm). For larger NPs, there would be a much larger degeneracy of shapes that would fit the same set of experimental coordination numbers for a given TEM NP diameter.

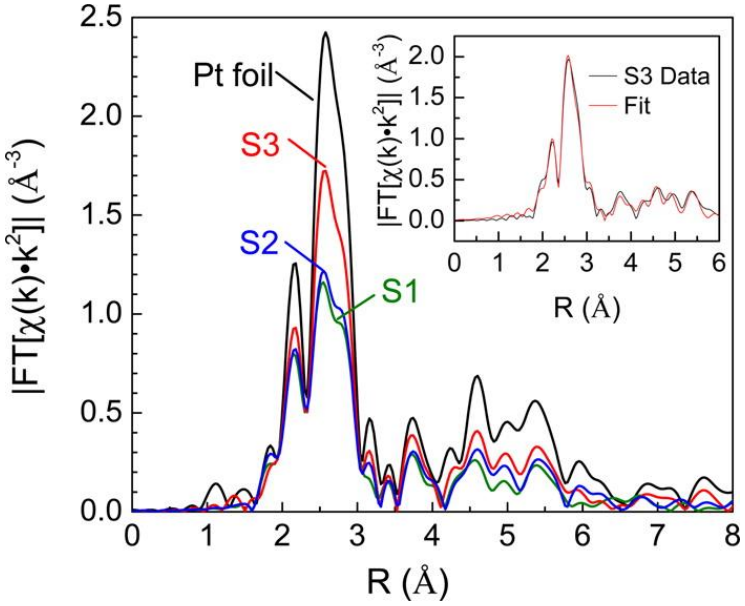

Figure 6. k^2-weighted Fourier transform EXAFS spectra of micelle-synthesized Pt NPs on γ-Al_2O_3 (samples S1–S3) and a reference Pt foil measured at room temperature in H_2 after NP reduction. The inset shows the raw data and multi-scattering fit of sample S3.

Table 2. First to fourth nearest neighbor coordination numbers (N1–N4) derived from the multiple-scattering analysis of EXAFS data acquired on as-prepared micelle-synthesized Pt NPs after reduction.

Sample	N1	N2	N3	N4
S1	8.1 ± 0.7	2.4 ± 1.5	5.7 ± 2.5	4.4 ± 1.8
S2	8.7 ± 0.6	1.7 ± 1.0	5.5 ± 2.6	3.3 ± 1.1
S3	9.4 ± 0.5	3.0 ± 1.4	8.4 ± 2.6	5.3 ± 1.6

Figure 7 shows the conversion of 2-butanol over each Pt NP/γ-Al_2O_3 sample under oxidation at different temperatures. Data at each temperature were taken under steady-state reaction conditions. In general, the oxidation of 2-butanol started at ~100 °C, and maximal

conversion was reached at ~160 °C for all the catalysts studied. The reactivity of the γ-Al_2O_3 support alone for 2-butanol oxidation was also measured at different temperatures, and a maximal conversion of 10% was found to occur below 180 °C, indicating that the γ-Al_2O_3 powder makes an insignificant contribution to the conversion measured for each sample.

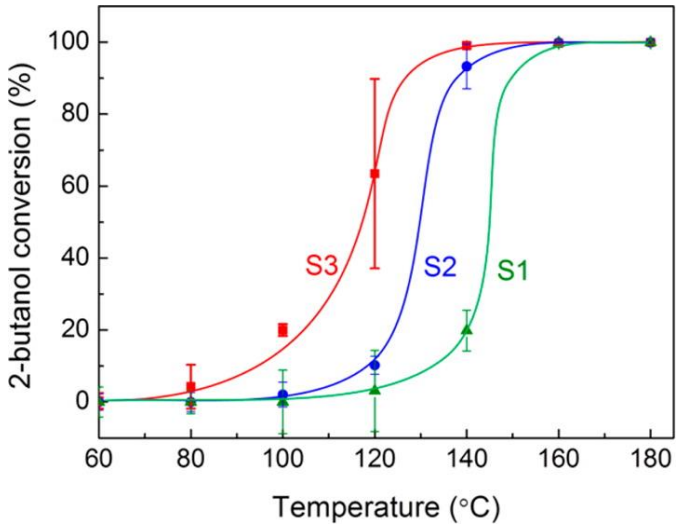

Figure 7. Catalytic performance of micelle-synthesized Pt NPs during the oxidation of 2-butanol measured at different temperatures under steady-state reaction conditions. Each experiment was repeated at least twice on fresh samples from the same catalyst batch. Error bars indicate maximal and minimal conversions measured at each temperature from two reproducibility experiments. Solid lines are guides for the eye.

The reaction products detected for the oxidation of 2-butanol were 2-butanone, carbon dioxide, and water. At low temperatures (<140–160 °C, depending on the NP shape), while the overall conversion is low, the reaction is more selective toward partial oxidation of 2-butanol, producing 2-butanone and water, as expected following equation (5):

$$C_4H_{10}O + \frac{1}{2}O_2 \rightarrow C_4H_8O + H_2O \quad (5)$$

At higher temperatures (>160–200 °C), 2-butanol undergoes complete oxidation to carbon dioxide and water, described by equation (6):

$$C_4H_{10}O + 6O_2 \rightarrow 4CO_2 + 5H_2O \quad (6)$$

The total conversion together with the selectivity toward each reaction pathway at each temperature is shown in Figure 8. From 25 to 120 °C, the total conversion is low; however, the conversion toward the formation of 2-butanone is favored over the production of CO_2 in all samples. At 120 °C, the selectivity for 2-butanone begins to decrease, while the selectivity toward CO_2 increases. Complete oxidation of 2-butanol to CO_2 is achieved with 100% selectivity at approximately 160 °C for S1, 140 °C for S2, and 200 °C for S3.

Discussion

The NP samples in this study were prepared using colloidal chemistry by loading inverse micelles formed from PS-2VP diblock copolymers with different molecular weights and distinct metal:P2VP ratios with a Pt salt (see Table 1). Because of the very small size of the NPs (~1 nm) and the high absorption of the thicker nanocrystalline Al_2O_3 support, HAADF-STEM measurements were used to obtain adequate contrast between the NPs and the support. Under these conditions, only the diameter of the NPs could be resolved, not their shape. Although TEM measurements provide similar average NP diameters with narrow size distributions for all samples, distinct catalytic behavior is observed (Figure 7), in particular, a different onset reaction temperature (Figures 7 and 9), distinct selectivity at a given temperature (S1 and S2 compared to S3), and a different transition temperature from the partial (2-butanone as the main product) to the total oxidation of 2-butanol (CO_2 as the product) (S1 and S2 compared to S3) (Figure 8).

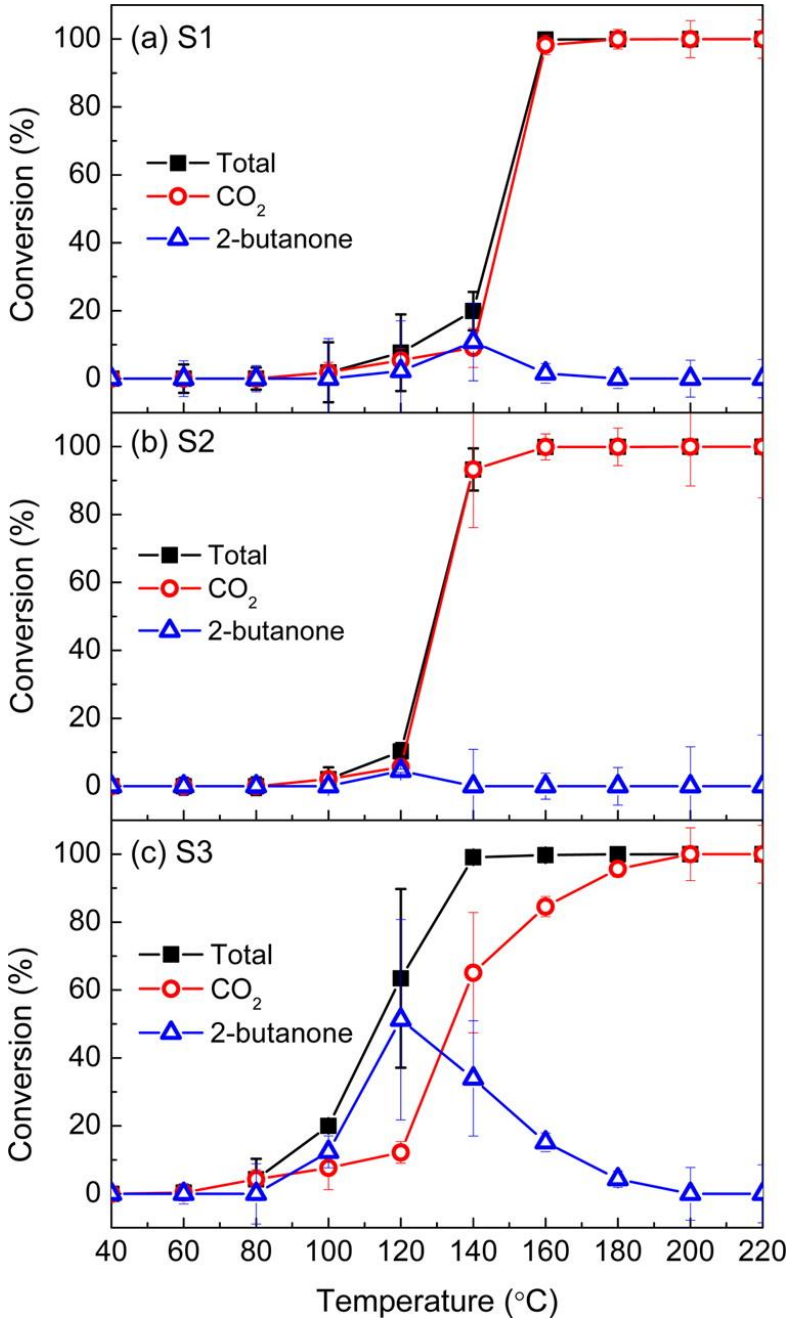

Figure 8. Total 2-butanol conversion (■), conversion of 2-butanol to 2-butanone (△), and conversion of 2-butanol to carbon dioxide (○) during the oxidation of 2-butanol over micelle-synthesized Pt NPs/γ-Al_2O_3 for samples S1–S3 (a–c, respectively). Error bars indicate maximal and minimal conversions measured at each temperature in reproducibility experiments under identical reaction conditions.

It should be noted that the morphological characterization of our NPs, revealing small size-selected NPs, was performed after pretreatment in H_2 at 375 °C, but before exposure to the reactant. Nevertheless, because the reaction temperature never exceeded 300 °C, NP stability against sintering is expected. In fact, previous work by our group on micellar Pt/Al_2O_3 NPs showed that the EXAFS spectra and TEM images of the as-prepared H_2-pretreated NPs were analogous to those measured after the 2-propanol oxidation reaction at similar temperatures after subsequent reduction in hydrogen, corroborating the absence of coarsening.[103] The NPs used in this study were exposed to comparable oxygen-rich conditions and had reached 100% conversion of 2-butanol at 240 °C, so it is unlikely that NP sintering occurred. In addition, the thermal stability of identical micellar Pt/Al_2O_3 NPs up to 450 °C in O_2 was previously demonstrated.[34]

To understand the structure–reactivity trends observed for nearly identically sized NPs, the TEM diameters and EXAFS coordination numbers were used to obtain a model for the dominant NP shape in each sample. As shown in Table 2, the EXAFS coordination numbers of samples S1–S3 are different, indicating the presence of NPs with distinct shapes. For example, for a given TEM NP diameter, flatter NPs are characterized by lower average coordination numbers. According to the first NN CNs listed in Table 2, sample S1 has the lowest value of N1 and S3 the highest. Therefore, S1 should have the smallest and/or the flattest NPs and S3 the largest and/or the most three-dimensional NPs. Via determination of the shape of the NPs, other useful parameters such as the total number of atoms (N_t), the ratio of the atoms at the NP surface normalized by the total number of atoms (N_s/N_t), and the average number of broken bonds at the NP surface can be obtained. A Pt atom in a bulk fcc structure has a first NN CN of 12, but surface atoms on NPs have lower CNs depending on their specific location. The number of

broken bonds for each surface atom is defined as 12 – N1 of that atom. While N_s/N_t represents the surface:bulk ratio, which is expected to be larger for smaller NPs, the average number of missing bonds depends mainly on the distinct NP facets and also the number of atoms at corner and edge sites. For instance, Pt(111) and Pt(100) facets have average numbers of missing bonds of three and four, respectively, while this value could be higher (up to eight) for atoms at NP corners and edges.

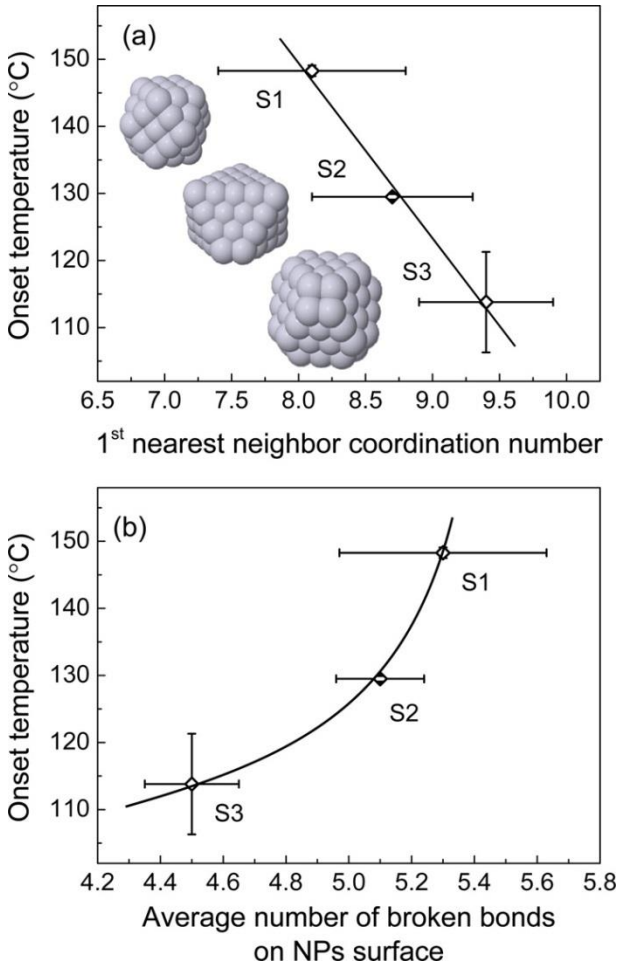

Figure 9. Onset reaction temperature (temperature of 50% conversion) as a function of (a) first nearest neighbor coordination number (EXAFS) and (b) the average number of missing bonds on the NP surface.

Figure 9a shows a clear correlation between the onset reaction temperature (T of 50% conversion) and the first NN CN (N1) obtained from the EXAFS analysis of Figure 7. Interestingly, samples with lower coordination numbers (smaller and/or flatter) have higher onset reaction temperatures and lower activities for 2-butanol oxidation. A similar trend is observed in Figure 9b, where the onset reaction temperature is higher for the samples with the largest number of atoms at corner and edge sites, namely, those with the largest number of broken bonds at the NP surface. This is contrary to our previous findings for 2-propanol partial oxidation, where it was shown that the NPs with the largest number of broken bonds were the most active[79]. To understand the difference between these two studies, we should take into account the selectivity of our catalysts in the 2-propanol and 2-butanol oxidation reactions. In the case of 2-propanol, the onset temperature for its partial oxidation to acetone ranges from 45 to 85 °C, depending on the specific NP shape, with more than 90% selectivity toward partial oxidation for all samples investigated below 100 °C. In a follow-up study, *operando* EXAFS and X-ray absorption near edge spectroscopy (XANES) data revealed a correlation between the chemical state of ∼0.7 nm Pt NPs and the switch in the selectivity observed from the partial (acetone) to total oxidation (CO_2) of 2-propanol above ∼140 °C.[103] Specifically, it was demonstrated that the partial oxidation of 2-propanol occurs when the NPs are oxidized (<140 °C), while the total oxidation pathway becomes dominant over metallic Pt NPs with a surface covered by chemisorbed oxygen (>140 °C).[103] In contrast, in the case of 2-butanol, conversion toward the partial oxidation product 2-butanone is low at all temperatures (nearly negligible for S1 and S2 and only clearly detectable for S3 below 160 °C), and the temperature required to achieve 100% total conversion is higher (140–160 °C), but also dependent on the specific NP geometric structure. In addition, in

this case, 100% conversion of 2-butanol is never achieved during its partial oxidation temperature regime, only at high temperature during its total oxidation to CO_2.

The trend previously observed for 2-propanol partial oxidation[79] (undercoordinated Pt atoms more active) is the opposite of the trend obtained here for 2-butanol total oxidation. A possible explanation for the shape dependency observed here could be the size-dependent stability of Pt oxide species. Binding of oxygen to Pt is stronger for smaller NPs;[104-106] therefore, Pt oxide decomposition is expected to require a higher temperature on smaller NPs. Assuming that metallic Pt is the active species for the total oxidation of butanol to CO_2 (similar to 2-propanol),[103] the higher onset temperature for 2-butanol oxidation over smaller NPs could be due to the higher temperature needed for Pt oxide decomposition. Similar structure-dependent reactivity trends have been shown in the literature for complete oxidation of various hydrocarbons over Pt/Al_2O_3 catalysts, with larger NPs showing higher activity because of their lower susceptibility to oxide formation.[107-110] Carlsson et al.[109] prepared Pt/Al_2O_3 monolith catalysts with particle sizes ranging from 10 to 48 nm for the total oxidation of propane at varying oxygen concentrations, and their experiments showed a decrease in activity after exposure to oxygen-rich conditions, most likely because of oxide formation. Furthermore, catalysts with large Pt NPs showed higher activity and could withstand higher oxygen concentrations before experiencing a decrease in activity as compared to smaller Pt NPs, indicating that the larger NPs are more difficult to oxidize than the smaller NPs. Also, for the oxidation of propane, Yazawa et al.[110] found higher turnover frequencies (TOFs) for Pt/Al_2O_3 catalysts with lower dispersion, resulting from the lower degree of oxidation of larger Pt NPs as revealed by XANES.

In addition to the PtO_x decomposition effect, the binding energy of chemisorbed oxygen species that might be present under reaction conditions at higher temperatures could also play a role in the shape-dependent reactivity obtained. Papaefthimiou et al.[63] studied the oxidation of benzene, butanol, and ethyl acetate over Pt/Al_2O_3 catalysts and fit their reaction data using a simple power law rate equation. Remarkably, the highest reaction order with respect to VOC concentration was found for the butanol oxidation reaction, where the most negative reaction order for oxygen was obtained. Such a negative reaction order was interpreted as the inhibition effect of oxygen, suggesting a Langmuir–Hinshelwood type of reaction mechanism. Along this line, the expected higher binding energy of chemisorbed oxygen on smaller NPs[104,106] or NP shapes with a larger fraction of strong binding sites (corners and edges) would lower the reaction rate and increase the onset temperature, which was observed in our study. Similar results showing higher activity for larger NP sizes have been obtained for the complete oxidation of other VOCs over the Pt/Al_2O_3 system.[111-118] For example, Radic et al.[111] compared 1.0 and 15.5 nm Pt/Al_2O_3 NPs in the complete oxidation of n-hexane and toluene, finding TOFs 10 times higher for the larger particles than the smaller for both alcohols because of the decreased Pt–O bond strength in the larger particles.

In summary, a shape-dependent trend was observed for the onset reaction temperature during the oxidation of 2-butanol, where NPs with the smallest number of weakly coordinated atoms (smallest number of broken bonds) at the NP surface displayed the best catalytic performance at low temperatures. The total oxidation of 2-butanol to CO_2 was the dominant reaction pathway, and metallic Pt surfaces decorated by chemisorbed oxygen were found to be the active species during this reaction. Therefore, the shape-dependent reactivity can be

explained by a lower PtO_x decomposition temperature and weaker binding of chemisorbed oxygen on NPs with less broken bonds at the surface, which favors the total oxidation pathway.

Our study illustrates the critical role played by the NP structure, specifically its size and shape, in its catalytic performance, in particular, the onset reaction temperature, preferred reaction pathway, and selectivity.

Conclusion

Small (~1 nm) size- and shape-controlled Pt NPs supported on γ-Al_2O_3 were used as a model system to investigate structure–reactivity relationships during the oxidation of 2-butanol. A shape dependency of the onset reaction temperature was observed, with decreasing activity detected for NPs with the largest number of undercoordinated surface atoms. In addition, very low activity for the partial oxidation of 2-butanol was obtained, with only a low conversion to 2-butanone observed for S3 below 160 °C. The dominant reaction pathway toward CO_2 formation was favored by the presence of Pt NPs with a small number of edge and corner sites. This result is explained considering the negative effect that the strong binding of oxygen to such sites (through the stabilization of chemisorbed oxygen or that of PtOx species) might have on the total oxidation pathway.

This study emphasizes the importance of tailoring the structure of catalysts at the atomic level to gain control of not only their catalytic activity but also their selectivity and optimal operation temperature.

CHAPTER FOUR: ADSORBATE-INDUCED SHAPE TRANSFORMATION IN PLATINUM/γ-Al_2O_3 NANOPARTICLES

Introduction

The interaction of hydrogen with supported noble-metal NPs is of great interest in heterogeneous catalysis, especially for applications such as hydrogenation reactions,[119,120] electrocatalysis,[121,122] and hydrogen storage.[123,124] Recent research has shown many of these catalytic processes to be dependent on catalyst particle size and shape.[83,125-127] Smaller, subnanometer-sized particles are often more active because of the increased number of edge and corner sites. For some chemical processes, these properties might correspond to the increased ability of such small NPs to adsorb hydrogen,[128] which has received much attention in recent literature, particularly for the Pt/Al_2O_3 system.[14,129,130] On Pt(1 1 1) single crystals, hydrogen coverage has been measured to saturate at a 1:1 ratio of H/Pt, a fact commonly used to calibrate metallic surface area measurements.[131] However, H_2 chemisorption isotherm measurements have indicated that nanometer-sized particles can adsorb between 1.1 to 1.5 H atoms per Pt.[132-134] Theoretical work has predicted even higher hydrogen coverages for subnanometer Pt particles,[135,136] such as Pt_{13} NPs which can stabilize 3.3 H/Pt as a result of particle shape reconstruction.[14] Using size- and shape-selected Pt/γ-Al_2O_3 NPs, Behafarid et al.[129] observed experimentally that small NPs with a large number of low-coordinated surface atoms (corner and edge sites) can adsorb significantly more H/Pt at atmospheric pressure than larger, more bulk-like NPs.

Adapted with permission from Mistry, H.; Behafarid, F.; Bare, S. R.; Roldan Cuenya, B. *ChemCatChem* **2014**, *6*, 348.

Understanding the adsorption of hydrogen on NP surfaces has been challenging because of the complex interplay between particle structure and electronic properties, adsorbate interactions, and support effects.[129,137-139] Furthermore, under realistic reaction pressures and temperatures, NPs can have a dynamic structure which allows them to transition between several stable structural isomers,[14,140,141] which further complicates their characterization. Several recent studies have measured morphological changes in Pt NPs under hydrogen environments.[133,142,143] Particularly interesting are recent theoretical investigations by Mager-Maury et al.,[14] who calculated structural changes in subnanometer Pt/γ-Al_2O_3 NPs as a function of temperature and pressure. Their theoretical work predicts that an increase in the H coverage should result in Pt_{13} NPs evolving from a biplanar to a cuboctahedral morphology as a result of weakened metal–support interactions and surface Pt hydride formation.[14]

In situ XANES spectroscopy at the Pt L_3-edge has proved to be an excellent tool for the study of hydrogen adsorption on Pt NPs through observing changes in the d electron density of states of the particles under different adsorbate environments.[129,134,138,139,142,144-151] In this experimental work we investigate the pressure-dependent changes in hydrogen coverage on size- and shape-selected Pt/γ-Al_2O_3 NPs as well as on their structure by using *in situ* XANES and EXAFS spectroscopy measurements. Difference XANES (ΔXANES) plots were used to quantify the H/Pt ratio as a function of H_2 pressure. In addition, EXAFS measurements showed changes in Pt–Pt bond length and coordination number, revealing morphology changes in the Pt NPs at room temperature under increasing H_2 pressure.

Experimental Methods

Pt/γ-Al_2O_3 NPs were prepared in solution through inverse micelle encapsulation. The molar ratio of Pt to polymer P2VP was 0.05. The solution was then filtered, nanocrystalline γ-Al_2O_3 powder (average grain size 40 nm) was added, and then the solution was stir-dried in air at 60 °C. The Pt/γ-Al_2O_3 NPs were then calcined at 375 °C in O_2 for 24 h to remove the polymer, and X-ray photoelectron spectroscopy was used to demonstrate that the encapsulating polymers were completely removed, as indicated by the absence of a C 1 s signal. The size and shape of the prepared NPs was determined using a combination of low-temperature EXAFS multiple scattering analysis and TEM diameter measurements. The above synthesis resulted in size-selected Pt NPs (0.8±0.2 nm), with approximately 22 atoms (Pt_{22}) in a flat (2 D) bilayer shape.[101,152]

XAFS measurements were performed at Beamline 10-ID-B of the Advanced Photon Source at Argonne National Laboratory. The Pt/γ-Al_2O_3 sample (60 mg) was loaded into an *in situ* beryllium high-pressure reaction cell allowing pressurization above 20 bar.[153] The reaction cell was housed within a furnace allowing for sample heating by means of an external PID temperature controller. The Pt L_3-edge was measured in transmission mode, and at least three spectra were acquired at each pressure condition for signal averaging. The gas flows were controlled using Brooks mass flow controllers. The sample was first reduced in 50 % H_2 balanced by He at a flow of 50 mL min^{-1} at 375 °C. Next, the sample was cooled to 25 °C and measured at atmospheric pressure in H_2, then measurements were taken after the cell was pressurized to 6, 11, 16, and 21 bar of H_2. The reactor was then depressurized to 4 bar, flushed with He, and heated to 375 °C to remove all H_2 from the sample, and a measurement of the

adsorbate-free NPs was taken at 25 °C in 4 bar He. A final set of measurements was taken at 375 °C in H_2 pressures of 0.15, 0.5, and 3 bar.

Data processing was conducted using the IFEFFIT package.[98] By using the Athena software,[59] reference spectra from each measurement were aligned to a Pt reference foil, and then data were merged and normalized by fitting smooth curves to the pre-edge and post-edge. ΔXANES plots were constructed by subtracting the spectra measured in He at 25 °C from spectra measured at various pressures of H_2. Owing to the presence of isosbestic points in XANES data at different hydrogen coverages, the ΔXANES data crosses the zero value at the same energies for all different H coverages. The area of the second ΔXANES peak indicated in Figure 11(a) as "peak B"[129] was integrated by using OriginLab software over the energy range in which peak B was positive. EXAFS spectra were fit in R-space in the Artemis software[59] with FEFF 8 calculations of face-centered cubic Pt to simulate Pt–Pt scattering paths and the Pt–O scattering path from $Na_2Pt(OH)_6$ to simulate Pt–O scattering paths. Data sets measured under different pressures were fit simultaneously with the energy shift ΔE_0 constrained, and owing to the strong correlation between Pt–Pt coordination number and bond length disorder (σ^2), σ^2 was fit as a shared parameter.

Results and Discussion

The Pt L_3-edge XANES analysis of size-selected 0.8±0.2 nm Pt NPs with 2 D shape[101,152] were measured as a function of H_2 pressure. In Figure 10 the normalized absorption coefficient of Pt NPs acquired in H_2 pressures of 1–21 bar and in 1 bar He, respectively, at 25 °C is shown (1 bar=100 kPa). A positive shift (+0.6 eV) in the absorption edge energy was observed upon hydrogen chemisorption as compared to the foil. Additionally, the intensity of the absorption

peak ("white line") was found to increase with increasing H_2 pressure, with adsorbate-free NPs measured in He showing a significantly lower intensity. The white-line intensity corresponds to the unoccupied 5 d electron density of states, and its increase upon hydrogen adsorption reflects the transfer of charge from Pt to H. Furthermore, a broadening of the "white line" is observed upon hydrogen chemisorption.

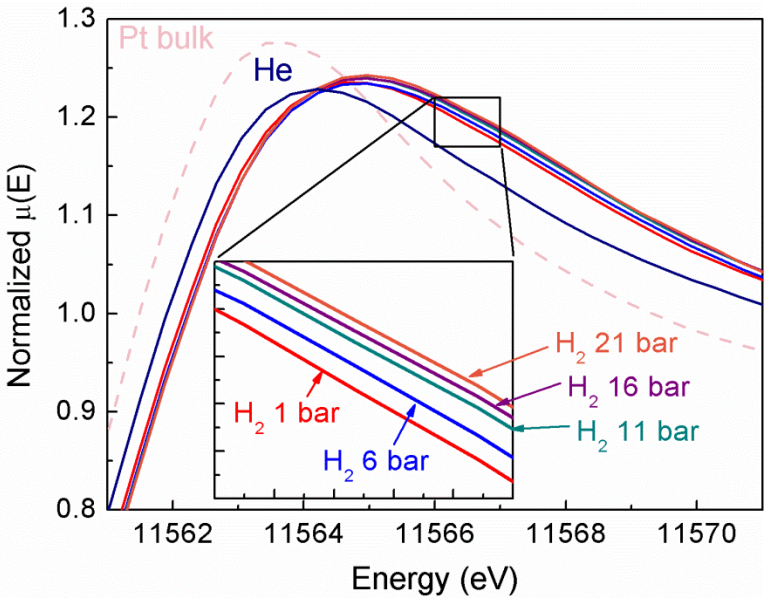

Figure 10. Pressure-dependent normalized absorption coefficient, μ(E), versus energy (XANES region) for the Pt L_3-edge of Pt NPs on γ-Al_2O_3. Data were acquired at pressures from 1 to 21 bar at 25 °C. Data acquired in He at 25 °C and Pt foil data are also plotted for reference.

As shown in Refs. 129,145,147,154, the integrated area of the absorption peak can be used to extract quantitative information on the hydrogen coverage on the NPs. However, to conduct such analysis, a reference of the hydrogen-free state of the NPs is required. For this purpose, XANES data obtained in helium were used as a reference. To ensure that the Pt NPs were hydrogen-free during the measurements in helium after the NP reduction pretreatment in

hydrogen, the reaction cell was pressurized to 4 bar He and heated to 375 °C for 30 min, then cooled to 25 °C in He before the measurements. An alternative approach (not used herein) to define the adsorbate-free state of the NPs involves the use of reference XANES data acquired under hydrogen at a high enough temperature at which negligible amounts of hydrogen would be adsorbed on the NP surface (375 °C for our Pt_{22} NPs, but this approach may have added complexity due to the embedded effect of temperature.

To quantify the change in the hydrogen coverage on the NP surface under elevated H_2 pressure at 25 °C, ΔXANES plots were calculated. In Figure 11a the ΔXANES spectra for Pt NPs are shown, measured in 1–21 bar H_2 at 25 °C. An increase in the area of peak B is seen with an increase in H_2 pressure, corresponding to an increase in H coverage on the NP surface. To estimate H/Pt ratios, the area of the ΔXANES peak B was normalized by the peak B area of large 1 nm diameter particles (Pt_{140}) with well-defined shape previously measured[129] in 1 bar H_2 at 183 K. Under these conditions, the larger NPs (Pt_{140}) are postulated to be saturated with one hydrogen atom per surface platinum atom. The number of hydrogen atoms per total number of Pt atoms in the Pt_{22} NP is shown in Figure 11b. To best compare our H/Pt ratios with those found in the literature, we normalized the hydrogen coverage by the total number of atoms in the NP, and not the number of Pt atoms at the surface, as was given in our previous work.[129] The hydrogen coverage on the NPs at 25 °C was found to increase from 1.9 to 2.5 H/Pt with an increase of pressure from 1 to 21 bar. Theoretical DFT H/Pt ratios for Pt_{13} NPs calculated by Mager-Maury et al.[14] are also plotted in Figure 11b. For these smaller NPs, a higher H/Pt ratio of approximately 2.6 is seen at atmospheric pressure of H_2, which increases only slightly with increasing H_2 pressure. This indicates that the smaller theoretical Pt_{13} NPs are able to adsorb more hydrogen

than our experimental Pt_{22} NPs under equivalent conditions. This trend is in agreement with our previous work on Pt/γ-Al_2O_3 NPs showing that hydrogen adsorption capacity increases with decreasing particle size.[129] Similarly, Jensen et al.[143] obtained a saturation coverage of 2.9 H/Pt at 25 °C for their smaller Pt_{13} NPs supported on a zeolite using H adsorption isotherms.

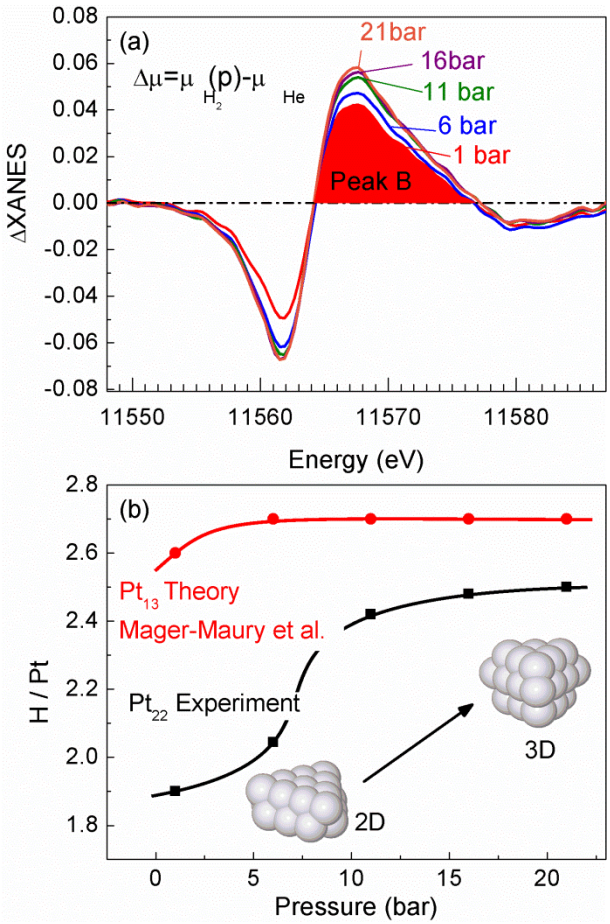

Figure 11. (a) ΔXANES spectra from the Pt L_3-absorption edge of Pt NPs on γ-Al_2O_3 displayed as a function of the H_2 pressure during measurement. In all plots, the RT He data are subtracted from those acquired at varying pressures in H_2. b) H/Pt ratio calculated from the area of the ΔXANES peak B normalized by the area of bulk-like NPs measured at 183 K (■). Model shapes for low and high coverage are shown as well as theoretical H/Pt ratios from Ref. [14] for Pt_{13} NPs (●).

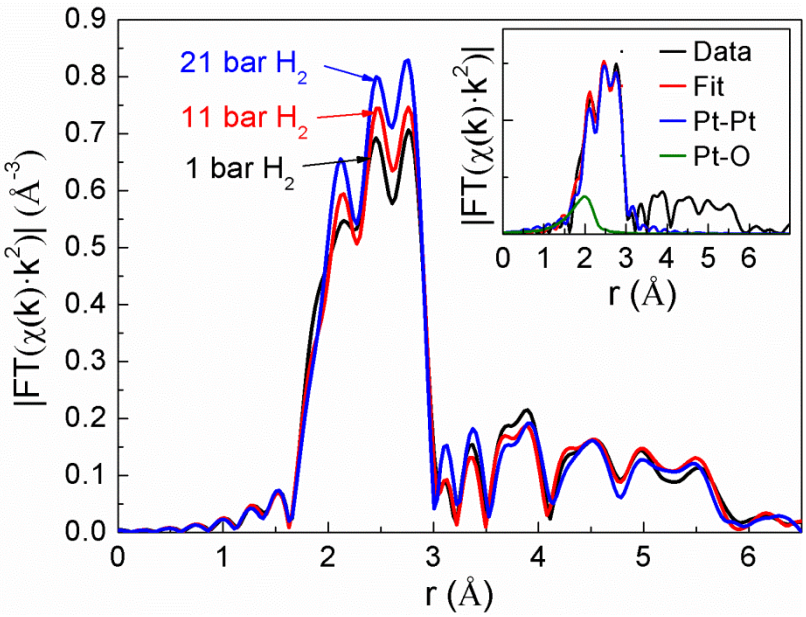

Figure 12. Fourier transform magnitudes of k^2-weighted EXAFS data for Pt/γ-Al_2O_3 NPs measured at 25 °C under 1–21 bar H_2 pressure. A first shell fit of the experimental data measured under 11 bar H_2 is included as an inset.

To investigate any morphological changes in the Pt NPs with increasing hydrogen coverage, EXAFS analysis was performed to extract 1st nearest-neighbor (NN) coordination number (CN) and bond length (*r*) information as a function of the hydrogen pressure. All EXAFS data from the reduced Pt NPs were fitted with two components corresponding to Pt–Pt (2.76 Å) and a long Pt–O (≈2.5 Å) bond.[127,154] The Pt–O component exhibits a longer bond length than that of the Pt oxide species or chemisorbed oxygen on Pt (≈2.0 Å), and is assigned to the NP/support interface.[127,154] The magnitude of the Fourier transform EXAFS data acquired in hydrogen at 25 °C from 1 bar to 21 bar is shown in Figures 12 together with an example fit as inset. In Table 3, EXAFS results are given for the Pt–Pt and Pt–O first-shell fits. In Figure 13,

the Pt–Pt 1st NN coordination numbers and Pt–Pt bond lengths are displayed for our Pt NPs under increasing H_2 pressure extracted from the analysis of EXAFS data, including NN data for Pt_{13} clusters from Mager-Maury et al.[14] as a function of the H/Pt ratio.

Table 3. 1st NN CNs and Pt–Pt and Pt–O bond lengths (*r*) extracted from single scattering analysis of EXAFS data acquired on Pt NPs at 25 °C in different pressures of H_2.[a] Fit uncertainties are given in parentheses for the last significant figure.

H_2 pressure (bar)	CN (Pt–Pt)	*r* [Å] (Pt–Pt)	CN (Pt–O)	*r* [Å] (Pt–O)
0 (He)	6.0 (7)	2.733 (5)	2 (1)	2.52 (3)
1	7.5 (7)	2.755 (4)	1.6 (8)	2.50 (4)
6	7.6 (7)	2.755 (4)	1.7 (9)	2.55 (4)
11	8.0 (7)	2.761 (4)	1.5 (8)	2.49 (5)
16	8.0 (7)	2.761 (3)	1.5 (8)	2.49 (4)
21	8.8 (8)	2.752 (3)	0.8 (7)	2.53 (8)

[a] The EXAFS fitting was performed with S_0^2 fixed at 0.85. The shared fit parameters ΔE_0 and σ^2 were ΔE_0=2.6 (5) eV and σ^2=0.0072 (4) Å^2.

Our results reveal that an increase in H_2 pressure correlates to an increase in Pt–Pt CN from 7.5 to 8.8, which indicates a structural change in the NPs as the coverage of H increases. A significant change in Pt–Pt CN occurs between 16 and 21 bar, indicating a possible abrupt structural change at this pressure. The Pt–Pt 1st NN distance exhibits a slight increase with H_2 pressure up to 21 bar, at which point it drops. The Pt–O CN decreases with increasing hydrogen pressure, indicating that Pt–O bonds between the metal and the hydroxylated Al_2O_3 support are broken. The increase in Pt–Pt coordination number and bond length, together with a concomitant decrease in the Pt–O coordination number, suggest that the NPs are restructured from their

original 2D bilayer shape, modeled by our shape analysis,[101,129,152] to a more 3D-like structure upon hydrogen adsorption.

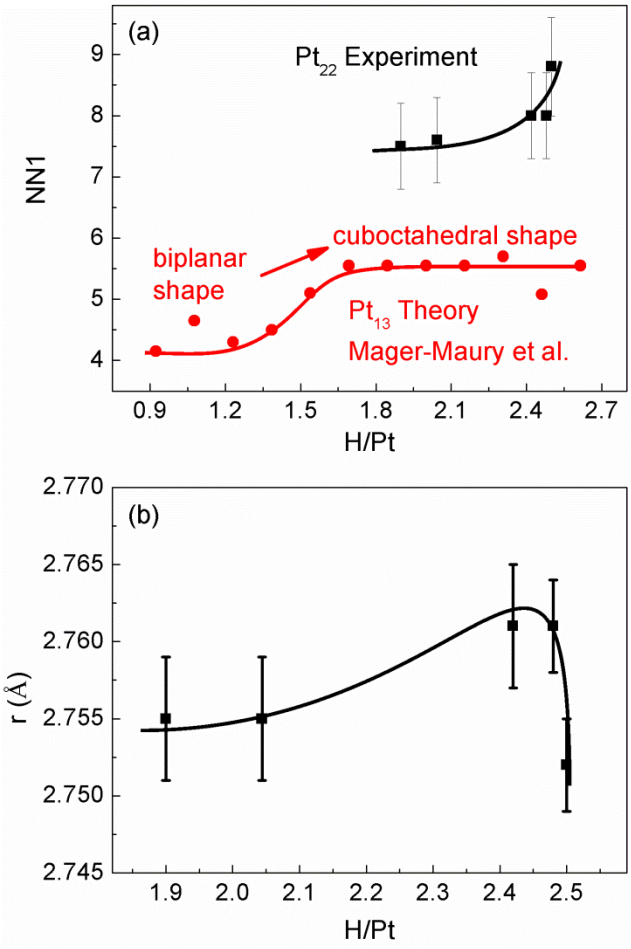

Figure 13. (a) Pt–Pt 1st NN coordination number from EXAFS single-scattering analysis as a function of H coverage (■), and theoretical 1st NN coordination numbers for Pt_{13} from Ref. [14] (●). (b) Pt–Pt bond length (*r*) as a function of H coverage.

Previous theoretical studies have predicted hydrogen-induced morphological changes in subnanometer Pt NPs. For example, calculations by Mager-Maury et al.[14] on Pt_{13} clusters

supported on γ-Al_2O_3 revealed that they are stabilized in a 2D biplanar configuration at low hydrogen coverage caused by strong metal–support interactions. However, at coverages above approximately 1.5 H/Pt, these NPs are transformed to a 3D cuboctahedral shape as a result of a weakening of the metal–support interaction by the adsorbed H, which is believed to accumulate at the NP/support interface and to contribute to NP/support bond breaking. A transformation from 2D to 3D shape would explain the increasing Pt–Pt CN with increasing H_2 pressure seen in this study, and also the drop in Pt–O coordination number as bonds between metal and support are broken. It should be, however, noted in Figure 13(a) that the calculations in Ref. [14] revealed an approximately constant cuboctahedral shape for the high H/Pt coverages used in our study, because their Pt_{13} NPs have already undergone a shape transformation from biplanar to cuboctahedral shape. It is plausible that their smaller Pt_{13} NPs are more susceptible to shape transformation at lower H coverages because of their smaller size. Sintering could be another possible explanation for the increase in the Pt–Pt coordination number. Room-temperature Ostwald ripening has been reported for Pd nanoclusters upon exposure to hydrogen, which was explained by the formation of Pd hydride.[155] Subsurface absorption of hydrogen would result in a decrease in Pt–Pt coordination numbers, which was not observed in this study. Therefore, room-temperature NP growth is not likely to occur in our samples, because they were also already preannealed in H_2 at much higher temperature (375 °C) without any evidence of sintering.[101] Although our results show no evidence for subsurface hydrogen, surface hydride species may still form on our NPs. Pt NPs are not known to form hydrides, but Hakamada et al.[156] reported that nanoporous Pt could form hydride species under lattice strain. In addition, theoretical studies predict the formation of Pt hydrides on nanoparticles at high H coverage.[14,141]

Recent work by Jensen et al.[143] has provided experimental evidence for Pt NPs restructuring under hydrogen pressure. Their Pt_{13}/KL zeolite NPs were measured by EXAFS after reduction in H_2 and after H desorption by heating at 573 K. Upon desorbing H, the Pt–Pt CN decreases, Pt–O CN increases, and the Pt–Pt bond length decreases, which the authors attribute to a restructuring of the NP to a flatter shape with more support interaction. DFT calculations by Chen et al.[141] also predicted restructuring for unsupported Pt_{13} NPs, which undergo a phase transformation from icosahedral to face-centered cubic structure at approximately 0.8 H/Pt, and above 2.8 H/Pt, H atoms can penetrate into the structure.

In our study, the Pt–Pt bond length shown in Figure 13b increases with increasing hydrogen pressure until a coverage of 2.5 H/Pt is reached, at which point the bond length drops. For nanometer-sized Pt NPs, the Pt–Pt bond length has been shown to increase with increasing hydrogen coverage caused by a lifting of the bond-length contraction by the adsorbed hydrogen.[134,139,142,157] A structural change in the NPs to a more 3D shape with a lower fraction of atoms at the surface would also relieve surface strain responsible for bond contraction. The anomalous drop in bond length measured at the highest pressure does not fit the previously described trends, but might be plausible if the strain induced by the NP support is initially expansive, in which case the NP break off from the support would result in Pt–Pt bond length contraction. Indeed, DFT calculations by Hu et al.[137] predict that for the majority of stable Pt_{13} cluster shapes, the γ-Al_2O_3 support induces an expansion in the Pt–Pt distance compared to that of unsupported NPs. Alternatively, this drop could be related to decomposition of surface hydride species at high hydrogen pressures, which was seen on nanoporous Pt above 13 bar H_2

pressure.[156] Nevertheless, it should be noted that as no loss of hydrogen was observed at this pressure through XANES analysis, the latter possibility is unlikely.

The present work illustrates the intricate correlation between the NP environment (surrounding adsorbates and support) and the electronic and structural characteristics of small NPs. To gain further insight into these effects, additional studies are planned with Pt NPs of different size and shape, and to extend the H_2 pressure regime to higher values.

Conclusion

An *in situ* investigation of the role of chemisorbed hydrogen on the electronic and structural properties of size-controlled Pt NPs supported on γ-Al_2O_3 was performed by means of XANES and EXAFS measurements. *In situ* XANES measurements on approximately 0.8 nm Pt NPs (Pt_{22}) revealed an increase in the hydrogen coverage on the surface of the NPs (H/Pt ratio) with increasing hydrogen pressure from 1 to 21 bar at 25 °C. Furthermore, EXAFS measurements revealed a change in the structure of the NPs from 2D to 3D, evidenced by increasing Pt–Pt coordination numbers and decreasing Pt–O (NP/support interface) coordination numbers. This study highlights the dynamic nature of NP catalysts under industrially relevant conditions and the superior adsorption capacity of subnanometer particles, properties that have high importance to catalyst design.

PART II. CASE STUDY: TUNING ACTIVITY AND SELECTIVITY IN MODEL CATALYSTS FOR CO_2 ELECTROREDUCTION

CHAPTER FIVE: PARTICLE SIZE EFFECTS IN THE CATALYTIC ELECTROREDUCTION OF CO_2

Size Dependent Reactivity of Au Nanoparticles for CO_2 electroreduction

Introduction

Because of the growing global demand for energy, rising CO_2 emissions from the burning of fossil fuels are an increasing environmental threat that, if unmitigated, could have disastrous environmental consequences. An ideal solution would be not only to curb CO_2 emissions by switching to sustainable energy sources but also to capture and reutilize waste CO_2 though its conversion into fuels and valuable chemicals[158]. A promising method of CO_2 utilization is its direct electrocatalytic reduction into useful hydrocarbons, such as methane and ethylene, or H_2 and CO for Fischer–Tropsch processes[43,159]. Several electrochemical[43,160-163] and computational[162-166] studies have investigated different metal electrodes for this reaction. However, low energy efficiency due to the need for high overpotentials to activate this reaction and low selectivity for desirable hydrocarbons compared with the formation of H_2 mean that this process is not yet industrially viable[167]. Pioneering work by Hori and others demonstrated that gold is one of the few metals that can produce CO from the reduction of CO_2[160,168,169]. Several recent studies indicate that gold electrodes with modified surface morphologies have superior catalytic properties to traditional polycrystalline gold electrodes[170-173]. However, studies of well-defined ligand-free Au NPs in the nanometer size range (<2 nm), where electronic and geometric finite-size effects play a significant role in catalytic activity and selectivity[79,83], are still missing

Adapted with permission from Mistry, H.; Reske, R.; Zeng, Z.; Zhao, Z.-J.; Greeley, J.; Strasser, P.; Roldan Cuenya, B. *J. Am. Chem. Soc.* **2014**, *136*, 16473. Copyright 2014 American Chemical Society.

for this reaction. This study sets out to fill this critical knowledge gap by exploring catalytic size effects in this important size regime.

In order to elucidate the effect of structure on the CO_2 electroreduction reaction over gold, we synthesized monodispersed Au NPs using the inverse micelle encapsulation method followed by complete ligand removal by an O_2 plasma treatment. The catalytic activity and selectivity toward CO formation during the electroreduction of CO_2 over these catalysts were measured and shown to have a striking correlation with NP size. In order to understand these trends, periodic density functional theory (DFT) calculations of Au NPs in the experimentally relevant size range and Au single-crystal surfaces were performed, revealing the relation between surface atomic coordination and catalytic behavior. Our work has uncovered exceptionally high intrinsic catalytic CO_2 electroreduction activities and previously unexplored size-dependent CO and H_2 selectivities that translate to tunable H_2/CO synthesis gas ratios for use in a variety of different subsequent catalytic transformations.

Experimental Methods

Au NPs with different size were synthesized via inverse micelle encapsulation. Synthesis parameters for the nine samples used in this study can be found in Table 4. The micellar solutions were filtered, and glassy carbon substrates were dip-coated into each solution. In order to remove the encapsulating polymers, the glassy carbon supported Au NPs were cleaned using an O_2 plasma etcher for 20 minutes at 10 W. To increase the NP density on the support, the glassy carbon substrates were dip-coated and O_2-plasma treated a total of three times. Nine identical samples were simultaneously prepared on SiO_2/Si(111). These were measured using

XPS to ensure that the O_2 plasma treatment was sufficient for complete polymer removal by the absence of a C-1s signal. Due to the relative roughness of the support, the nanometer-sized Au NPs deposited on glassy carbon could not be accurately resolved with AFM. Therefore, the SiO_2/Si(111)-supported NPs prepared with the same colloidal solution were additionally used to characterize the NP size and coverage resulting from the multiple dip-coating via AFM.

Table 4. Synthesis parameters for Au NPs, including polymer molecular weight, metal salt to P2VP ratio (loading), particle size as measured by AFM, and surface area of Au normalized by the geometric surface area of the support.

Sample Name	Polymer	Loading	Particle Size h_p (nm)	Surface Area A_{Au} (cm^2_{Au}/cm^2_{geo})
Au1	PS(2600)-P2VP(4800)	0.2	1.1 ± 1.0	0.006
Au2	PS(53400)-P2VP(8800)	0.1	1.4 ± 0.4	0.006
Au3	PS(91000)-P2VP(10000)	0.1	1.8 ± 1.2	0.006
Au4	PS(91000)-P2VP(10000)	0.2	3.2 ± 0.8	0.026
Au5	PS(17000)-P2VP(9800)	0.1	3.3 ± 1.3	0.037
Au6	PS(91000)-P2VP(10000)	0.4	3.6 ± 1.0	0.037
Au7	PS(53000)-P2VP(43800)	0.2	4.3 ± 1.3	0.092
Au8	PS(53400)-P2VP(8800)	0.6	4.9 ± 1.1	0.120
Au9	PS(33000)-P2VP(46000)	0.3	7.7 ± 2.3	0.178

AFM images were acquired using the peak force mode of a Multimode 8 AFM (Bruker). For each sample, the average NP height, h_p, was measured. Assuming spherical particles, the average height was used to calculate the average NP surface area as $A_{Au} = 4\pi(h_p/2)^2$, which was

multiplied by NP density to estimate the total surface area of Au on each sample. All details related to the NP synthesis and size characterization are included in Table 4.

Electrochemical measurements were performed by Prof. Peter Strasser's group (Technical University Berlin, Germany) in an air-tight electrochemical cell with a three-compartment, three-electrode design. A platinum mesh 100 (Sigma Aldrich 99.9 %) formed to a cylinder was used as counter electrode (CE) and a leak-free Ag/AgCl electrode as reference electrode. The glassy carbon samples with Au NPs were contacted with a gold clamp and used as working electrode (WE). The active geometric surface area of the particle-covered support was 3 cm^2. 25 mL 0.1 M $KHCO_3$ was used as electrolyte and purged with CO_2 (30 ml/min) from the bottom of the cell under the WE until a final stable pH of 6.8 was reached. The CO_2 saturation of the gas atmosphere was controlled with an *in situ* mass spectrometer. H_2 and CO were analyzed using a gas chromatography (GC) system.

The working electrodes were immersed into the electrolyte under potential control at E = +0.22 V vs. RHE. A linear voltammetric sweep was performed with a scan rate of -5 mV/s between E = +0.22 V vs. RHE and E = -1.22 V vs. RHE followed by a chronoamperometric measurement at E = -1.22 V vs. RHE for 10 min. At the end of the amperometric step, product gas samples were analyzed. CO_2 gas was bubbling through the electrochemical cell throughout the electrochemical measurements. All potentials are reported with respect to the reversible hydrogen electrode (RHE) and were corrected by the experimental voltage loss (IR-drop) caused by the uncompensated resistances of the electrolyte and external electrical contacts and connections. ICP-OS measurements of Pt ion concentration before and after the electrochemical

experiments showed no detectable evidence of dissolved Pt ions, confirming the lack of any significant dissolution of the Pt anode (counter electrode) during the experiments.

Surface-area normalized catalytic activity and selectivity values were calculated from raw current data by subtracting data measured on a bare glassy carbon support and subsequently dividing by the Au surface area for each sample, A_{Au}, according to Table 4.

Results and Discussion

By means of the inverse micelle encapsulation method[79,96,174,175], nine Au NP samples ranging from 1.1 to 7.7 nm in size were prepared and deposited on glassy carbon. The samples are labeled Au1 to Au9 in order of increasing size. For AFM morphological characterization, the NPs were deposited onto SiO_2/Si(111). Figure 14 shows AFM images of the Au NPs after removal of the polymeric ligands. AFM analysis revealed that the Au NPs had been prepared with narrow size distribution and uniform coverage across the support. Table 4 lists the synthesis parameters and AFM analysis results for each sample. The relative Au surface coverage for each sample determined from AFM (assuming a spherical NP shape with the measured AFM height and NP density) was used to normalize all of the subsequent electrochemical measurements.

The Au NPs deposited onto glassy carbon supports were used as working electrodes for the electrochemical reduction of CO_2 in 0.1 M $KHCO_3$ at pH 6.8. Linear sweep voltammograms (LSVs) measured from E = +0.22 to −1.22 V vs. RHE are shown in Figure 15a after subtraction of a background signal measured on the glassy carbon support and after normalization by the Au surface area. For clarity, only five of the Au samples are shown here. Decreasing the particle size from 7.7 to 1.1 nm resulted in a drastic increase in catalytic activity over a wide range of

potentials. Figure 15b shows the current density measured at E = −1.2 V vs. RHE as a function of NP size for all of the samples. Strikingly, the smallest NPs in sample Au1 displayed over 100 times the activity of the largest NPs. All samples below 5 nm in size showed significantly higher activity than bulk Au, while the largest NPs, Au8 and Au9, showed comparable activity to bulk gold.

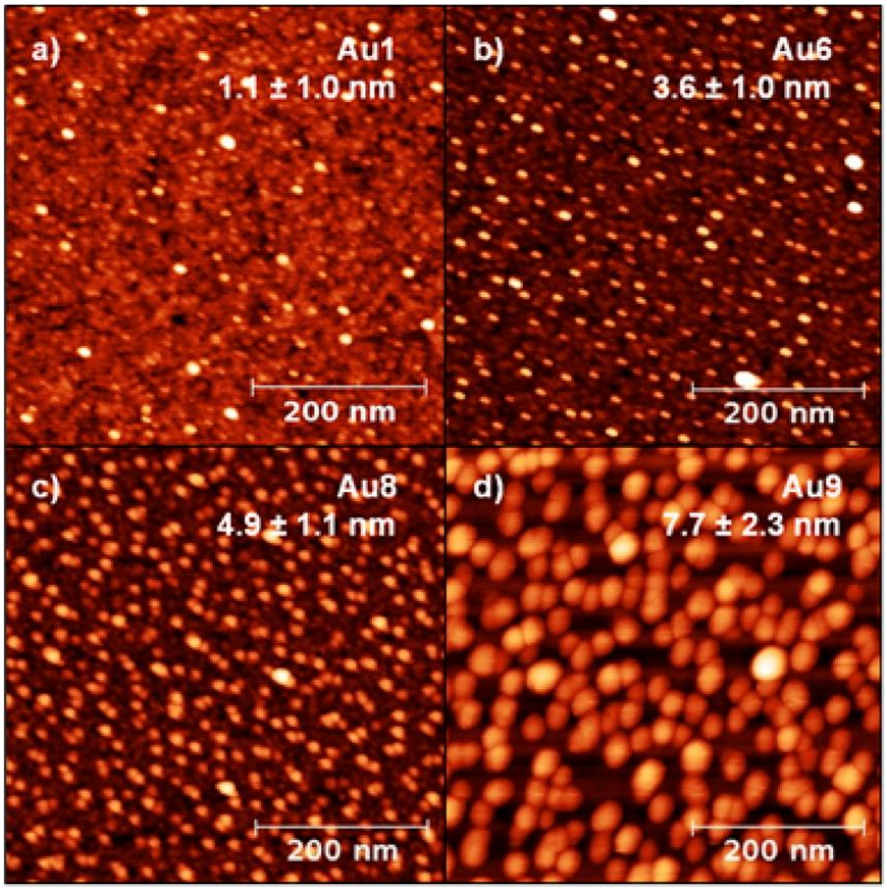

Figure 14. AFM images of four differently sized Au NP samples prepared by inverse micelle encapsulation and supported on SiO_2/Si(111): (a) Au1 (1.1 ± 1.0 nm); (b) Au6 (3.6 ± 1.0 nm); (c) Au8 (4.9 ± 1.1 nm); (d) Au9 (7.7 ± 2.3 nm).

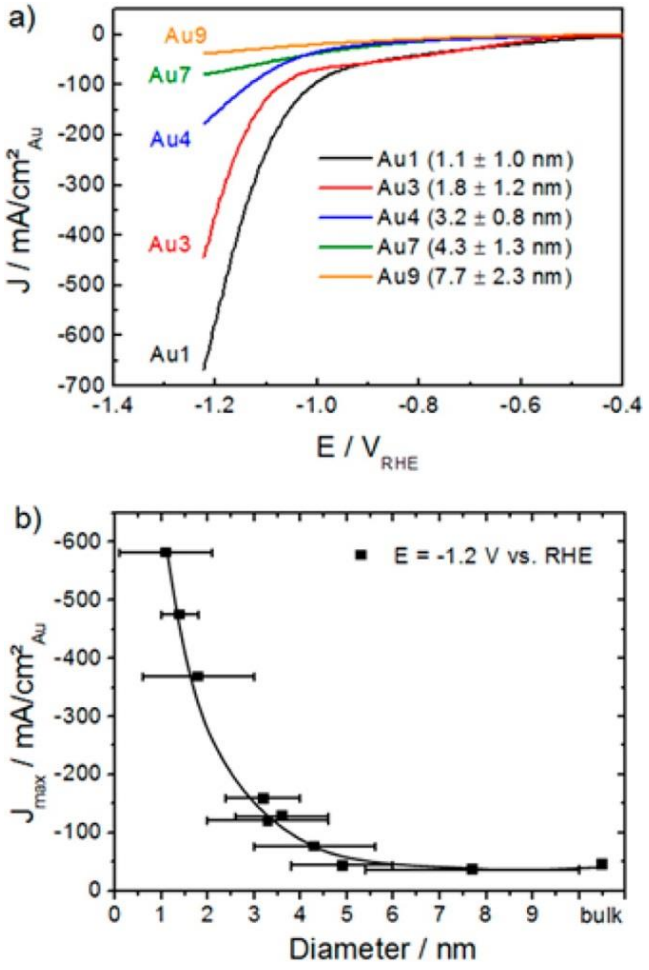

Figure 15. (a) Linear sweep voltammetry of CO_2 electroreduction over Au NP catalyst samples. Data were acquired at room temperature in 0.1 M $KHCO_3$ with a −5 mV/s scan rate and were normalized by the respective Au surface areas after subtraction of a background signal measured on clean glassy carbon. (b) Faradaic current densities at E = −1.2 V vs. RHE as a function of Au NP size, with error bars indicating NP size distributions.

The absolute volume percent of reaction products was measured under steady-state reaction conditions at E = −1.22 V vs. RHE in order to characterize the NP size effect on the reaction pathways. The results revealed that the increase in activity for small NPs below 5 nm is mainly due to a sharp increase in H_2 production (Figure 16a). Figure 16b shows the Faradaic

selectivity as a function of particle size, revealing a clear size effect on the selectivity toward the two reaction products, CO and H_2. While the smallest NPs below 5 nm overwhelmingly favored the production of H_2, the largest NPs (7.7 nm, Au9) showed a sudden increase in selectivity toward CO. The intermediate NP sizes showed an approximately constant Faradaic selectivity toward CO of ∼18%, while Au9 showed the maximum CO selectivity of 45% and Au1 showed a minimum of 9%. Consistent with earlier measurements by Noda[168] and Hori[160,169] (after conversion to the RHE scale), a gold foil measured under identical conditions showed 88.6% Faradaic selectivity toward H_2 and 11.4% toward CO at E = −1.22 V vs. RHE, so that all NP samples except Au1 displayed higher selectivity toward CO than bulk Au. Evaluation of the actual space time yields of CO revealed that Au1 produces more than 8 mL of CO and over 80 mL of H_2 per hour and square centimeter of active surface, corresponding to more than 0.36 mmol h^{-1} cm^{-2} and 3.6 mmol h^{-1} cm^{-2} CO and H_2, respectively, at the applied cell voltage. The H_2/CO molar ratio produced by each sample is plotted in Figure 16c. Changing the size of the catalyst particle enables careful tuning of the H_2/CO ratio in the product stream to acquire the desired composition. NPs below 5 nm in size produce H_2/CO ratios greater than 3, which is ideal for the methane (synthetic natural gas, SNG) synthesis reaction. Between 5–7.5 nm, a H_2/CO ratio of 2 can be inferred by extrapolation, which is suited for methanol synthesis or Fischer–Tropsch processes. At a H_2/CO ratio of 1, which occurs on NPs approximately 7.5 nm in size, the product stream can be used for hydroformylation of alkenes to aldehydes.

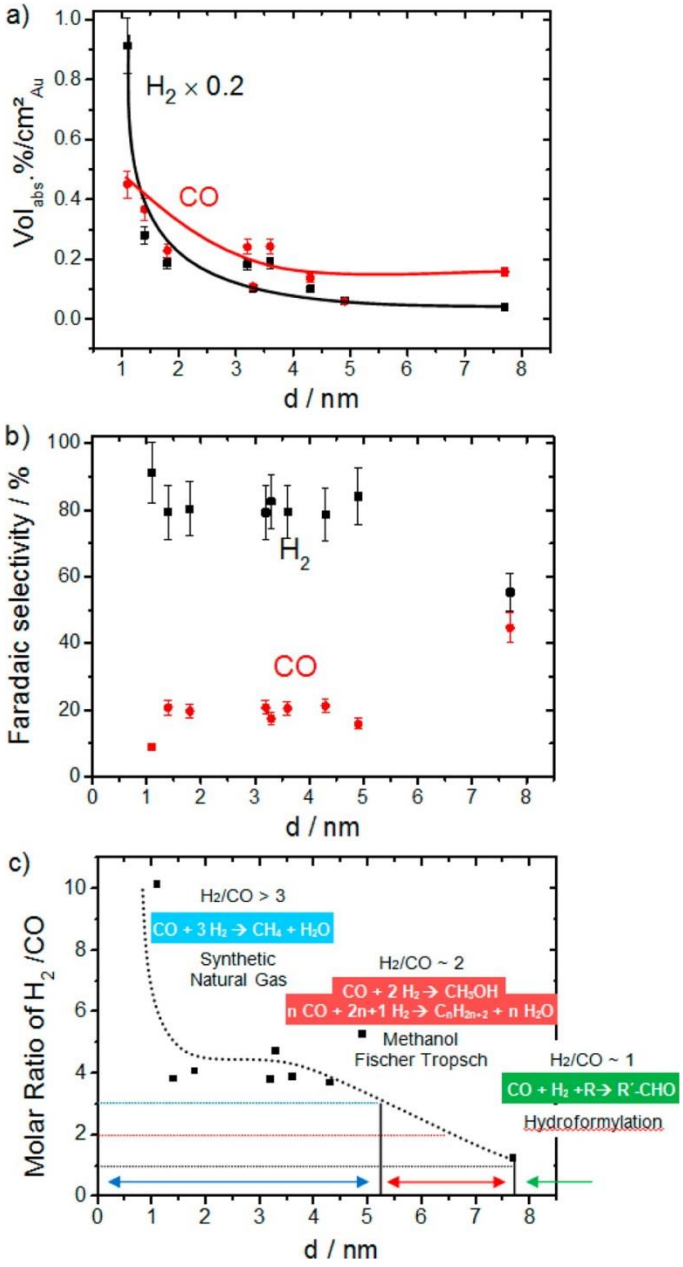

Figure 16. (a) Particle size dependence of the composition of gaseous reaction products (balance is CO_2) during catalytic CO_2 electroreduction over Au NPs. (b) Faradaic selectivity toward H_2 and CO as a function of NP size. Data were acquired in 0.1 M $KHCO_3$ at E = −1.2 V vs. RHE. (c) Ratio of the volume % of H_2 and CO produced at E = −1.2 V vs. RHE as a function of NP size.

The superior catalytic activity of Au NPs less than 5 nm in size is often explained by the increasing ratio of low-coordinated surface sites such as edges and corners[79,83]. These low-coordinated sites allow for stronger binding of reactants or intermediate species, which can lead to increased activity and changes in product selectivity[5]. In order to investigate the population of such active sites on our NPs, model spherical fcc Au structures between 1 and 20 nm in diameter were generated. The population of atoms with CN less than 8 on the NP surface increases significantly for NPs below 2 nm, which is in excellent correlation with the enhanced activity of these NPs shown in Figure 15b.

Cuboctahedral clusters were used as model shapes by Zhu et al.[176] to determine the number of edge and corner sites for given NP sizes in order to establish structure–reactivity correlations. However, their models fail to account for the difference in activity they observed for NPs between 8 and 10 nm, and no experimental data were available for the most interesting samples, namely, those with sizes below 2–3 nm. It is expected that our NPs are spherically shaped with energetically unfavorable low-coordinated atoms present on the NP surface, as opposed to lower-energy facets. As shown below, our smallest NPs (1.1 nm) were also modeled on the basis of structures obtained by DFT.

Size-dependent reactivity was also observed by Kaufmann et al.[171] for CO_2 electroreduction over ligand-protected $Au_{25}(SC_2H_4Ph)_{18}$– clusters (~1 nm) compared with bare 2 and 5 nm Au NPs and bulk Au. They also found that the current density increases with decreasing particle size, but their catalytic activities were an order of magnitude lower than those presented on the present ligand-free Au NPs. Our smallest NPs in sample Au1 (1.1 nm in size) produced H_2 at a rate of 3.6 mmol h^{-1} cm^{-2} at E = −1.2 V vs. RHE. In comparison, Kauffman et

al. reported a rate of approximately 0.01 mmol h^{-1} cm^{-2} for similarly sized ligand-protected Au_{25} NPs at the same potential. The low efficiency for H_2 production on their ligand-protected NPs could be due to blocking of low-coordinated corner sites by the encapsulating ligands, since such sites are expected to favor H_2 evolution. Regardless, because of the low hydrogen yield, ligand-protected Au NPs appear to be unsuitable for the production of industrially valuable synthesis gas.

To further evaluate the effect of NP size on CO_2 electroreduction, DFT calculations were conducted by Prof. Jeff Greeley's group (Perdue University) on several models of both extended Au surfaces and Au NPs, including a Au(111) terrace, a Au(211) step, and Au_{38} and Au_{55} NPs. The results at 0 V vs. RHE are shown in Figure 17. We see that, consistent with previous calculations[177], the CO_2 electroreduction intermediates COOH* and CO* are stabilized on both the steps and NPs compared with Au(111). Similar stabilizing trends are seen for the H_2 evolution reaction (HER) intermediate H*, where ΔG (at 0 V vs. RHE) is reduced from 0.28 eV on Au(111) to 0.21 eV on Au(211) and further to 0.06 and −0.01 eV on Au_{55} and Au_{38} NPs, respectively. Since a good HER catalyst is required to exhibit H* binding that is neither too strong nor too weak, i.e., a ΔG close to 0 V,[178-180] the stabilization of H* on Au NPs implies that Au, a traditionally inert HER catalyst, could actually catalyze this reaction if the NPs are sufficiently small and contain many undercoordinated defects. For the CO_2 electroreduction intermediates, COOH* is stabilized from ΔG = 1.47 eV on Au(111) to 1.27 eV on Au(211) and further to 1.11 and 0.71 eV on Au_{55} and Au_{38}, respectively. These results, calculated at low surface adsorbate coverages, strongly imply that both CO_2 electroreduction and hydrogen evolution proceed at higher rates on small NPs with significant numbers of undercoordinated

surface features compared with extended surfaces, consistent with our NP-size-dependent experimental trends. However, we note that the calculated stabilization of the COOH* energy on smaller NPs is substantially larger than the corresponding stabilization of HER intermediates. Further, the results in Figure 17 suggest both that CO* might accumulate on the small NPs and lead to poisoning and that hydrogen might be present at relatively high coverages on the NP steps and even terraces, at least at the very negative potentials applied in the experiments. These considerations suggest that coverage effects for CO and H might have important consequences for the size-dependent trends in CO_2 electroreduction chemistry.

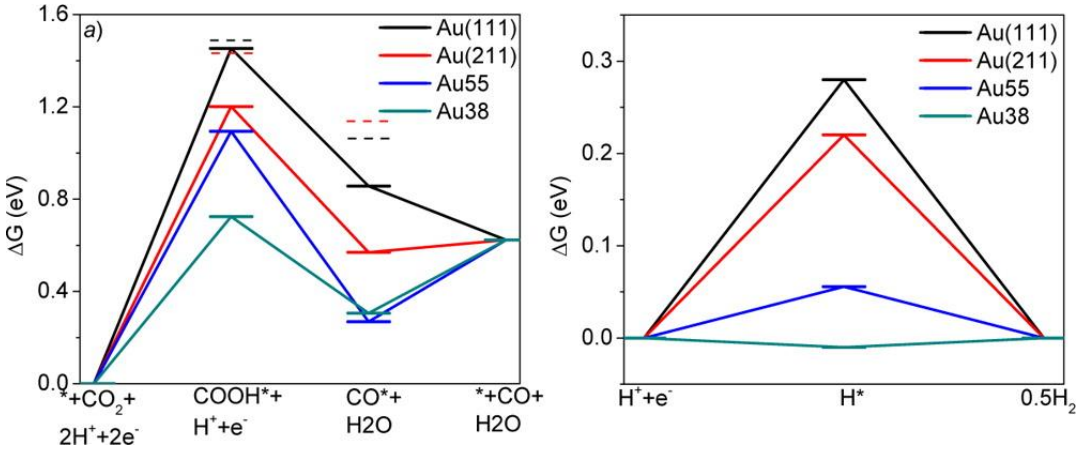

Figure 17. Free energy diagrams for electrochemical reduction of (a) CO_2 to CO and (b) H^+ to H_2 on Au(111) (black lines), Au(211) (red lines), Au_{55} NPs (blue lines), and Au_{38} NPs (cyan lines) at 0 V vs. RHE. The dashed lines are results of calculations performed with a full monolayer of adsorbed H.

A very simple estimate of the coverages of CO* and H* at different potentials can be made using Langmuir adsorption thermodynamics. The isotherms indicate that although the

detailed CO* and H* coverage profiles vary from one surface to the next, the overall trends are very clear and consistent. At potentials higher than −0.3 V, both the surface of Au(211) and the NPs are predominantly covered by CO*. However, H* starts populating the surface at lower potentials and becomes dominant on all surfaces at potentials lower than −0.5 V. At the experimental potential, −1.2 V, it is clear that the surface will be fully covered by H*, which emphasizes the possible importance of the H* coverage effect on CO_2 electroreduction. Although it is challenging to quantify this effect, particularly for small NPs, a basic estimate of its importance may be obtained on the single-crystal surfaces by evaluating the electroreduction energetics in the presence of a full monolayer of adsorbed hydrogen. The results at 0 V vs RHE are given in Figure 17 with dashed lines. For the intermediate CO*, consistent with the isotherm analysis, there is no CO poisoning at low potentials at which surfaces are fully covered by H. For the intermediate COOH*, although the trends are similar to the case with no adsorbed H* (the binding is stronger on Au(211) than on Au(111)), the binding of the intermediates becomes somewhat weaker, and the corresponding energy differences between Au(211) and Au(111) become smaller. If these H coverage effects are somewhat similar on small Au NPs, the increase in CO_2 electroreduction rate with respect to decreased NP size would be mitigated, and consequent enhanced selectivity toward the HER could be observed. Therefore, as the NP size is decreased, CO production likely increases only slightly while H_2 production increases significantly, explaining the increased Faradaic selectivity toward H_2 on smaller NPs.

In addition to the larger population of low-coordinated atoms at the surface of small NPs, quantum size effects responsible for the alteration of the electronic structure may play a role;

however, it is likely that size-dependent changes in surface coordination are the dominant cause of the enhanced activity of our small Au NPs.

Conclusion

Our results demonstrate the exceptionally high activity of ligand-free micellar Au NPs for the electroreduction of CO_2 to CO in aqueous solution. By correlation of activity and selectivity trends with changes in CO_2 reduction and HER energetics, as determined by DFT calculations, the drastic increase in activity observed for NPs below 2 nm can be explained by the increase in the content of low-coordinated sites. Furthermore, our results indicate that changing the size of the NPs enables the adjustment of the H_2 to CO product ratio, allowing for the production of specific chemical feedstocks for different industrial applications. Understanding these structure–activity relationships for catalysts in the nanometer size range is critical for controlling reaction pathways and designing highly active and selective nanostructured catalysts.

Size Dependent Reactivity of Cu Nanoparticles for CO_2 Electroreduction

Introduction

In comparison to Au catalysts, which can electrochemically reduce CO_2 only to CO in aqueous solutions, it is well-known[43,44] that CO_2 can be reduced on copper surfaces producing formate, CO, and hydrocarbons like methane (CH_4) and ethylene (C_2H_4) according to:

$$CO_2 + H_2O + 2e^- \rightarrow HCOO^- + OH^- \quad (7)$$

$$CO_2 + H_2O + 2e^- \rightarrow CO + 2OH^- \quad (8)$$

$$CO_2 + 6H_2O + 8e^- \rightarrow CH_4 + 8OH^- \quad (9)$$

$$2CO_2 + 8H_2O + 12e^- \rightarrow C_2H_4 + 12OH^- \quad (10)$$

Although the standard potentials of CO_2 reduction to CH_4 or C_2H_4 are small and positive (E^0_{CH4} = +0.169 V vs. SHE and E^0_{C2H4} = +0.079 V vs SHE),[181,182] the overpotentials of these reactions are in a range of −800 to −900 mV,[164,182-185] which makes these processes energetically very inefficient. Furthermore, the catalytic selectivities of hydrocarbons are generally relatively small compared to the formation of molecular hydrogen according to

$$2H_2O + 2e^- \rightarrow H_2 + 2OH^- \quad (E^0_{H2} = 0 \text{ V vs. RHE}) \quad (11)$$

In the past few years, several studies have investigated the mechanism of the CO_2 reduction reaction.[162-165,186] It is generally accepted that carbon monoxide (CO) is an intermediate in the reduction of CO_2. DFT calculations put forward by the Norskov group proposed that the protonation of the adsorbed CO to CHO* is the potential determining step (PDS) of methane formation on (211) and (100) surfaces.[164,165] On (111) surfaces, the initial protonation of CO_2 was predicted to dictate the potential requirements. By the same authors, ethylene was predicted to form through a chemical dimerization step of CHO or similar adsorbates. Schouten et al.[162,163] demonstrated experimentally that the Cu(100) surface offers a uniquely active reaction pathway for the formation of C_2H_4 via an electron-mediated dimerization reaction of two adsorbed CO molecules. Dimerization of CO on Cu(111) indeed was unfavorable compared to the protonation of CO to COH.[164,165,186] More recently, Nie et al.[186] proposed that methane and ethylene formation on Cu(111) occurs via a common hydroxyl–methylidyne intermediate, *C–OH, which is subsequently hydrogenated to a common CH_2*

intermediate. That latter adsorbate may undergo a nonelectrochemical dimerization and C–C bond formation toward ethylene or else hydrogenate further to methane.[186]

Controlling the selectivity of the CO_2 reduction reaction and reducing the overpotential for the formation of methane and ethylene are currently major scientific challenges. The geometry, morphology, and roughness of copper single crystal and polycrystalline surfaces have shown a dramatic influence on the catalytic activity and product selectivity during CO_2 electroreduction.[183,185,187] Enhanced ethylene and CO formation was reported on roughened Cu foils.[185] The altered selectivity was rationalized based on differences in the chemisorption characteristics of (111), (100), and (211) surfaces. DFT calculations confirmed that key intermediates, such as *CO and *CHO were stabilized on stepped surfaces owing to more negative chemisorption energies. Vollmer et al. used temperature-programmed desorption (TPD) to study CO adsorption on (i) low index surfaces (Cu(111), Cu(100), and Cu(110)), (ii) stepped and kinked surfaces (Cu(211), Cu(221), and Cu(532)), and on (iii) sputtered and polycrystalline Cu films, concluding that CO binds more strongly on Cu step edges and kinks than on terrace sites.[188]

Chemisorption and catalytic selectivities can also be controlled by lattice strain in thin metal overlayers.[20,22,189,190] This was shown in the electroreduction of CO_2 on thin Cu overlayers on Pt studied using online electrochemical mass spectrometry (OLEMS).[191] Results showed that by decreasing the copper overlayer thickness, the selectivity of C_2H_4 versus CH_4 increased, while the activity decreased.[191] This was explained by the alteration of the chemisorption of reactive intermediates due to geometric lattice effects.

Another well-known morphology-based strategy to tune surface chemisorption and resulting catalytic activities and selectivities is varying the size and/or shape of the catalytically active species, for instance, metal NPs.[79,104,125,129,175] Utilized in practice for centuries, this dispersion dependence is generally known as the "catalytic particle size effect".[104,192,193] For very small NP diameters below around 2 nm, where quantum effects become noticeable,[5,194,195] the effect is often also referred to as the "catalytic finite-size effect".[194] Size effects have frequently been reported for gas-phase catalytic reactions on metal NPs, such as hydrogenations,[196-198] ammonia synthesis,[199] alcohol decomposition reactions,[78] or partial oxidation reactions,[200-208] and CO oxidation on Au NPs.[174,209] Electrocatalytic reactions where size effects have been explored include the oxygen reduction reaction on noble metals,[125,210-215] the oxygen evolution reaction,[216-218](55-58) and electro-oxidation of small organic molecules,[219] as well as electrocatalytic CO oxidation.[56,220,221] The oxygen electroreduction reaction (ORR) on Pt, for instance, exhibits a pronounced particle size effect: Plotted against the particle diameter, the Pt mass-based catalytic activity shows a nonmonotonic dependence with a maximum activity for Pt NPs between 3 and 5 nm in size.[210,213,222,223] To date, reports on NP size effects involving Cu NPs have been limited to heterogeneously catalyzed gas-phase reactions, such as the heterogeneous oxidation of CO in an excess of hydrogen and the catalytic degradation of gaseous carbon tetrachloride.[224,225] The present study is the first exploration of catalytic particle size effects in CO_2 electroreduction on Cu NPs.

Here, we investigate the influence of the size of Cu NPs on the CO_2 electroreduction activity and, in particular, on product selectivity. The copper NPs ranged from 2 to 15 nm in size and gave rise to unexpected selectivity and activity variations. Aside from providing a practical

strategy for deliberately altering activity and product selectivity, this size effect study provides new clues and hypotheses how chemical bonding controls the selectivity in CO_2 electro conversion. Experimental materials, reaction conditions, observables, and their interpretation lend themselves easily to theoretical verification and thus will add important aspects to a more complete mechanistic understanding of such an important energy storage reaction.

Experimental Methods

Size-selected Cu NPs were prepared via inverse micelle encapsulation, see Table 5. Glassy carbon plates were dip-coated into each micellar solution, resulting in a monolayer of NPs deposited on the support. The molecular weight of the polymer tail can be varied to control interparticle spacing. Next, the encapsulating polymers were removed by O_2 plasma etching for 20 min (20 W power). To increase the NP density, the dip-coating and plasma etching (ligand removal) steps were successively repeated 3–4 times on each individual sample. NPs were simultaneously prepared on flat SiO_2(4 nm)/Si(111) supports and underwent the same treatment as the glassy carbon supported NPs. The complete removal of polymeric ligands from Cu/SiO_2/Si(111) samples was demonstrated based on the lack of any C-1s signal in high resolution XPS measurements. However, such measurements are not possible for Cu NPs supported on glassy carbon due to the very strong carbon signal from the support. Nevertheless, since similar micelle prepared NPs (same NP solution) were deposited on both SiO_2/Si(111) and glassy carbon supports, and since the same plasma treatment procedure was carried out on both samples, the complete removal of the polymeric ligands is guaranteed from our XPS measurements on SiO_2/Si(111).

Table 5. Parameters used in the synthesis of size-controlled micellar Cu NPs.[a]

Sample Name	Polymer	Loading	No. of Coats	Particle Size h_p (nm)	Real Cu Surface Area $A_{Cu,norm}$ (cm^2_{Cu}/cm^2_{geo})
S1	PS(26000)-P2VP(4800)	0.2	4	1.9 ± 0.7	0.018 ± 0.001
S2	PS(27700)-P2VP(4300)	0.4	4	2.3 ± 0.8	0.037 ± 0.002
S3	PS(33000)-P2VP(46000)	0.4	3	4.8 ± 1.4	0.110 ± 0.005
S4	PS(33000)-P2VP(46000)	0.4	5	6.7 ± 1.8	0.153 ± 0.008
S5	PS(130000)-P2VP(135000)	0.1	5	13.1 ± 3.5	0.06 ± 0.01
S6	PS(130000)-P2VP(135000)	0.4	5	15.1 ± 5.2	0.07 ± 0.02

[a] Molecular weight of the PS-P2VP polymers, metal-salt to polymer-head ratio (loading), AFM heights with error bars (standard deviation) measured on SiO_2/Si(111) supported NPs, and normalized Cu surface areas calculated from the AFM heights as surface area of NPs/geometric surface area of support, assuming spherical NPs.

AFM images acquired in tapping-mode were used to characterize the NP morphology on SiO_2(4 nm)/Si(111). Average AFM particle heights h_p (size) and support area-normalized NP surface areas, $A_{Cu,norm}$ (in units of cm^2_{Cu}/cm^2_{geo}), were calculated assuming spherical particles, Table 5. The assumption of a spherical NP shape on weakly interacting supports such as SiO_2 or C is based on previous cross sectional transmission electron microscopy studies on similarly synthesized NPs[226]. The surface area of a single particle A_p was estimated according to $A_p = 4\pi(h_p/2)^2$. Using the surface particle density on the flat support, $A_{Cu,norm}$ was evaluated.

Electrochemical measurements were performed by Prof. Peter Strasser's group (Technical University Berlin, Germany). An airtight electrochemical cell with a three-compartment, three-electrode design was used for the electrochemical CO_2 reduction. The

glassware was cleaned in a “nochromix” bath and afterward in concentrated HNO_3 for 1 h, respectively, rinsed with ultra-pure water several times, and dried at T = 60°C in a drying cabinet. A platinum mesh 100 (Sigma-Aldrich 99.9%) formed to a cylinder was used as counter electrode (CE) and a leak-free Ag/AgCl electrode as reference electrode (Hugo Sachs Elektronik Harvard apparatus GmbH).

The glassy carbon plate, on which the Cu NPs were supported, was contacted with a gold clamp and used as working electrode (WE). The geometric surface area, A_{geo}, of the particle-covered support was 3 cm^2. 25 mL of 0.1 M $KHCO_3$ (Roth >99.5%) was used as electrolyte and purged with CO_2 (Air liquid 4.5) (30 mL/min) from the bottom of the cell under the WE until a final stable pH of 6.8 was reached[43]. Before and during the electrochemical measurements, the CO_2 saturation of the gas atmosphere was controlled with an *in situ* mass spectrometer (OmniStar GSD 301c, Pfeiffer). Hydrogen (H_2), carbon monoxide (CO), methane (CH_4), and ethylene (C_2H_4) were analyzed using gas chromatography (GC). The gas chromatograph used was a Shimadzu GC 2016 equipped with a thermal conductivity detector (TCD) and a flame ionization detector (FID). Argon (Air liquid 5.0) was employed as carrier gas. The gaseous products H_2, N_2, O_2, CH_4 and CO were separated in a molecular sieve column (Alltech, part no. 57732, 1.65 m × 1/8 in., molecular sieve 13X, 60/80 mesh) and for C2–C3 hydrocarbons and CO_2 in a HayeSep column (Alltech, part no. 14487, 3.5 m × 1/8 in., HayeSep D, 80/100 mesh).

The working electrodes were always immersed into the electrolyte under potential control at E = +0.22 V/RHE. A linear voltammetric sweep was performed with a scan rate of −5 mV/s between E = +0.22 V/RHE and E = −1.1 V/RHE followed by a chronoamperometric measurement at E = −1.1 V/RHE for t = 10 min. At the end of the amperometric step, product

gas samples were analyzed. CO_2 gas was bubbling through the electrochemical cell throughout the electrochemical measurements to ensure sufficient convective mass transport to keep the Nernst diffusion layer thicknesses to a minimum and minimize mass transport limitations and local pH changes at the electrode interface. All potentials are reported with respect to the reversible hydrogen electrode (RHE) and were corrected by the experimental voltage loss (IR-drop) caused by the uncompensated resistances of the electrolyte and external electrical contacts and connections. ICP-OS measurements of Pt ion concentration before and after the electrochemical experiments showed no detectable evidence of dissolved Pt ions, confirming the lack of any significant dissolution of the Pt anode (counter electrode) during the experiments. In addition, high-resolution XPS measurements confirmed the absence of Pt on the Cu foil or Cu NPs after electrocatalysis, ruling out any possibility of Pt ion cross contamination.

Cu surface-area normalized catalytic activity and selectivity values were calculated from raw current data subtracting coverage-corrected current and selectivity values of bare glassy carbon supports, followed by subsequent division by the real Cu surface area, $A_{Cu,norm} \times A_{geo}$, of the Cu NPs according to Table 5.

To generate spherical Cu NP model shapes, a large FCC structure with a Cu lattice unit (L) of 3.61 Å was constructed using a MATLAB code. When the desired diameter was varied, all the atoms outside the defined sphere were removed from the bulk FCC structure in order to construct each model shape. For the database to be comprehensive, different symmetry centers (SC) were considered with (i) the SC located on one of the Cu atoms and (ii) the SC shifted 0.5L along one of the Cartesian axes (e.g., x-axis). The largest spherical NP considered had a diameter of 18 nm and about 261000 atoms. In the next step, for each model shape in the database, the

coordination number (CN) of all individual atoms was calculated. Atoms with a CN value of 12 were considered as bulk atoms and those with CN below 12 were considered as surface atoms. The surface atoms were also further distinguished based on their coordination number as will be discussed later.

Results

A well-established micelle-based nanoparticle preparation method[79,83,174,227] was utilized to prepare six metallic Cu NP catalysts with spherical shape and different, well-controlled particle height ("size"), henceforth referred to as S1 to S6 in order of increasing size, Table 5. This synthesis method has been known to produce highly reproducible particle sizes, and multiple duplicates of all six NP catalysts were prepared and measured independently. Figure 18 shows AFM images of the spherical Cu NPs after ligand removal.

Analysis of the AFM particle heights revealed that six distinct average NP sizes between 1.9 and 15.1 nm were obtained (see Table 5). Particle size histograms evidenced largely near-symmetric, narrow size distributions. Increasing the molecular weight of the micelle head or increasing the metal loading inside the micelles generally resulted in larger NP sizes. The interparticle distance generally decreased with smaller NP size due to the successive multiple dip-coatings employed in the preparation of such samples in order to ensure sufficient active Cu NP surface and coverage on the carbon support.

The Cu NP catalysts S1–S6 were supported on flat glassy carbon electrodes and were subsequently deployed as working electrode in a three-electrode electrochemical setup designed for the electroreduction of CO_2 in a 0.1 M bicarbonate solution at pH 6.8. The activity and

chemical selectivity of catalysts S1– S6 for CO_2RR were monitored during a slow cathodic potential scan as well as at a constant electrode potential of −1.1 V/RHE. Reproducibility of individual catalytic activity was confirmed and sample averages are provided. Figure 19 displays the Linear Sweep Voltammograms (LSV) of each Cu NP catalyst in comparison to the LSV of a Cu foil electrode (”foil”), which was considered an extended macroscopic Cu reference catalyst. To correct for differences in the electrochemically active real surface area of each Cu NP catalyst, the geometric current density was converted into the Cu surface area-specific current density after the subtraction of the glassy carbon (support) background.

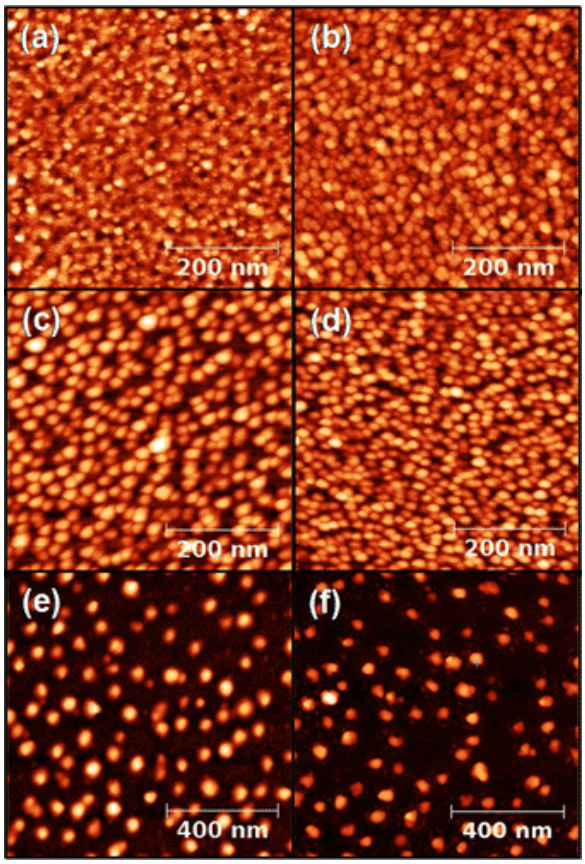

Figure 18. Tapping-mode AFM images of micellar Cu NPs: (a) S1, (b) S2, (c) S3, (d) S4, (e) S5, and (f) S6.

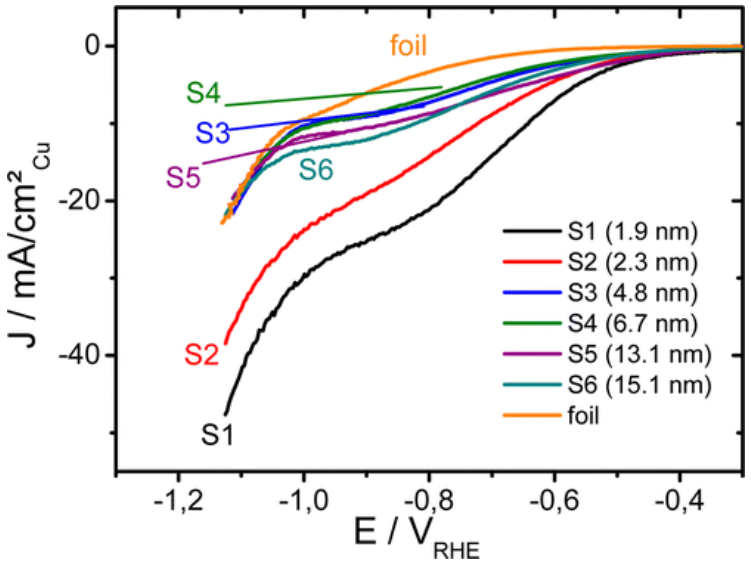

Figure 19. Linear sweep voltammetry of CO_2 electroreduction on Cu NP catalysts, S1–S6, in 0.1 M $KHCO_3$ acquired at room temperature with −5 mV/s scan rate. Current densities are normalized by the Cu particle surface area after subtraction of the glassy carbon background signal. A Cu foil electrode ("foil") is included as reference.

Figure 19 reveals a dramatic particle size effect on the overall catalytic CO_2RR activity of Cu NPs. The LSV of the Cu foil showed the characteristic shoulder between −0.8 and −1.0 V, previously associated with the formation of carbonous surface species. The catalytic LSV currents of the Cu bulk reference in Figure 19 are in excellent quantitative agreement with previous reports of CO_2 reduction on Cu foil electrodes in buffered bicarbonate solutions[43,44,181,228]. The total current of the Cu foil at −1.1 V versus RHE was −23 mA/cm^2, while that reported by Hori[44] under similar conditions was −25 mA/cm^2.

In stark contrast to the Cu foil electrode, the Cu NPs exhibited significantly higher catalytic activity (larger negative current density *J*) as the Cu NP size decreased. The smallest Cu NPs (S1 and S2, ∼2 nm) showed almost twice the catalytic activity of extended bulk Cu, while

catalysts S3–S6 exhibited similar catalytic activities over a wide potential window, ranging between those of bulk Cu and of S2.

Figure 20 highlights the dependence of the overall catalytic CO_2RR activity on particle size at two different electrode potentials, E = −1.1 V versus RHE and E = −1.0 V versus RHE. The data suggest comparable overall activity between bulk Cu and Cu NPs down to about 5 nm, below which an explosive trend toward higher catalytic activity with smaller Cu NP size becomes evident. The smallest Cu NP catalyst (1.9 nm) displayed a 100% increase in faradaic current density (−48 mA/cm$^2_{Cu}$), while the 2.3 nm NP catalyst S2 still showed a 50% increase in activity compared to Cu foil electrode. Together, the observed trends evidence a dramatic activity-enhancing size effect of nanoscale spherical Cu surfaces during CO_2RR.

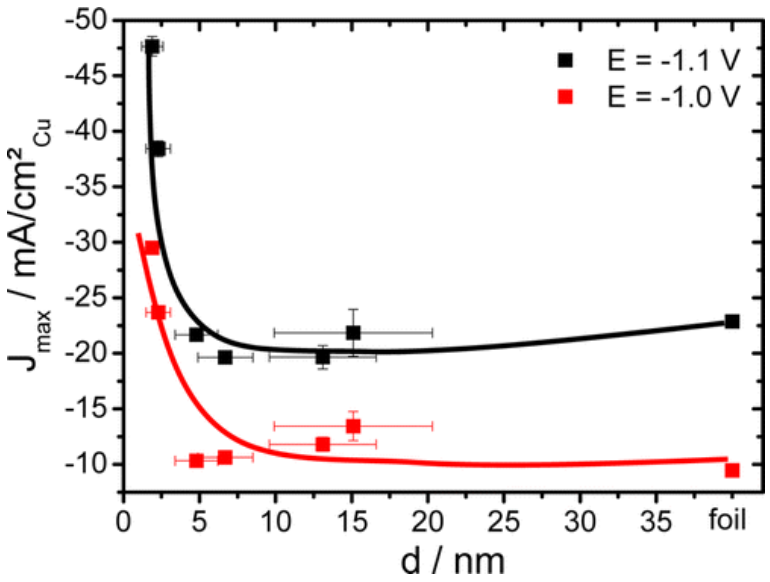

Figure 20. Particle size effect during catalytic CO_2 electroreduction. The faradaic current densities at −1.1 and −1.0 V vs. RHE are plotted against the size of the Cu NP catalysts. The current densities have been normalized by the Cu particle surface area after subtraction of the glassy carbon background signal. Error bars indicate scatter in particle size distributions. Lines are guides to the eye. Data of a Cu foil electrode ("foil") are inserted as reference. Conditions: 0.1 M $KHCO_3$, pH = 6.8, 25 °C.

To obtain insight into the relevant catalytic reaction pathways, faradaic selectivity measurements were performed under stationary reaction conditions at −1.1 V vs. RHE. Figure 21a reports the background-corrected, NP surface area-normalized product composition of the gas stream leaving the working electrode compartment. Each data point represents the average of at least three independent measurements. The excess CO_2 flow keeps the combined volumetric ratios of gas reaction products below 1 vol % for all NP sizes (note that the values of three products are scaled with the factor given in the plot). We note that the absolute volume % values (gas molar ratios) of the reaction products are sensitive to variations in the volumetric CO_2 flow, a shortcoming which is eliminated when relative faradaic selectivities are considered.

It is evident from Figure 21a that major reaction products were hydrogen, CO, methane, and ethylene. While a minute amount of liquid formic acid was detectable for the Cu foil (<5% consistent with results from Hori[44]), no detectable quantities of formic acid were formed for the nanoparticle samples.

The size of the Cu NP catalysts had a significant effect on the formation rate of individual products and, hence, their catalytic selectivity. Larger particles in the 5–15 nm size regime clearly showed much less hydrocarbon formation, and instead yielded more H_2 and CO. Smaller particles below 5 nm displayed a sudden increase in H_2 and CO formation relative to hydrocarbons. It is evident that small Cu NPs, in stark contrast to bulk Cu surfaces, evolve no significant amounts of the highly desired reaction product ethylene.

Taking the number of transferred electrons of each species into consideration, the volumetric ratios were converted into faradaic selectivities, see Figure 21b. We note that the faradaic selectivities of the Cu bulk electrode are in good agreement with earlier reports by

Hori[44]. Methane showed the highest selectivity of 57% (55% reported by Hori), ethylene and hydrogen showing about 20% (25% and 10% reported by Hori), and CO exhibiting less than 5% selectivity (3% reported by Hori).

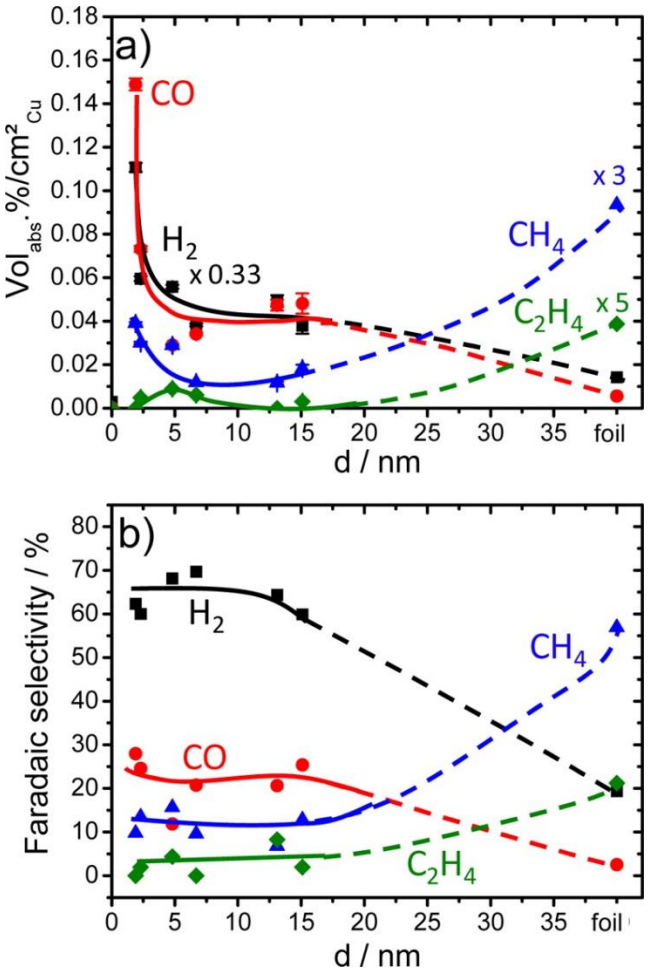

Figure 21. Particle size dependence of (a) the composition of gaseous reaction products (balance is CO_2) during catalytic CO_2 electroreduction over Cu NPs, (b) the faradic selectivities of reaction products during the CO_2 electroreduction on Cu NPs. Lines are guides for the eye. Conditions: 0.1 M $KHCO_3$, E = −1.1 V vs. RHE, 25 °C. For (a), volume concentrations were normalized using the Cu surface areas. Values for H_2, CH_4, and C_2H_4 are scaled by factors of 0.33, 3, and 5, respectively.

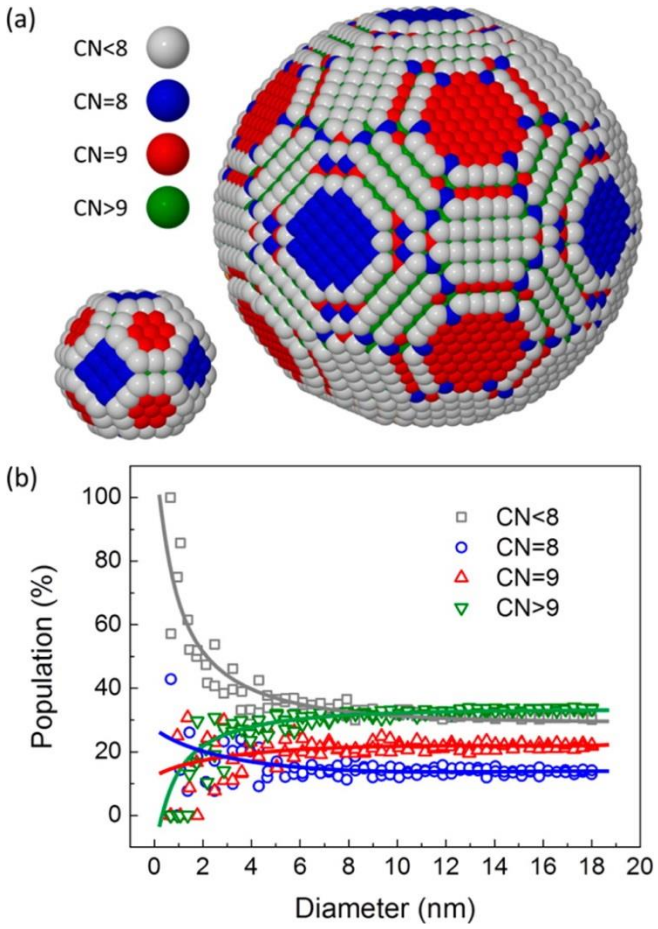

Figure 22. (a) Ball models of spherical Cu NPs with 2.2 and 6.9 nm diameters. Surface atoms are color-coded according to their first neighbor coordination number (CN), CN < 8 (gray), CN = 8 (blue), CN = 9 (red), CN > 9 (green). (b) Population (relative ratio) of surface atoms with a specific CN as a function of particle diameter.

The data in Figure 21b evidence a drastic dependence of the product selectivities on the size of the spherical Cu NP catalysts at a given overpotential. In contrast to the bulk Cu electrode, the selectivity profiles of Cu NPs are largely dominated by hydrogen evolution (60–70% compared to 20% on Cu bulk) over the entire size range considered, a pattern that typically occurs for extended Cu bulk surfaces at much less negative overpotentials. The selectivities of

methane and ethylene dropped drastically from their bulk values to much reduced levels (10–15% for methane and 0–10% for ethylene) in the 5–15 nm particle size regime, while CO selectivities followed the trend of hydrogen and increased from 5% to 20–25%. The anticorrelation between methane and ethylene, on the one hand, and H_2 and CO, on the other, is quite obvious in Figure 21b. At particle sizes below 5 nm, hydrocarbon selectivities dropped again with ethylene formation ceasing on 1.9 nm Cu particles. At the same time, CO selectivity increased to almost 30%.

To gain insight into the origin of the observed particle size effects, model spherical Cu NPs between 1 and 18 nm diameter were considered with a face-centered cubic structure and a unit cell parameter of a = 3.610 Å. Figure 22a illustrates the surface structure of 2.2 nm (left) and 6.9 nm (right) NPs corresponding to catalysts S2 and S4. The percentage ratio of the surface atoms with specific nearest-neighbor coordination numbers (CN) between 5 and 11 were considered and binned into atoms with CN < 8, CN = 8, CN = 9, and CN > 9. Figure 22b breaks down the size-dependent populations of atoms with these four CN groups.

Atoms with coordination 8 (blue), 9 (red), and >9 (green) accounted together for about 70% of the surface atoms of spherical particles between 6 and 18 nm. The contribution of low coordinated atoms (steps and kinks) (gray) increased slightly between 18 and 6 nm, then started to become significant between 6 and 2 nm, and finally drastically augmented for NPs below 2 nm. Below 4 nm, the scatter in the individual populations increased considerably, until, below 2 nm, low-coordinated steps prevailed on the surface of the Cu NPs. The color coding in Figure 22a reflects the location of atoms with individual CN providing an intuitive picture of how the individual CNs are distributed across the surface of the particles. Atoms in Cu(111) and Cu(100)

surfaces have CN values of 9 (red) and 8 (blue), respectively. Also the second layer of atoms in Cu(110) and Cu(211) surfaces have CN of 11 and 10, respectively (green). However, there are a small number of atoms with the mentioned CN values that do not belong to the assigned Cu surface orientation (e.g., 6 blue-colored kink atoms with CN = 8 at the corner of each 111 facet). Nevertheless, the color coding illustrates the complexity of the surface atomic coordination on such spherical particles compared to faceted Wulff-type models (truncated cuboctahedron shape).

Discussion

Structure sensitivity is very common in homogeneous, heterogeneous, electro-, and biocatalysts. However, the dependence of the catalytic activity and selectivity on the catalyst dispersion is an idiosyncrasy of heterogeneous catalysts and heterogeneously catalyzed reactions. This study has explored the effect of the size of spherical Cu NPs on the catalytic activity and selectivity during the mechanistically fairly complex electrocatalytic reduction of CO_2. It is the first of its kind for Cu and CO_2 electrocatalysis, and has revealed a distinctly different behavior of nanoscale Cu surfaces compared to their extended bulk counterparts. A significant increase in the overall faradaic activity was found with shrinking NP size. This was coupled to an increased selectivity for hydrogen and CO, but decreased selectivity for hydrocarbon production. Entering the smallest size domains of particles below 3 nm, hydrocarbon formation drops drastically, while CO is the preferred carbonaceous product.

Stepped extended surfaces have often been considered as models for the behavior of particle surfaces. The effect of steps and kinks on well-defined planar Cu surfaces on the

catalytic activity and selectivity of CO_2RR has first been addressed by Hori and co-workers[43,229]. They reported a high selectivity for ethylene on Cu(100), while methane formation was clearly preferred on Cu(111) facets. Steps in (100) terraces, regardless of their orientation, increased the ethylene formation over methane. Hori's observations were later confirmed by Koper and co-workers[162,163], who found Cu(100) to be highly active and selective for ethylene and proposed a decoupled proton–electron transfer during a dimerization of CO to explain the pH independence of the reaction. More recently, surface morphology effects in CO_2 electroreduction were explored by Tang et al.[185], who found that steps on roughened Cu surfaces show increased ethylene, but very low methane selectivity. Unlike Hori, however, Tang et al. also reported increased CO selectivities on roughened polycrystalline Cu surfaces. Similar to others[164], the authors corroborated their experimental results using thermochemical DFT calculations that suggested stronger chemisorption of CO and CHO intermediates on (211) stepped surfaces as compared to planar (100) or (111) surfaces. These predictions are consistent with earlier experimental studies of CO chemisorption on polycrystalline and stepped single crystals of Cu[188,230,231]. Vollmer et al.[188] reported shifts of CO TPD peaks to higher temperatures as they moved from (111) to (211) and polycrystalline Cu surfaces, indicating stronger CO binding on stepped surface sites. While stepped planar-type surfaces do provide qualitative insight in the effect of steps on reactivity and selectivity, they typically fall short of capturing the more detailed behavior of highly curved NP surfaces.

Another recent computational thermochemical DFT analysis of the CO_2 electroreduction on the stepped Cu(211) surface[165] explored the effect of CO chemisorption on the limiting potential U_L. The limiting potential of an elementary electrochemical reaction step represents the

electrochemical overpotential at which the elementary step becomes exergonic (or downhill in free energy), and can be regarded as a simple measure of the potential where the rate of this step becomes appreciable. The elementary step with the largest U_L dictates the overpotential of the overall reaction. Stronger CO binding was predicted to cause a moderate increase in the U_L of the potential-limiting protonation of CO_{ad} according to $CO_{ad} + H^+ + e^- \rightarrow CHO_{ad}$. This should translate into lower CO protonation rates and lower hydrocarbon selectivities at any constant electrode potential. While this prediction is qualitatively consistent with the present selectivity trends, the dependence of U_L on the CO binding energy appears too weak[165] to account for the sudden selectivity changes in Figure 21.

There is a consensus that NP size effects largely originate from size-dependent surface metal atomic coordination and its corresponding surface electronic structure[56,129,193-195,198]. This is the reason three-dimensional particle models and their surface coordination structure are better suited to help understand particle size effects. A meaningful analysis of surface atomic coordination using particle models requires the selection of structural models that are relevant to the experimental system with respect to size and shape. In the present study, the micelle-assisted, plasma-cleaned NP synthesis initially yielded surface-oxidized Cu NPs, which were subsequently *in situ* electrochemically reduced to metallic Cu NPs, as confirmed by XPS. Since neither thermal treatments nor repeated potential cycling was applied, the present Cu NPs are rather spherical in shape with only limited surface faceting. Unlike faceted models, spherical particle models also include energetically less favorable, higher-index facets and their characteristic coordination. Clearly, this consideration renders highly faceted Wulff-type particle models inappropriate for the present study, and this is the reason why spherical models with

limited faceting were explored in terms of their surface atomic coordination. Coordination numbers (CN) of surface atoms ranged from 5 to 11, where CN 8 atoms could be largely associated with (100) facets, while CN 9 atoms represented (111) facets, see Figure 22a. The present models also exhibit (110) facets and atoms with CNs of up to 11 (green in Figure 22a).

To understand the observed size effects in Figure 21 in more detail, the experimental trends in catalytic activity and selectivity were correlated with the size-dependent surface structure and coordination in Figure 22. We start our discussion with the smallest size regime. The smallest Cu NPs S1 and S2 with sizes around 2 nm showed a dramatic increase in overall catalytic activity, which is attributed to the high ratio of low-coordinated surface atoms (CN < 8) starting as low as CN = 5 for NP diameters below 4 nm, see Figure 22b. In this size regime, particle size effects are often referred to as "catalytic finite size effects", and small variations in size induce drastic changes in the NP's electronic structure, while quantum effects may become non-negligible[5,194]. Following our arguments on stepped surfaces above, step and kink atoms of Cu NPs with such low CNs are expected to exhibit stronger chemisorption of CO_2, CO, atomic H, and CO_yH_x as compared to larger particles or bulk Cu surfaces. Since the reductive adsorption of protons (the Volmer reaction) on free Cu surface sites ($H^+ + e^- + * \rightarrow H_{ad}$) is the rate-determining step of the overall electrocatalytic hydrogen evolution reaction (HER)[179,232], the observed increase in hydrogen production, in hydrogen selectivity, and overall faradaic activity for small NPs appears plausible. A similar argument can be made for those Cu surface orientations where the initial reductive CO_2 adsorption to COOH ($CO_2 + H^+ + e^- + * \rightarrow COOH_{ad}$) is rate-determining[164,165]. Stronger CO_2 adsorption would increase the overall rate of this initial reaction step toward CO.

For Cu particles in the intermediate size range (5–18 nm), the populations of surface atoms with CN = 8 and 9 amount to about 12 and 20%, respectively (see Figure 22b), and remain surprisingly constant over the entire intermediate size range. These population numbers are significantly smaller compared to those found on low-index smooth extended surfaces, such as the (100), (111), or (211) surfaces. With methane and ethylene forming preferentially on (111) (CN = 9) and (100) (CN = 8) sites, respectively[43,162,163], changes in the relative populations of (111) and (100) facets provide a plausible explanation for both the sudden steep drop in faradaic selectivities between Cu bulk surfaces and Cu NPs, as well as the selectivity plateau between 2 and 15 nm discernible in Figure 22.

The distinct selectivity observed when comparing small (2 nm) and large (15 nm) NPs can be explained based on the increase in the strength of the binding of products and intermediate reaction species on the smaller NPs. Strong CO binding on low coordinated sites (small NPs) favors high activity, high CO and H_2 selectivities, and reduced hydrocarbon formation. The latter is understood if the reduced surface mobility of the more strongly bound CO_{ad} and H_{ad} on the NP surface is considered, leading to a lower probability of surface reaction to form hydrocarbons. Instead, it is likely that on small NPs CO_{ad} and H_{ad} desorb before reacting on the Cu surface, which explains the higher yields of CO and H_2 products on these samples. The lower mobility of adsorbed intermediate species on the surface of our small spherical NPs can be assigned to their higher curvature and stepped and roughened surfaces. Thus, on the small NPs, the small hydrocarbon yields detected may be explained based on a different reaction mechanism, as for example, an Eley–Rideal-type one involving the earlier desorption of hydrogen as compared to CO, its diffusion in the liquid phase, readsorption on the Cu surface

near a strongly bound CO atom, and subsequent reaction and desorption in the form of a hydrocarbon. For the large NPs, due to the expected weaker CO and H bonding, their diffusivity on the particle surface might be greater, favoring reaction and hydrocarbon formation without having to involve an additional desorption/liquid phase diffusion/readsorption/reaction pathway.

It should also be mentioned here that we do not have any indication of a CO-poisoning effect for the small NP samples. If that were the case, we would have a decrease in the surface area available for water dissociation, which should lead to a decrease in the yield of H_2, which opposes the present observation.

Li and Kanan[184] recently reported interesting CO_2 electroreduction experiments on Cu oxide electrodes. They achieved significantly increased CO selectivities on electrochemically reduced micrometer-thick Cu oxide films and foils. Following the authors, Cu oxide electroreduction creates a uniquely selective Cu surface. However, for thin Cu oxide layers, this effect vanishes. This is the reason we believe we can exclude the formation of uniquely CO-selective Cu metal phases from Cu oxide particles as origin for the current observations.

In a recent report by Gupta et al.[233], the authors highlighted the role of local pH changes during the CO_2RR. Under the present experimental conditions, the authors predicted a local pH increase near the electrode surface of about 2 pH units at a Nernst layer thickness of 100 μm. This effect would result in a downshift of the zero point of the RHE scale relative to the NHE scale (and along with it a downshift in the thermodynamic equilibrium potentials of coupled proton/electron half-cell reactions). Given our constant applied electrode potential, this would lead to a decrease in the electrochemical overpotential of proton-coupled electron transfer reactions, leading to a smaller hydrogen evolution rate. This is in obvious conflict with our

experimental observations, in which increased hydrogen selectivities and increased current densities were measured for the smallest nanoparticles. We therefore conclude that a strong local pH change is not the origin of the increased faradaic selectivities of hydrogen obtained for our small nanoparticles.

Finally, in recent years, Ono et al.[234] and subsequently Eckle et al.[235-237] advanced a particle density based mechanism to account for stability and selectivity changes in NP ensembles. The role of the interparticle distance on the activity and stability of Au NP catalysts during CO oxidation was investigated by Ono et al., and NP samples with larger distances were found to result in lack of reactive-coarsening for these catalysts, while more closely spaced catalysts experienced drastic morphological changes under reaction conditions[234]. Taking the methanation of CO as a model reaction, Eckle et al. argued that low catalyst particle densities favor desorption of intermediates rather than their subsequent reaction by repeated collision with the catalytic surface. We cannot rule out that this effect might also contribute to the present observations. While in our study the particle density of the most H_2- and CO-selective particle ensembles (smaller size Cu NPs, S1 and S2) is larger than that of the larger Cu NPs (S6) which were found to be less CO-selective, the samples with the smallest NPs also have the smallest total Cu surface coverage (see Table 5). Therefore, readsorption and reaction should also be less favorable on our smallest NP samples. This is an interesting aspect that requires further attention and will be addressed in a separate study where we are systematically changing the interparticle distance while keeping the particle size constant.

In summary, a spherical particle model provided valuable insight into experimental trends in activity and selectivity of CO_2 electroreduction as a function of particle size. An increasing

number of surface atoms with CN below 8 are responsible for enhanced hydrogen and CO evolution on NPs around 2 nm and below. Characteristic changes in the populations of low coordinated sites provide plausible explanations for experimental activity and selectivity variations for NPs between 5 and 15 nm. The smallest Cu NPs at and below 2 nm displayed the most drastic dependence of product selectivities on particle size consistent with a dramatic increase in the content of low-coordinated surface atoms.

Conclusion

The particle size effect has been explored for the catalytic electroreduction of CO_2 on Cu NPs in the size range of 2–15 nm and compared to bulk Cu. Given that this reaction is emerging as one of the most important processes for chemical storage of electricity, knowledge about the reactivity and selectivity of this reaction on nanoscale catalysts is of utmost importance. Nanometer-sized Cu NPs showed a dramatic increase in overall catalytic activity (faradaic current). Selectivity analysis has revealed that enhanced formation of CO and H_2 accounts for the increase in the faradaic activity observed on the Cu NPs. The selectivity of hydrocarbons first changed to a reduced constant plateau, until it virtually vanished for NP sizes at and below 2 nm.

A model of nonfaceted, spherical, and hence experimentally relevant, Cu particles was used to estimate the population of surface atoms with specific coordination numbers. Below 2 nm, a drastic increase in under-coordinated atoms with CN < 8 is observed. These strongly binding sites accelerate the hydrogen evolution and the CO_2 reduction to CO. However, they seem to be unfavorable for the subsequent hydrogenation of CO, which lowers hydrocarbon selectivity at small particles. A plausible explanation for the observed trend is the reduced

mobility of intermediate reaction species (CO and H) on the small NPs due to their stronger bonding, which decreases the chance of further recombination and reaction to form hydrocarbons on the Cu surface.

At intermediate particle sizes, the spherical particle model predicts low and constant populations of (100) and (111) facets, which is consistent with the reduced, yet constant hydrocarbon selectivities observed for Cu NPs between 5 and 15 nm compared to Cu bulk surfaces. For these larger NPs, weaker binding of CO and H is expected, favoring hydrocarbon formation. Clearly, where hydrocarbon yields are of the essence, very small (<3 nm) nanoscale Cu catalysts should be avoided. However, where syngas is the preferred reaction product, for instance, to serve as feed for gas-to-liquid reaction technologies, the size of the Cu particles could serve as a convenient parameter to deliberately control the resulting H_2 to CO product ratio.

Overall, the presented size-dependent selectivity conclusions help obtain a more complete mechanistic understanding of the CO_2 electroreduction process. Catalyst materials, their geometry, and the reaction conditions lend themselves easily to DFT theoretical verification and refined mechanistic interpretation. In particular, this study considers particles below 2 nm, which have become computationally tractable by theorists using ab initio codes. This opens the possibility for further in-depth DFT work on the present system.

CHAPTER SIX: SIZE- AND COMPOSITION-DEPENDENT REACTIVITY OF GOLD-COPPER BIMETALLIC NANOPARTICLES DURING CO_2 ELECTROREDUCTION

Introduction

Alloying is a powerful technique to improve the reactivity of metal nanocatalysts by influencing their morphological, chemical, and electronic properties.[238-240] Alloying may allow for the tuning of the electronic properties of the nanoparticle surface, and consequently its binding strength to different adsorbed species.[241] In addition, bimetallic particles may have unique geometric properties which may enhance their reactivity. For example, the surface of core-shell NPs may be under strain due to lattice mismatch with the NP core, leading to altered binding properties.[22,23] Alternatively, different metal atoms may create a specific ensemble at the NP surface which is the active site for a particular reaction.[29] Since the reactivity of bimetallic NPs will depend on the structure, composition, and chemical state of the surface, thorough characterization of the properties is critical in order to gain insight into their behavior. However, it is well known that under reaction conditions, nanocatalysts may evolve due to chemisorption of reactants, to the environmental temperature or pressure conditions, or the presence of an electrolyte or applied potential.[35,37,223,242,243] Therefore, *operando* measurements of a catalyst in its working state are highly important, particularly for understanding reactivity mechanisms on bimetallic catalysts, which have an added layer of complexity with the addition of a second metal.

One reaction where alloyed catalysts may provide remarkable improvement in catalyst activity and selectivity is the electroreduction of CO_2. Currently, Cu shows the most promise as a

catalyst for this reaction since it can produce hydrocarbons, but only at high overpotentials.[1,44,228,244] Au is also a promising material since it can selectively generate CO at moderate overpotentials.[169,245] Despite these results, low-cost catalysts with high selectivity and efficiency for CO_2 reduction to valuable products are yet to be discovered.

Using density functional theory (DFT), Hansen et al. have shown that the unique hydrocarbon selectivity of Cu can be linked to its optimal binding to the CO* and COOH* intermediates in comparison to other metals.[166] These results indicate that the reactivity of Cu could be further improved by tuning its binding properties to different intermediates, although the scaling relations between these binding energies must first be broken.[246] Several strategies for achieving this have been proposed, including nanostructuring the Cu surface[247] or adding ligands to an active metal center,[248] but the most promising may be introducing a secondary metal to create an alloy catalyst.[165,246]

Recently, several experimental and theoretical studies have explored the reactivity of bimetallic catalysts during CO_2 electroreduction.[28,191,249-257] In particular, several studies have focused on copper-gold bimetallics, due to the reactivity of both of these metals.[187,242,249,258-265] Composition dependent studies on bulk Au-Cu alloys and 10 nm Au-Cu nanoparticles (NPs) indicate that hydrocarbon production is favored with increasing Cu content, although not surpassing that of pure Cu, while increasing Au content favors an increase in CO selectivity.[259] In order to understand the reactivity of AuCu bimetallic catalysts, it is crucial to understand the structure and stability of the catalysts during the reaction. Monzó et al. investigated Au core Cu shell NPs for CO_2 electroreduction, arguing that trends in reactivity may be explained by strain effects in the Cu shells of different thickness.[261] However, it is important to consider that Cu

monolayers on an Au surface can be highly unstable under electrochemical conditions, and Au may segregate to the surface and alloy with Cu.[260,266] In addition, previous studies on AuCu CO_2 electroreduction catalysts have been restricted to bulk-like surfaces[187,265] or NPs 10 nm or larger in size,[259,261-263] although NPs smaller than 10 nm are known to have widely different reactivity than their bulk counterparts.[2,3] It is also important to consider the oxidation state of the metals in the NP surface and its evolution during the reaction, since oxide derived Cu nanostructures have shown widely improved reactivity during CO_2 electroreduction,[184] and a secondary metal may alter the stability of such oxides.

In this study, we address the adsorbate-driven restructuring and structure-dependent reactivity of AuCu bimetallic NPs for CO_2 electroreduction using well-defined model NP catalysts less than 10 nm in size. NPs in the size range from 1.4 to 24 nm were synthesized using inverse micelle encapsulation and characterized using microscopy and X-ray spectroscopy. In addition, 1.4 and 4.8 nm NPs were characterized using AP-XPS in order to study the segregation and chemical state of the NPs under different environments. During CO_2 electroreduction, although a significant increase in activity was found for smaller NPs, the selectivity was found to have only slight size dependence, in stark contrast to monometallic Au and Cu NPs.

Experimental Methods

Monodisperse AuCu bimetallic NPs were synthesized using the inverse micelle encapsulation technique, see Table 6. The resulting metal loaded micelle solutions were dip-coated onto the support (silicon wafers or glassy carbon), and then the encapsulating polymers were removed using 20 min of oxygen plasma at 20 W. The absence of the C 1 s signal in XPS measured on silicon wafer-supported samples was used to ensure the plasma etching conditions

were sufficient to completely remove the polymers. For the synthesis of the electrodes, the dip-coating and plasma etching steps were repeated three times to increase the loading of NPs on the glassy carbon.

AFM was used to determine NP size, interparticle distance, and geometrical surface area of our NP catalysts. AFM was acquired using a Digital Instruments Nanoscope-III microscope on ligand-free AuCu NPs dip-coated onto SiO_2/Si(111) wafers. The interparticle distance d was estimated as $d = \frac{1}{\sqrt{\sigma}}$ by measuring the NP density σ and assuming hexagonal arrangement. The metal NP surface area was estimated by using the NP height and NP density from AFM and calculating the NP surface area per area of support, assuming spherical NPs. The latter was used as geometrical metal surface area for the normalization of the electrochemical currents.

XPS was measured with a monochromatic Al Kα source (1486.6 eV) in an ultra-high vacuum (UHV) system with 2 × 10−10 mbar base pressure (Phobios 150, SPECS GmbH). Data were aligned to the Si^0 2p peak at 99.3 eV. XAFS was measured at beamline 10-ID-B of the Advanced Photon Source at Argonne National Laboratory. For XAFS, 7.9 nm AuCu NPs supported on a carbon foil were measured in air in fluorescence geometry at the Cu K and Au L_3 edges. Data were analyzed using the Athena and Artemis software from the IFEFFIT package,[98] and fitting was performed using FEFF 8 calculations.[60]

Ambient pressure XPS measurements were performed at NSLS I at BNL, at the X1A1 endstation. A SPECS Phobios 150 electron analyzer was used with a differentially pumped lens system to allow measurements in up to 1 Torr of gas. 1.4 ± 0.7 nm NPs with $Au_{48}Cu_{52}$ composition, and 4.8 ± 1.2 nm NPs with $Au_{60}Cu_{40}$ composition were used for ambient pressure XPS. Measurements were performed at X-ray energies of 295, 479, 523, and 777 eV, which

result in Au 4f and Cu 3p photoelectrons with approximately 214, 398, 442, and 696 eV kinetic energies (KE), respectively. XPS data analysis was performed using the CasaXPS software. Spectra were aligned to the Si^0 2p peak at 99.3 eV. To calculate Au/Cu ratios, the peak areas of Au 4f and Cu 3p regions were normalized by the photoionization cross sections.[267]

CO_2 electroreduction was performed by Prof. Peter Strasser's group (Technical University Berlin, Germany) in a three electrode electrochemical cell. A platinum mesh 100 was used as counter electrode, and a leak-free Ag/AgCl electrode was used as reference electrode. The working electrode was the AuCu NPs supported on glassy carbon plates. The electrolyte was 0.1 M $KHCO_3$, and CO_2 was bubbled at a constant flow rate of 30 mL/min from the bottom of the cell (pH = 6.8). Every measurement was started with a linear voltammetric sweep performed with a scan rate of −5 mV/s between E = +0.05 VRHE and the working potential (−1.2 VRHE), followed by a chronoamperometric step for 10 min. Gas products (H_2, CO, and CH_4) were monitored using a gas chromatograph (Shimadzu GC 2016) equipped with a thermal conductivity detector (TCD) and a flame ionization detector (FID). The products were measured at −1.2 VRHE to ensure high enough production rates for reliable GC detection over our low loading samples. The signal from a blank glassy carbon electrode was subtracted from all electrochemical data shown here.

Nanoparticle Characterization: AFM, XAFS, and XPS

For this study, AuCu NPs ranging from 1.4 to 24 nm in size were synthesized using an inverse micelle encapsulation method. Since the surface of the glassy carbon electrodes is rough, the NPs were deposited onto silicon wafers to accurately characterize their morphology using AFM. Figure 23 shows AFM images of three coats of AuCu NPs supported on SiO_2/Si(111).

Table 6 lists the synthesis parameters used for the five samples, along with the morphological parameters acquired from AFM including the NP size, interparticle distance, and the surface area used for normalization of the electrochemical data. The AFM results show that the NPs could be synthesized with a high degree of size control, and narrow size distribution was achieved for the four smaller NP sizes. The largest 24 nm NPs had a wider size distribution and resulted in a bimodal size distribution.

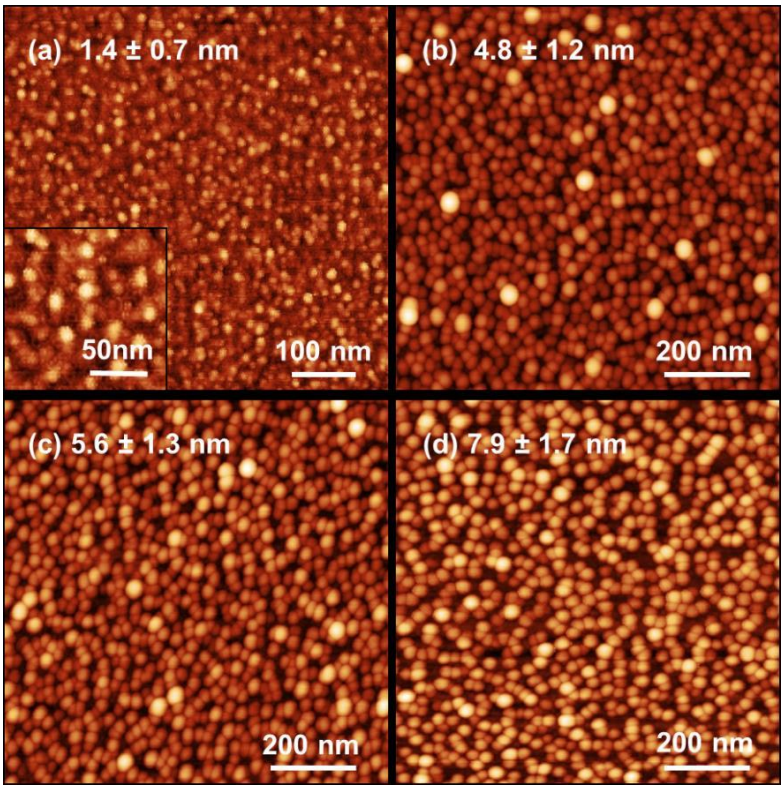

Figure 23. AFM images of bimetallic AuCu NPs supported on SiO_2/Si(111). (a) 1.4 ± 0.7 nm (enlarged region shown in inset), (b) 4.8 ± 1.2 nm, (c) 5.6 ± 1.3 nm, and (d) 7.9 ± 1.7 nm.

Table 6. Synthesis parameters and size characterization of bimetallic AuCu NPs prepared via inverse micelle encapsulation: polymer size, loading (metal salt to P2VP ratio), NP size measured from AFM, metal surface area assuming spherical NPs (cm^2 of metal per cm^2 of support), interparticle distance, and NP composition derived from XPS.

Polymer weight	Loading	NP Size (nm)	Surface Area	Interparticle Distance (nm)	Composition
PS(9,800)-P2VP(17,000)	0.1	1.4 ± 0.7	0.0458	12.9	$Au_{48}Cu_{52}$
PS(43,800)-P2VP(53,000)	0.2	4.8 ± 1.2	0.100	27.7	$Au_{60}Cu_{40}$
PS(46,000)-P2VP(33,000)	0.2	5.6 ± 1.3	0.107	31.4	$Au_{34}Cu_{66}$
PS(70,000)-P2VP(48,500)	0.2	7.9 ± 1.7	0.148	37.4	$Au_{63}Cu_{37}$
PS(135,000)-P2VP(130,000)	0.4	24 ± 6	0.145	75.7	$Au_{44}Cu_{56}$

XPS was used to characterize the composition and chemical state of the NPs in their initial as prepared state. The composition of the NPs was determined by quantifying the Au 4f and Cu $2p_{3/2}$ peaks measured on the as prepared NPs supported on SiO_2/Si(111). Close to 50-50 Au-Cu composition was calculated for each sample, as shown in Table 6. It should be noted that XPS is a surface sensitive technique and may not probe the bulk of the larger NPs.

XPS was also used to investigate the oxidation state and alloying of the Au and Cu in the NPs. Figure 24 shows the Au 4f and Cu 2p core level regions measured on the 7.9 nm AuCu NPs supported on SiO_2/Si(111). Figure 24a and b shows data acquired immediately after ex situ O_2 plasma treatment and transfer in air to the UHV system for XPS measurement. After O_2 plasma, the Au 4f region shows mainly Au^{3+} peaks, indicating that the NPs contained mostly Au_2O_3 species. Small Au^0 peaks were also measured, and the Au^0 $4f_{7/2}$ peak agrees with bulk metallic gold at 83.9 eV. The Cu 2p region shows only Cu^{2+} species with the characteristic satellite peaks

at higher binding energies. Only the Cu $2p_{3/2}$ peaks were fit, since a sloped background exists at high binding energies due to overlap with the O LMM Auger lines. The Cu $2p_{3/2}$ peak can be deconvoluted into two peaks which agree with CuO and $Cu(OH)_2$ species. These results show that the NPs are heavily oxidized in their as prepared state due to the O_2 plasma treatment employed during the synthesis.

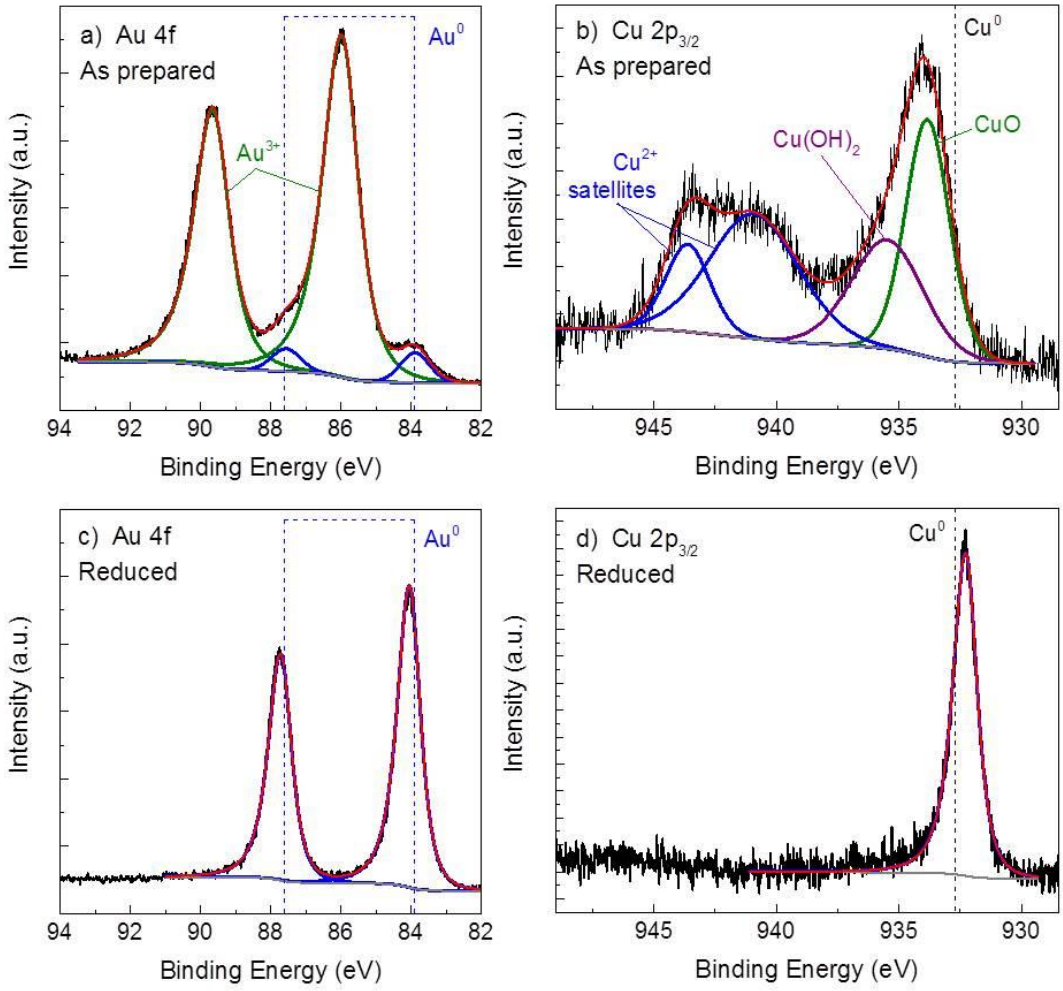

Figure 24. XPS data of the (a,c) Au 4f and (b,d) Cu 2p core level regions of 7.9 nm AuCu NPs supported on SiO_2/Si(111). The spectra were measured of the same sample in its as prepared state (a,b), and after *in situ* reduction (c,d).

In order to confirm that true alloyed NPs were formed, the oxidized NPs were thermally reduced under mild reducing conditions *in situ* so that binding energy shifts due to alloying could be detected with XPS. XPS was measured on the 7.9 nm AuCu NPs/SiO_2/Si(111) after annealing *in situ* for 20 min at 275 °C in UHV. Figure 24c and d shows the Au 4f and Cu 2p regions of the sample after *in situ* reduction. The Au 4f region in Figure 24c shows that the Au has been reduced to metallic Au, with an Au $4f_{7/2}$ binding energy of 84.0 eV. The Cu 2p region also shows reduction of the Cu^{2+} species with a Cu $2p_{3/2}$ peak binding energy of 932.3 eV. A negative binding energy shift exists with respect to bulk metallic Cu at 932.7 eV. Bulk alloys of Au and Cu have shown a positive binding energy shift of 0.1 to 0.5 eV in Au 4f, and a negative shift of approximately 0.1 to 0.4 eV in Cu 2p.[268] The positive binding energy shifts in Au 4f are due to transfer of d charge from Au to Cu, although overall Au gains charge due to its electronegativity. Similarly, Cu gains d charge causing the negative binding energy shifts in Cu 2p.[268] Therefore, our results indicate that Au-Cu alloyed NPs were synthesized.

The 7.9 nm AuCu NPs were also supported on carbon foil and measured in their oxidized as prepared state using XAFS to gain information on the structure and chemical state. Figure 25 shows XANES and EXAFS of this sample measured at the Cu K and Au L_3 edges. The XANES spectrum at the Cu K edge (Figure 25a) shows the features of CuO species, in agreement with XPS measurements. Table 7 and Figure 25b show fit results for the Cu K edge EXAFS. EXAFS fitting gave a Cu O bond distance of 1.95 ± 0.01 Å, also in good agreement with CuO structure. No Cu Cu bonds could be fit, indicating the copper in the NPs was heavily oxidized. The Au L_3 edge XANES spectrum of the sample, shown in Figure 25c, shows a white line feature indicating the presence of Au^{3+} species in Au_2O_3. Fit results for the Au L_3 EXAFS are also given in Table 7

and plotted in Figure 25d, indicating an Au-Au path with CN = 10, and an Au-O path with CN = 0.6. In agreement with XPS, XAFS measurements revealed that the initial samples are heavily oxidized and likely initially composed of segregated oxidized Au and Cu grains, since no AuCu path could be fit.

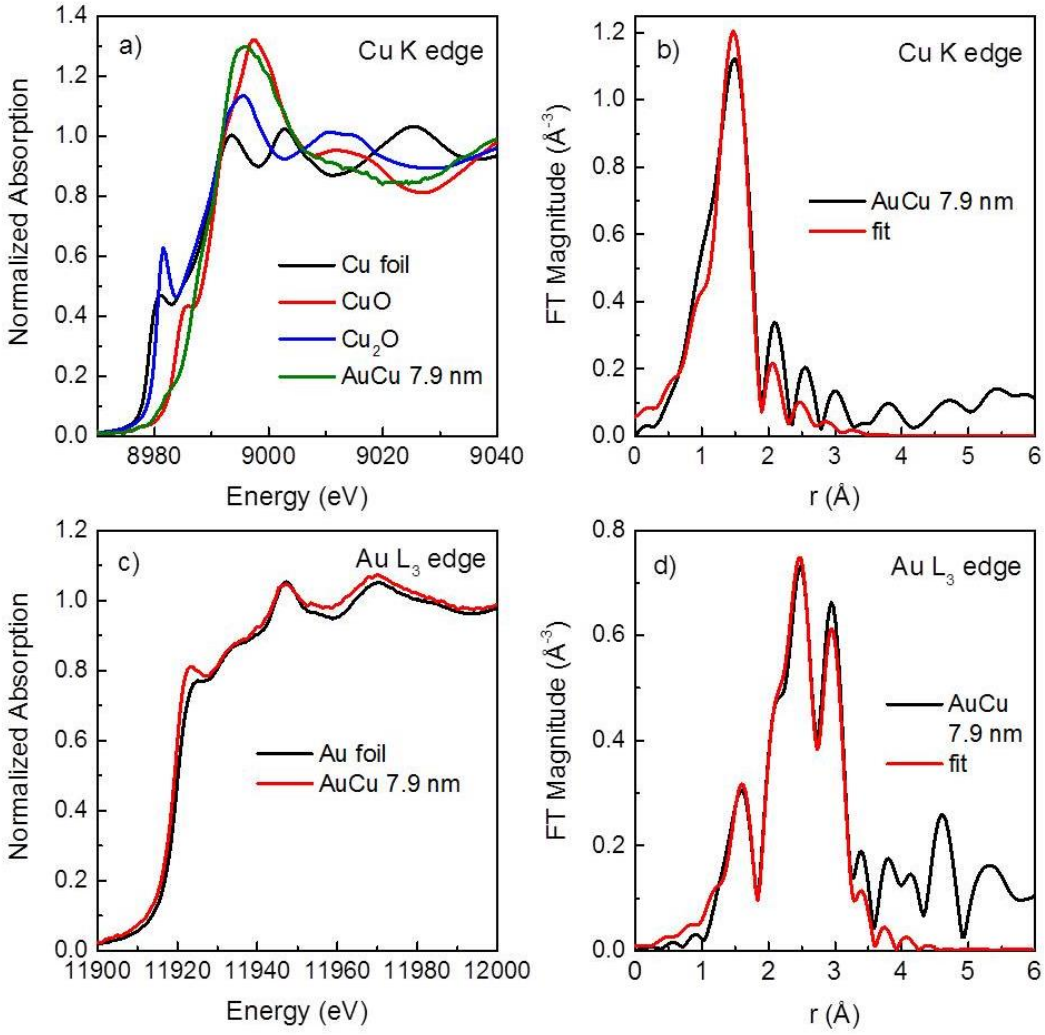

Figure 25. XAFS measurements of as prepared 7.9 nm AuCu NPs supported on carbon foil. (a) XANES spectrum of the AuCu NPs and bulk Cu foil, CuO and Cu_2O references at the Cu K-edge. (b) k^2-weighted EXAFS spectrum of Cu references, AuCu NPs, and fit at the Cu K edge (Fourier transform k range 2.5–10.5 Å). (c) XANES spectrum of the AuCu NPs and Au foil at the Au L_3 edge. d) k^2-weighted EXAFS spectrum of Au foil, AuCu NPs, and fit at the Au L_3 edge (Fourier transform k range 2.5–12 Å).

Table 7. EXAFS fit parameters: coordination number (CN), bond length (r), and disorder parameter (σ^2) for the Cu K edge and Au L_3 edge of as prepared 7.9 nm AuCu NPs supported on carbon foil.

Path	CN	r(Å)	σ^2 (10^{-3} Å^2)
Cu–O	3.2 ± 0.5	1.95 ± 0.01	2 ± 2
Au–Au	10 ± 1	2.854 ± 0.007	9 ± 1
Au–O	0.6 ± 0.2	2.00 ± 0.03	1 ± 4

AP-XPS Measurements of Adsorbate-Driven Restructuring

AP-XPS measurements were performed on the 1.4 and 4.8 nm AuCu alloy NPs with close to 50-50 composition supported on silicon wafers. AP-XPS was measured on the NPs under different environmental conditions at various incident X-ray energies in order to probe different depths into the NPs and monitor segregation phenomena. XPS spectra were measured on the NPs as prepared (after ex situ O_2 plasma cleaning) in UHV at room temperature, in 1 Torr O_2 at 300 °C after 1 hour, then in 1 Torr H_2 at 450 °C after 30 min. Figure 26(a) and (b) show the Au 4f and Cu 3p spectra measured on the 4.8 nm AuCu NPs under 1 Torr O_2 at 300°C with KE = 442 eV. Figure 26(c) and (d) show the Au/Cu ratio calculated from the XPS spectra measured at different photoelectron kinetic energies under different conditions for (c) the 1.4 nm NPs and (d) the 4.8 nm NPs. The smallest kinetic energy electrons measured here have a inelastic mean free path (IMFP) of about 0.5 – 0.6 nm, while the largest kinetic energy electrons have a IMFP of around 1.0 – 1.3 nm (depending on if the medium is Au or Cu), meaning that the core of the 4.8 nm NPs will not be probed by these measurements. For the smaller 1.4 nm NPs, the IMFP of the highest kinetic energy photoelectrons (1.0 – 1.3 nm) is similar to the NP size, meaning that it is possible for the bulk of the NP to be measured, however these measurements at the highest

energy may be weighted more to the species which is at the surface. This may explain why the calculated Au/Cu ratio is not 1 at the highest kinetic energy.

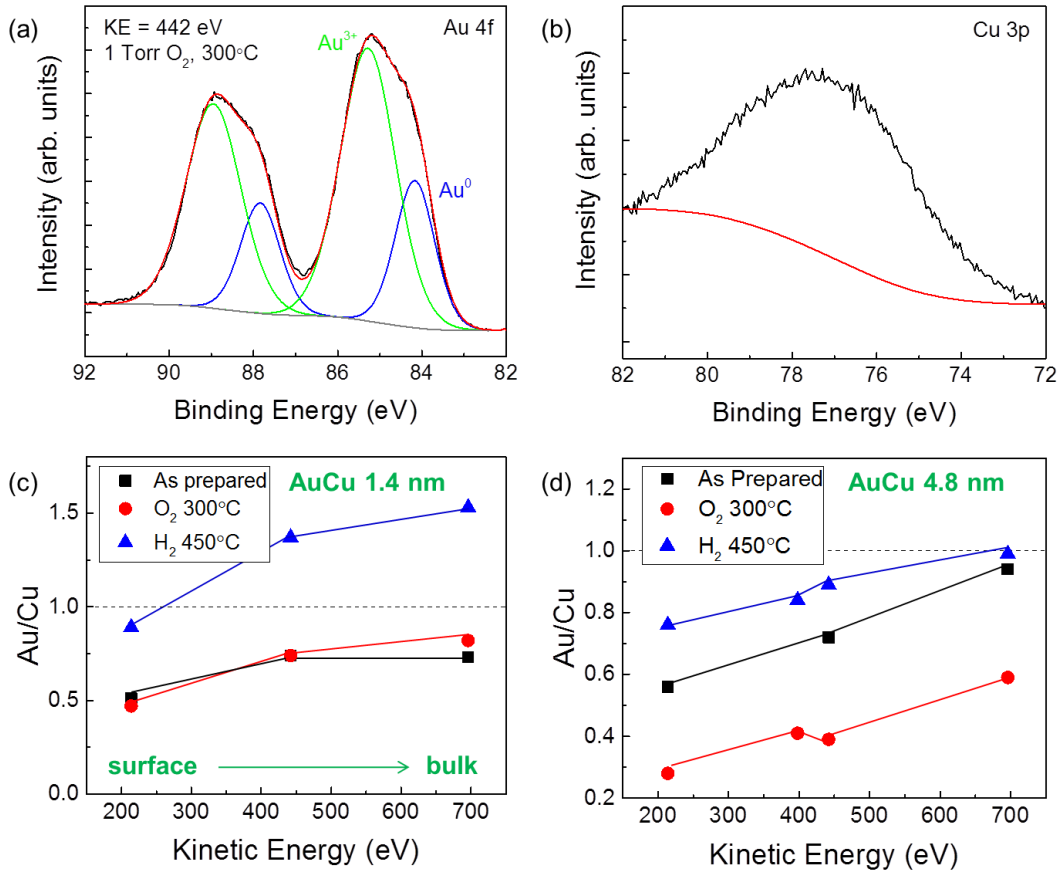

Figure 26. (a) Au 4f and (b) Cu 3p spectrum measured on 4.8 nm AuCu NPs in 1 Torr O_2 at 300 °C at KE = 442 eV. (c) Ratio of Au to Cu as a function of photoelectron kinetic energy for (a) 1.4 nm AuCu NPs and (b) 4.8 nm AuCu NPs in UHV (as prepared), in 1 Torr O_2 at 300 °C, and in 1 Torr H_2 at 450 °C.

For both NP sizes, Figure 26 shows that initially there is overall a higher fraction of Cu (Au/Cu ratio below 1), and the fraction of Cu is highest at the very surface of the NPs (smaller

kinetic energy photoelectrons). In the oxygen environment, no change is seen in the 1.4 nm NPs, while in the 4.8 nm NPs, a smaller Au/Cu ratio is seen, indicating that Cu segregates outward. In the H_2 environment, the Au/Cu ratio increases for both NP sizes, indicating the outward segregation of Au atoms. Interestingly, for the 4.8 nm NPs, the surface is still Cu rich in the H_2 450 °C environment. However, this measurements was performed after 30 minutes under these conditions, and a longer time may have been necessary to allow further segregation of Au to the surface.

Several mechanisms may be driving the segregation observed in these NPs. Previous results have shown that for our micellar AuCu NPs, in their as prepared state after O_2 plasma cleaning the NP surface is heavily oxidized, with Cu entirely in the Cu^{2+} state and a mixture of Au^0 and Au^{3+} present.[4] Under an O_2 atmosphere at 300 °C, it is likely that the NPs will become further oxidized, and the segregation of Cu to the surface under these conditions may be driven by the higher affinity of Cu for oxygen compared with Au. The absence of any change between the 1.8 nm NPs in the as prepared state and in the oxidizing conditions could be explained if the NPs are already completely oxidized in their initial state, with a shell of CuO surrounding an Au/Au_2O_3 core. The larger 4.8 nm NPs may still contain some metallic Cu within the core which can still migrate outwards and become oxidized under oxidizing conditions. Conversely, in the reducing H_2 environment, the oxides in the NPs will reduce, and Au preferentially segregates to the surface. This phenomenon may be driven by the larger atomic radius of Au atoms compared to Cu and the comparatively lower surface energy of Au.[269]

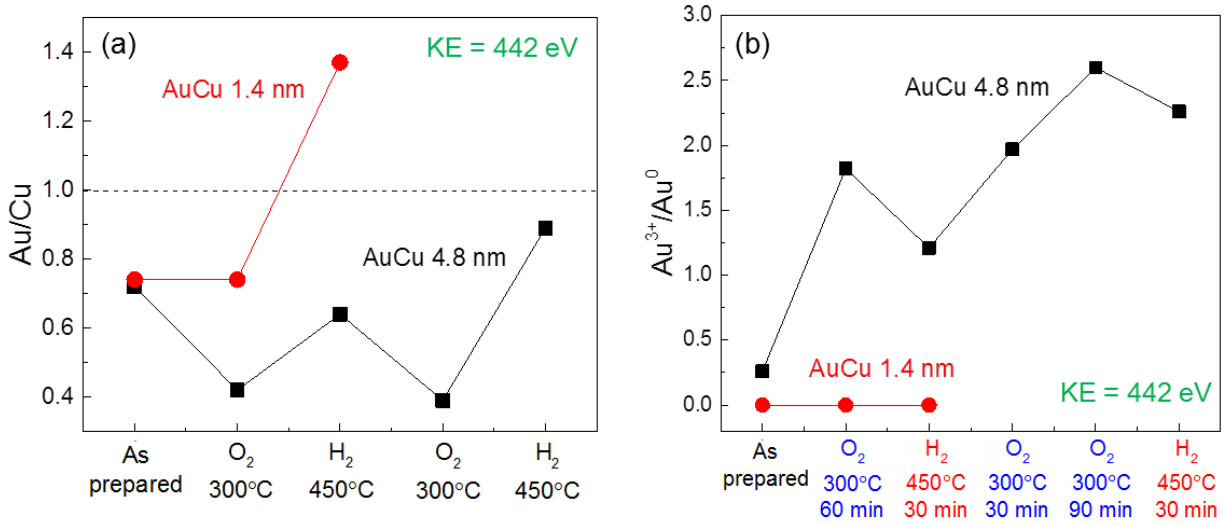

Figure 27. (a) Ratio of Au to Cu for 1.4 and 4.8 nm AuCu NPs under different environmental conditions at 442 eV photoelectron kinetic energy. (b) Ratio of Au^{3+} to Au^{0} for AuCu NPs under different environmental conditions at 442 eV photoelectron kinetic energy.

In order to further probe the stability and oxidation state, the oxidizing and reducing conditions were cycled as shown in Figure 27. Figure 27(a) shows the Au/Cu ratio for the two NP sizes at 442 eV kinetic energy during exposure to the conditions indicated. For the 4.8 nm NPs, the segregation trends are reversible when the sample is exposed to another round of oxidizing then reducing conditions. Although the oxidation state of Cu could not be fit and deconvoluted from the Cu 3p spectra measured in this study, the oxidation state of Au could be derived from the Au 4f spectra. Figure 27(b) shows the ratio of Au^{3+}/Au^{0} for the samples measured in the same conditions. Interestingly, the smaller NPs show only metallic Au under the different conditions, while the 4.8 nm NPs show significant oxidation of Au after exposure to oxidizing conditions. This result may have to do with the larger NPs storing Au oxides within the

bulk of the sample which are protected from reduction by a layer of metallic Au at the very surface. It should be kept in mind that the synchrotron X-ray irradiation may play an important role in the oxidation and reduction of the NPs in these experiments. Indeed, a previous study has shown that AP-XPS measurements in O_2 at room temperature can oxidize Au NPs/TiO_2 and a Au foil, and the synchrotron radiation in UHV could reduce the Au NPs, but not the Au foil.[270]

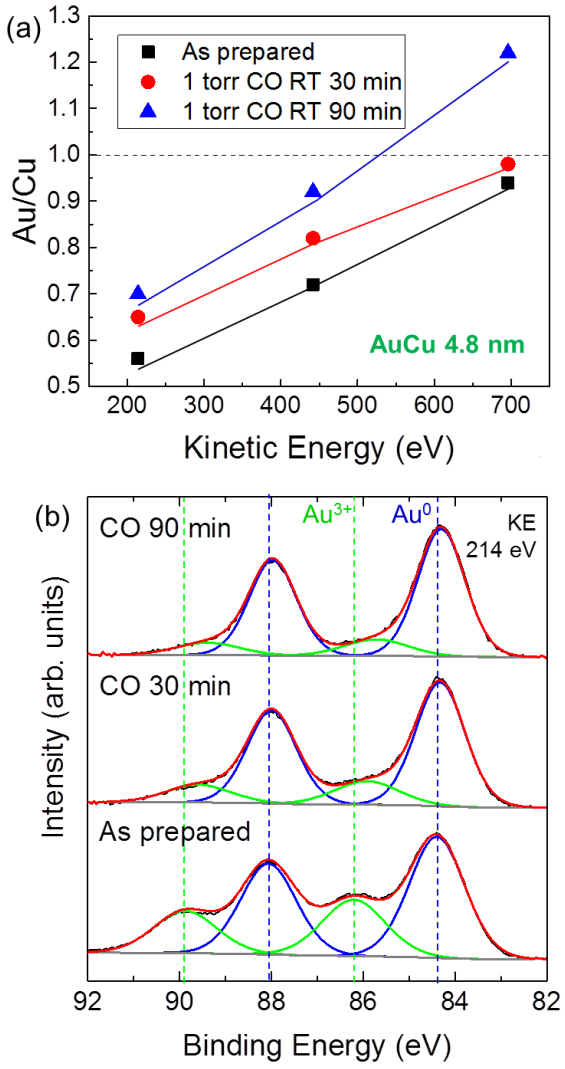

Figure 28. (a) Ratio of Au to Cu for 4.8 nm AuCu NPs under 1 Torr of CO at room temperature over time. (b) Au 4f region of 4.8 nm AuCu NPs in 1 Torr CO at room temperature over time. Data were measured with 214 eV photoelectron kinetic energy.

The dynamic changes in the largest NPs were also investigated in 1 Torr of CO at room temperature over time. Figure 28(a) shows the Au/Cu ratio of the as prepared sample, and the sample after 30 and 90 minutes in the CO environment. Remarkably, over time the Au/Cu ratio increases slightly, indicating segregation of Au to the surface and dynamic changes in the AuCu NPs even at room temperature. This Au surface segregation agrees with earlier results in reducing H_2 conditions. Figure 28(b) shows the Au 4f region at the most surface sensitive kinetic energy measured at the different times of CO exposure. Here it is clear that surface Au oxides are more reduced after 90 minutes in 1 Torr of CO. It should be kept in mind that the reduction of the Au^{3+} may also be accelerated by the X-ray irradiation, however no time dependent changes were observed in the Au 4f region when measured in UHV. These results indicate that Au^{3+} is unstable in CO, and the reduction of Au atoms may drive the segregation of Au to the surface.

Reactivity for CO_2 Electroreduction

The AuCu NPs supported on glassy carbon were used as the working electrode for the electroreduction of CO_2 in 0.1 M $KHCO_3$. Figure 29 shows the current density after the first 10 min of reaction for each sample as a function of NP size. A significant increase in activity with decreasing NP size was observed, with the smallest 1.4 nm NPs showing approximately twice the current density of the largest NPs. This trend is in agreement with previous studies on monometallic Au and Cu NPs, where CO_2 reduction current density increased significantly with decreasing NP size, particularly below 5 nm NP size.[2,3] In those studies, the size dependent trend was due to the increased population of low coordinated sites on the smaller NPs, which were more active. It is likely that a similar mechanism can explain the size-dependent activity here. The 5.6 nm NPs are slightly out of the trend, showing a larger current density than the 4.8 nm

NPs which are closest in size. This anomaly may be related to the differing composition of these two samples, which will be discussed below.

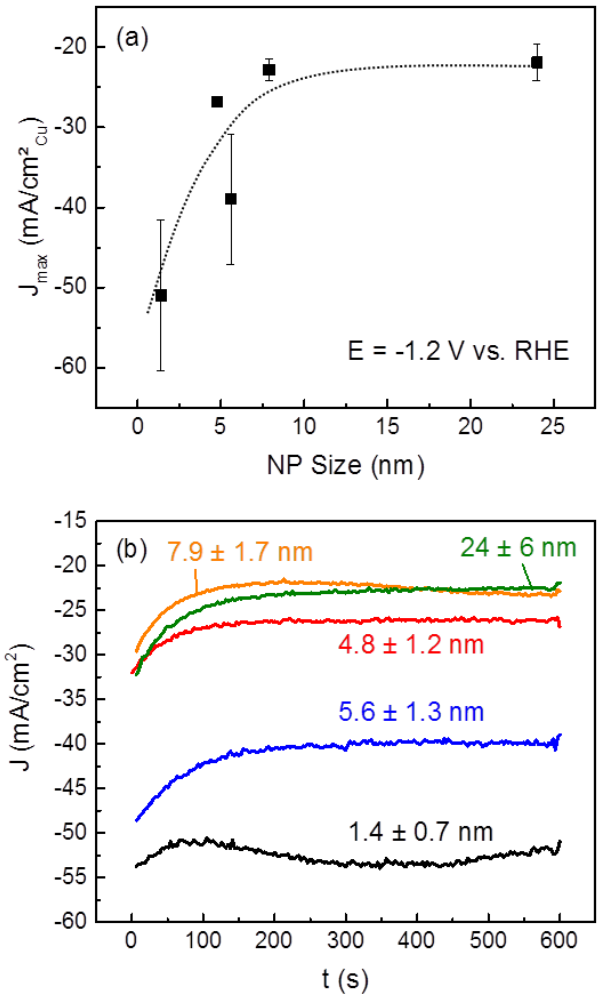

Figure 29. (a) Current density (*J*) after 10 min of reaction during CO_2 electroreduction at E = −1.2 V vs. RHE. Error bars indicate the standard deviation of multiple measurements on analogously prepared fresh independent samples. The dashed line is a guide for the eye. (b) Chronoamperometry during the first 10 min of reaction at −1.2 V vs. RHE.

The selectivity towards gas products was measured at −1.2 V vs. RHE using gas chromatography and is plotted in Figure 30. The NPs show ~20% selectivity for CO_2 reduction products (CO and methane), and the remaining selectivity is to H_2. Figure 30a shows that the production of H_2, CO, and CH_4 increases for smaller NPs, however Figure 30b shows that there is only very small size dependent change in the Faradaic selectivity for different products. CO selectivity increases from approximately 11% on the smallest NPs to 18% on the largest NPs, while CH_4 selectivity remains roughly constant with size. These trends are in stark contrast to monometallic Au and Cu NPs, which show drastic size-dependent changes in product selectivity.[2,3,176,271]

Our results demonstrate that while activity is strongly dependent on NP size, selectivity does not show a strong size-dependence. This result can be compared to size-dependent studies from our group on similarly prepared mono-metallic Au and Cu NPs during CO_2 electroreduction, which clearly show size dependent selectivity.[2,3] Cu NPs were shown to have increasing selectivity towards hydrocarbons for larger NP sizes, while smaller NPs favorably produced H_2 and CO. In comparison, for Au NPs, CO selectivity increased with increasing NP size, while H_2 selectivity decreased. The trends in H_2 and CO selectivity in our AuCu catalysts follow the trends we observed for pure Au NPs, although CO selectivity is not as high for the bimetallic NPs in comparison to the pure Au. This trend may indicate that the surface of the AuCu NPs is Au rich. In our previous work on micellar Au NPs, DFT calculations showed under the high H* coverage that is likely present on the NP surface under CO_2 electroreduction conditions, H_2 evolution becomes more facile than CO_2 reduction on low coordinated surfaces, i.e. Au(211) versus Au(111).[3] A similar mechanism may explain the higher H_2 selectivity of our

smallest AuCu NPs, since low-coordinated Au atoms on an Au-rich surface of AuCu NPs may also favor H_2 evolution. DFT has also predicted that adsorbed CO will enhance the hydrogen evolution reaction on close-packed metal surfaces due to repulsion between CO* and H*.[177]

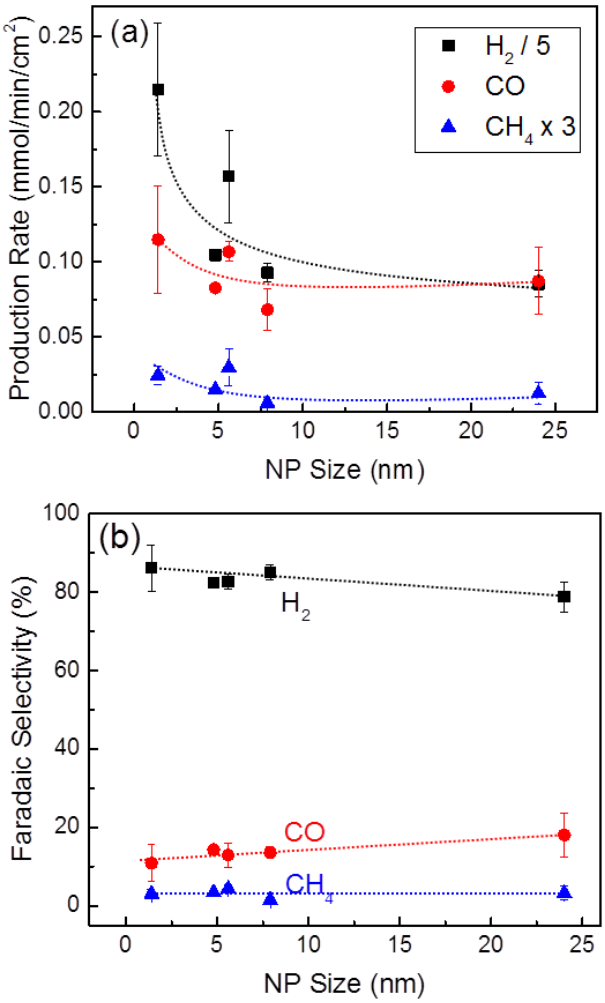

Figure 30. (a) Molar production rate and (b) Faradaic selectivity towards gas products formed during CO_2 electroreduction as a function of NP size. Error bars indicate the standard deviation of multiple measurements carried out on analogously prepared independent fresh samples. Dashed lines are guides for the eye.

In order to understand the size-dependent selectivity, it is critical to also consider the drastic chemical and structural changes that may occur in these bimetallic NPs under reaction conditions.[242,257,272-275] In particular, several studies have shown that such drastic restructuring can occur in bimetallic catalysts under CO_2 electroreduction conditions.[191,255,260,276] In their initial state, the AuCu NPs are oxidized due to the O_2 plasma treatment, and it is favorable for Cu to segregate to the surface under oxidizing conditions, due to its higher affinity for oxygen. Consequently, it is possible that the initial NPs have a Cu oxide-rich surface. Other studies of AuCu catalysts have also shown that Cu can segregate to the surface after air exposure, after calcination, or during oxidation reactions.[277-280] During the reaction at the high overpotential used for CO_2 electroreduction, the NPs are expected to become at least partially reduced, and under these reducing conditions it is more favorable for Au to segregate to the surface, due to its lower surface energy and larger atomic radius. Indeed, Friebel et al. have shown that Cu monolayers on Au(111) undergo restructuring and alloying with the underlying Au due to segregation of Au atoms to the surface under electrochemically reducing conditions.[260] Furthermore, EXAFS measurements of AuCu clusters in a reducing H_2 environment have also indicated segregation of Au to the surface.[281] Similarly, it is possible that the surface of our AuCu NPs is Au-rich under reaction conditions, which could explain the higher selectivity towards CO as opposed to CH_4 and the absence of C_2H_4. Our AP-XPS measurements of micellar AuCu NPs described above support the idea that significant restructuring may occur in the NPs under reactive environments, with Cu segregation to the surface under oxidizing conditions, and Au segregation to the surface under reducing conditions.

Studies of composition dependence in bulk and 10 nm NP AuCu catalysts have shown that increasing Au content increases the selectivity towards CO compared to hydrocarbons.[187,259] Similarly, for our AuCu NPs, which may be Au-rich at the surface, the majority of the CO_2 reduction selectivity is towards CO, while only ~3% CH_4 selectivity is observed. The 5.6 nm NPs were observed to have slightly higher methane selectivity and lower CO selectivity compared to 4.8 nm NPs, which are very similar in size, which may be due to their bulk composition being Cu rich. This Cu-rich sample also shows the highest methane production, in line with the results from Kim et al., who show that no methane is produced on their $Au_{50}Cu_{50}$ catalysts, whereas 4% methane is produced on $Au_{25}Cu_{75}$ at ~−1.1 V vs. RHE. Furthermore, their Cu rich catalyst showed lower CO selectivity in comparison to a sample with the same size but 50-50 Au-Cu composition.[259]

Another factor to consider is the reduction of the oxidized NP surfaces, which may create unique highly active sites for CO_2 electroreduction. Previous work has shown that bulk Cu surfaces which are oxidized and reduced show higher activity, lower overpotentials, and higher selectivity towards CO or C_2H_4 with suppression of CH_4 in comparison to metallic Cu.[184,282-286] Similarly, oxidized and reduced Au surfaces have shown vastly improved CO_2 reduction behavior compared to metallic Au.[170] Our group has recently shown that the improved catalytic reactivity of oxide-derived Cu is not only due to the highly rough surfaces which are created during the oxidation and reduction treatment or the high local pH generated by the high currents on these rough surfaces, but also by the survival of cationic Cu species and subsurface oxygen within the catalyst which control the selectivity and low overpotential for CO_2 reduction.[286] The AuCu NPs used in this study are heavily oxidized in their initial state, and would become

partially or fully reduced under reaction conditions. However, it is unlikely that oxide species can survive in these small NPs at CO_2 electroreduction overpotentials, in contrast to the thick bulk oxidized surfaces. In addition, we do not see C_2H_4 production or high CO selectivity, which are the signatures of oxide-derived catalysts. In this case, a plausible explanation for the trends observed is that, even if Cu^+ species might be more stable on the Cu-Au NPs than in other related systems such as Cu-Pd or Cu-Ni due to the low affinity of Au for O,[287] the concomitant favorable Au surface segregation results in the absence of Cu+ at the NP surface. Therefore, even if Cu^+ species might remain stabilized on these NPs under reaction conditions, they should be subsurface and therefore not directly exposed to the reactants.

Conclusion

Bimetallic AuCu NPs 1.4–24 nm in size were synthesized using inverse micelle encapsulation to achieve narrow size distribution. X-ray spectroscopy revealed that the NPs were oxidized in their initial state. 1.4 and 4.8 nm NPs were measured using AP-XPS under oxidizing and reducing conditions in order to resolve changes in the surface composition due to reaction environment. By cycling in O_2 or H_2 environments at elevated temperature, reversible segregation of Cu to the surface was observed under oxidizing conditions, while Au segregation occurred under reduction conditions. Additionally, under CO atmosphere at room temperature, segregation of Au to the surface over time, along with reduction of surface Au oxides was observed. When used as catalysts for CO_2 electroreduction, smaller NPs showed high current density during CO_2 electroreduction due to their higher population of low coordinated sites at the surface. Faradaic selectivity depended less strongly on NP size. For all NPs, H_2 was the dominant product with approximately 80% selectivity, although CO and CH_4 were also formed.

CO production increased and H_2 production decreased by ~7% with increasing NP size. The selectivity trends observed are assigned to possible preferential segregation of Au to the NP surface under reducing reaction conditions, which may be responsible for the low selectivity for hydrocarbon products. In order to further tune the catalytic properties of AuCu NPs, additional studies of the morphological and compositional changes which occur in the NPs under reaction conditions must be performed.

CHAPTER SEVEN: TUNING THE REACTIVITY OF COPPER CATALYSTS FOR CO_2 ELECTROREDUCTION THROUGH OXIDATION STATE

Introduction

Investigations in recent years have led to the development of many interesting metal-based catalytic materials for CO_2RR. Nanostructured catalysts such as NPs,[2,3,185,288-290] nanocubes,[291,292] nanofoams[293] and nanowires[172] have shown vastly improved activity or selectivity over bulk materials.[1,247] Recently, nanostructures derived from the reduction of copper oxides have shown vastly improved CO_2 reduction efficiency at lower overpotentials.[184,283-285] These materials were synthesized from the reduction of thermally oxidized Cu or electrodeposited Cu_2O, and in general display improved current density, enhanced CO_2 reduction to CO at low overpotentials, and a partial suppression of methane in favor of ethylene at higher overpotentials. Despite these promising results, the mechanism behind the reactivity trends of oxide-derived CO_2RR catalysts is still under dispute. Grain boundaries in oxide-derived Cu have been suggested to support unique surface sites which may be active for CO_2RR.[184,282,294] Another mechanism could be the increase in local pH due to high current densities[233] on the highly roughened surfaces, which could alter the reaction pathway in favor of ethylene.[295-297] Alternatively, the nanostructuring of the catalyst surface during the oxide reduction may also provide low-coordinated atoms as active sites.[2] $Cu^{\delta+}$ sites which may remain on the catalyst surface during the reaction have also been suggested to be the active sites.[298-302] However, no *operando* evidence of this claim exists up to this point, and only ex situ evidence has been

Adapted from Mistry, H.; Varela, A. S.; Bonifacio, C. S.; Zegkinoglou, I.; Sinev, I.; Choi, Y.; Kisslinger, K.; Stach, E. A.; Yang, J. C.; Strasser, P.; Roldan Cuenya, B. *Nat. Commun.* **2016**, *7*, 12123.

presented. This ex situ evidence is complicated by the rapid formation of native oxides on metallic Cu surfaces upon removal from the reactor and exposure to air.[285] In general, it has been assumed that Cu oxides are completely reduced during the relatively high CO_2RR potentials used (that is, ~ 1 V versus reversible hydrogen electrode (RHE)), and that the reaction occurs only on metallic Cu species.

Oxygen plasma treatment is a facile and scalable technique to controllably oxidize and nanostructure metal catalysts for CO_2RR that has not yet been explored. Plasma treatment is a powerful method to activate catalysts, for example by removing capping ligands used in the synthesis of nanoparticles without sintering,[96,303] by rapidly changing the chemical state of the surface at room temperature,[175,304] or by creating defects or embedded atoms which can improve reactivity.[305] We have used oxygen and hydrogen plasmas to create novel nanostructured oxide layers and porous surfaces with tunable morphology and chemical state on polycrystalline Cu. These catalysts can lower the onset potential of CO_2 reduction to ethylene by 350 mV compared with electropolished Cu, with a maximum faradaic selectivity of >60% at −0.9 V versus RHE. Here, using a combination of characterization techniques—including *operando* X-ray absorption fine-structure spectroscopy (XAFS), scanning transmission electron microscopy (STEM) equipped with energy dispersive X-ray spectroscopy (EDS)—we gain insight into the catalysts in their working state and find that Cu^+ is the active species for reducing CO_2 to ethylene. Through our results, we unravel the mechanism behind the improved activity and unique ethylene selectivity of oxide-derived Cu catalysts and lay out the design principles necessary for improved ethylene-selective CO_2RR catalysts.

Experimental Methods

All Cu foils were initially electropolished in 85% phosphoric acid at 3 V versus a titanium foil, then thoroughly rinsed with ultra-pure water and dried with nitrogen. Plasma treatments were performed in 400 mTorr of H_2 or O_2 for the indicated plasma power and time. For the O_2 100 W 2 min + H_2-treated sample, 100 W 10 min of H_2 plasma was used.

SEM images were obtained using a Quanta 200 FEG microscope from FEI with a field emitter as electron source. A secondary electron (Everhart-Thornley) detector was used for the image acquisition. An electron acceleration voltage of 10 kV and a working distance of 10 mm were chosen for the measurements. TEM cross-section samples were prepared using a FEI Helios 600 Dual Beam Focused Ion Beam (FIB) at the Center for Functional Nanomaterials (CFN) at Brookhaven National Laboratory (BNL) by Eric Stach's group. The FIB sectioning was performed at 30 keV with final milling at 5 keV. Spatially resolved elemental maps were acquired using a FEI Titan TEM/STEM microscope with ChemiSTEM technology (X-FEG and SuperX with four windowless silicon drift EDS detectors) operated at 200 kV, at the National Center for Electron Microscopy (NCEM), Molecular Foundry at Lawrence Berkeley National Laboratory (LBL). A Hitachi 9500 TEM at the Nanoscale Fabrication and Characterization Facility (NFCF), University of Pittsburgh operated at 200 keV was used to acquire HRTEM images and SAED patterns. TEM measurements were performed by Prof. Judith Yang's group.

XANES and EXAFS spectra were measured at beamline 2–2 of the Stanford Synchrotron Light Source. A home-built *operando* electrochemical cell was used, with a platinum foil counter electrode and silver/silver chloride (Ag/AgCl) reference electrode. The samples were mounted behind an X-ray kapton window with 1 mm of electrolyte between the sample and window. The

electrolyte (0.1 M $KHCO_3$) was circulated between the cell and a reservoir in which CO_2 was continuously bubbled. Measurements were performed in fluorescence at small incidence angle using a passivated implanted planar silicon (PIPS) detector. The acquisition of each spectrum took 15 min, and they were acquired during the first 15 min and after 1 h of reaction. Data analysis was performed using the Athena and Artemis software. The FEFF8 code was used to simulate Cu, Cu_2O and CuO spectra for EXAFS fitting.

Electrochemical measurements were carried out by Prof. Peter Strasser's group (Technical University Berlin, Germany) in a custom made two compartment cell separated by a Nafion membrane. The glassware was cleaned in a 'nochromix' bath and afterwards in concentrated HNO_3 for 1 h, rinsed, and sonicated with ultra-pure water several times. The working compartment was filled with 120 ml 0.1 M $KHCO_3$ (Sigma-Aldrich 99.95%). Before and during the electrochemical reaction the cell was purged continuously with CO_2 (30 ml min^{-1}), reaching a stable pH value of 6.8.

A platinum mesh 100 (Sigma-Aldrich 99.9%) was used as counter electrode and a leak-free Ag/AgCl electrode as reference electrode (Hugo Sachs Elektronik Harvard apparatus GmbH). The plasma-treated Cu foils were used as working electrode and contacted by a gold clamp. Every measurement was started with a linear voltammetric sweep, performed with a scan rate of $5mVs^{-1}$ between E = + 0.05 V vs. RHE and the working potential (between 0.45 V and 1.0 V vs. RHE) followed by a chronoamperometric step for 60 min. All reported potentials are corrected for Ohmic drop determined by electrochemical impedance spectroscopy.

After 10 and 60 min of bulk electrolysis at constant potential, a sample of the gas was analyzed by gas chromatography (Shimadzu GC 2016) to determine the production rate and

faradaic selectivity of the gaseous products. In addition, an aliquot of the electrolyte was analyzed by a high-performance liquid chromatograph (Agilent 1200 series).

Results

To synthesize plasma-activated Cu, electropolished polycrystalline Cu foils were treated in O_2 and H_2 plasmas of varying power and duration. Figure 31 presents scanning electron microscopy (SEM) images of the Cu films treated with O_2 plasma at 20 W for 2 min (top row) and 100 W for 2 min (middle row) and 10 min (bottom row). By tuning the plasma conditions, the morphology of the surface and oxide thickness can be easily controlled. Growth of the Cu oxide begins at grain boundaries, forming micron-sized wires as shown in Figure 31a. With increasing plasma time and power, the wires merged, forming a highly roughened surface, (c.f. Figure 31b,e,i) and became highly porous with an observed 64% increase in the number of pores and 50% decrease in pore size. Subsequently, the plasma-activated Cu samples were partially reduced *in situ* during CO_2RR, and the resulting surface morphology is shown in the last column of Figure 31. For most samples, an increase in the porosity was observed. Interestingly, the sample oxidized at 100 W for 10 min showed the growth of hair-like nanoneedles after the reaction. To compare the effect of plasma reduction on the film morphology to the electrochemical reduction mentioned above, a H_2 plasma was used (100 W for 10 min) and is shown in Figure 31g. The resulting structure was very similar to the electrochemically reduced sample (c.f. Figure 31f), indicating that plasma reduction or electrochemical reduction of the Cu oxides results in a similar structure.

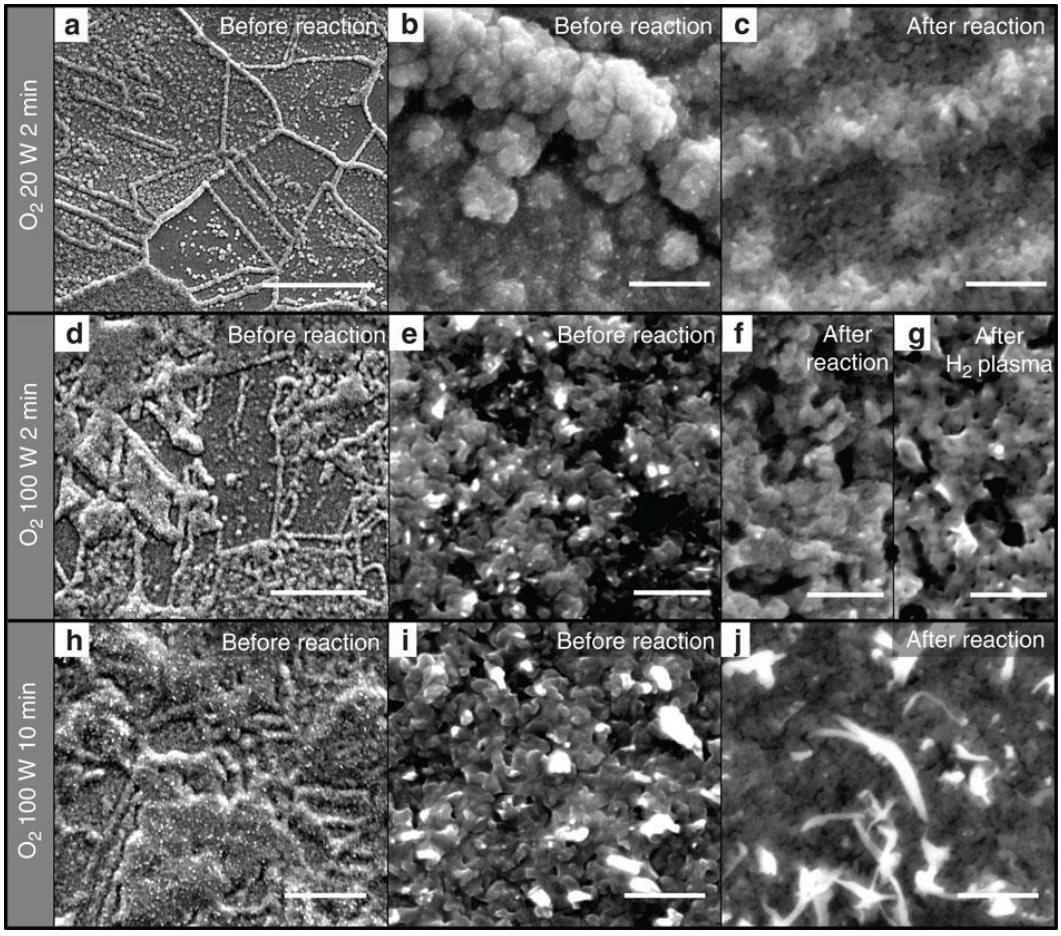

Figure 31. Morphological characterization of plasma-treated Cu foil electrodes. SEM images of Cu foils treated with O_2 plasma for (a–c) 20 W 2 min; (d–g) 100 W 2 min; and (h–j) 100 W 10 min. (a,b,d,e,h,i) The morphology of the as-prepared foils. (c,f,j) The morphology after the CO_2RR reaction. (g) The sample plasma treated with O_2 at 100 W for 2 min after an additional H_2 plasma treatment at 100 W for 10 min. Scale bars, (a) 10 μm; (b,c,e–g,i,j) 500 nm; (d,h) 20 μm.

To gain further information on the structure and chemical state of the plasma-treated Cu films, cross-sections of the samples were measured using STEM combined with elemental mapping using EDS. Cross-sectional EDS maps of plasma-treated Cu samples before and after CO_2RR are shown in Figure 32. After the O_2 plasma treatment, the EDS maps show two well-

defined oxide layers over the bulk metallic Cu film. Stoichiometric analysis using EDS data resulted in Cu:O ratios of 2.7:1.0 and 1.3:1.0 for the interlayer and upper layers, respectively, indicating that the interlayer is Cu_2O, while the upper layer is CuO. It is also apparent that at grain boundaries and crystallographic domains with the fastest oxide growth, a thick 1.5-μm Cu_2O interlayer grows with a thinner 100 nm CuO top layer, while in domains with slower oxide growth, the CuO layer is thicker at 260 nm—as clearly shown in Figure 32a. Figure 32g shows the 100 W 2 min oxidized Cu with a subsequent H_2 plasma treatment. A 100 nm layer at the surface is reduced entirely to metallic Cu, with the CuO and Cu_2O oxide layers being still observed subsurface. After H_2 plasma treatment, the sample was exposed to air for more than a week before TEM sample preparation and analysis, and the native Cu oxide layer, measured to be <3 nm thick, was insignificant compared with the thick oxide layers which formed from the plasma treatment and the remained during the reaction. This indicates that observed oxides in our samples before or after reaction are not simply due to surface oxidation in air during the ex situ sample transfer to the TEM. Figure 32c,f,h also shows EDS maps of these samples after 1 h of CO_2RR at −0.91 V versus RHE. Remarkably, after the reaction a single layer with O atom concentration ranging from 3 to 29 atomic % remains with porous and oxygen-rich regions observed. The Cu oxide species are present throughout the layer, indicating that the surface is rich in Cu^+ sites which remain stable on the surface and near surface layers during the reaction. This finding challenges the conventional assumption that only metallic Cu (Cu^0) is the active species during CO_2RR and indicates that Cu^+ plays a significant role in the unique reactivity of oxide-derived Cu.

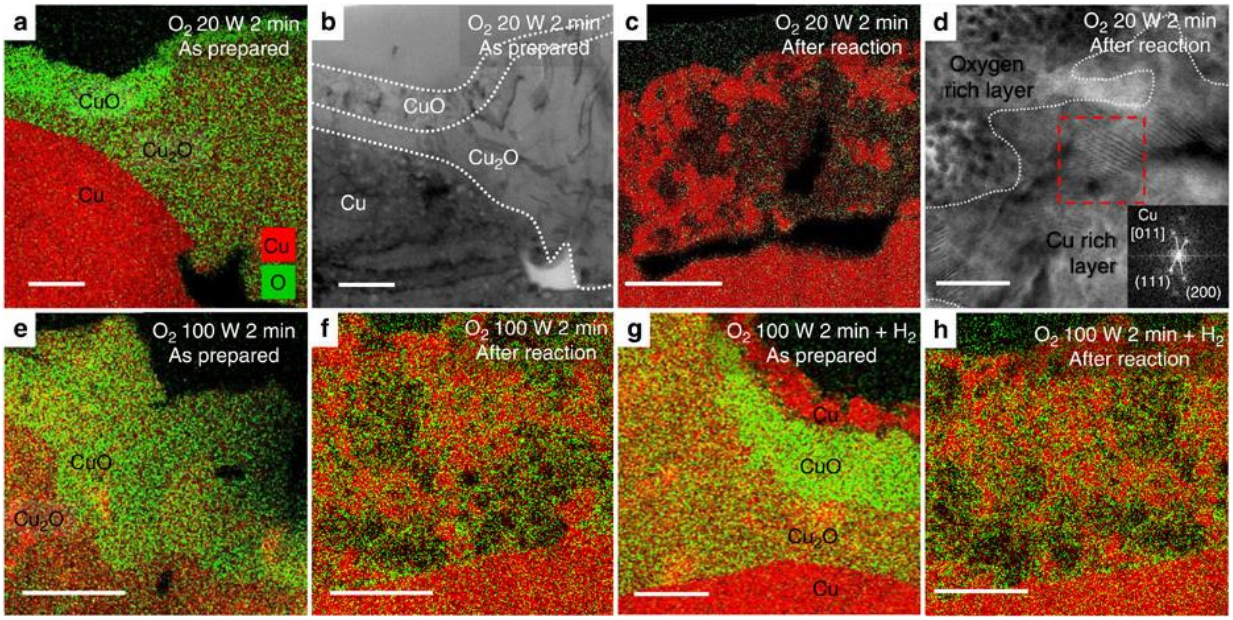

Figure 32. Morphological and chemical analysis of plasma-activated Cu foils. EDS elemental maps of Cu foils treated with O_2 plasma for (a–d) 20 W 2 min; (e–f) 100 W 2 min; and (g–h) 100 W 2 min+H_2 plasma. The images labelled 'after reaction' were used as catalyst for CO_2RR for 1 h at −0.91 V versus RHE. (b,d) HRTEM and SAED analysis of the O_2 plasma 20 W 2 min treated sample before and after the reaction, respectively. Scale bars, (a–c) 300 nm; (d) 20 nm; (e–h) 200 nm.

Figure 32b,d show high-resolution TEM (HRTEM) and selected area electron diffraction (SAED) patterns of the O_2 20 W 2 min plasma-treated sample before and after the reaction. The diffraction analysis confirms that a CuO top layer and Cu_2O interlayer exist before the reaction (Figure 32b). After the reaction, the layer transforms into a mixture of Cu-rich regions, which contain only 3.4±0.9% oxygen atoms, and oxygen-rich regions with 19.5±2.6% oxygen atoms identified as Cu_2O. It is clear that the oxygen is depleted during the reaction, but the surface layer of the oxidized Cu films is still rich in oxygen even after 1 h of reaction. It is unlikely that the Cu oxides in the sample after reaction could be a result of air exposure, since the native oxide

would be much thinner due to its slow growth rate at room temperature in air and would contain Cu(II) species, which are not observed here.

To further investigate the changes in the structure of the oxide layer during CO_2RR and gain insight into the chemical state of the active Cu species, *operando* XANES and EXAFS were used. Figure 33 shows the Cu K-edge XANES and EXAFS spectra of the O_2 100 W 2 min plasma-treated Cu measured in fluorescence at small incidence angle (for enhanced surface sensitivity) during CO_2RR at −1.2 V versus RHE. Although the thickness of the sample caused dampening of the XAFS signals due to self-absorption, the XANES spectrum of the as-prepared plasma-oxidized Cu shows the features of Cu_2O, in particular, the prominent shoulder at the edge marked with a green dashed line at ~8,982 eV. The presence of metallic Cu and Cu oxide in the initial sample is also clear in the EXAFS data shown in Figure 33b,c. During the first 15 min of reaction, a combination of Cu and Cu_2O features are still present, and at 1 h, only metallic Cu features are discernable. Although an oxygen content of ~25–28% is still present in the surface layer of the catalyst after 1 h of reaction according to STEM-EDS, XAFS probes further into the bulk, and when the films are partially reduced, the XAFS signals become dominated by the signal of the metallic Cu underlayer. Nevertheless, we have shown here unquestionably that for our plasma-oxidized Cu catalyst, Cu_2O species are present and can participate in the reaction. It is clear that significant changes occur in the bulk of the Cu oxide layer during the first 15 min of reaction in which the initial CuO and Cu_2O layers are reconstructed and some of the oxygen is depleted. After this initial change, it is likely that the Cu_2O species remain relatively stable in the surface layer, since the activity and selectivity measured after 10 min and 1 h are unchanged for all the oxidized samples. Furthermore, the reactivity of the O_2 20 W 2 min sample was observed

to be stable over the course of 5 h, suggesting there is no significant change on the active phase during this time. Therefore, it is likely that Cu^{+} species can be supplied to the surface from the thick initial oxide surface and subsurface layers during the reaction to maintain the reactivity of these catalysts over time.

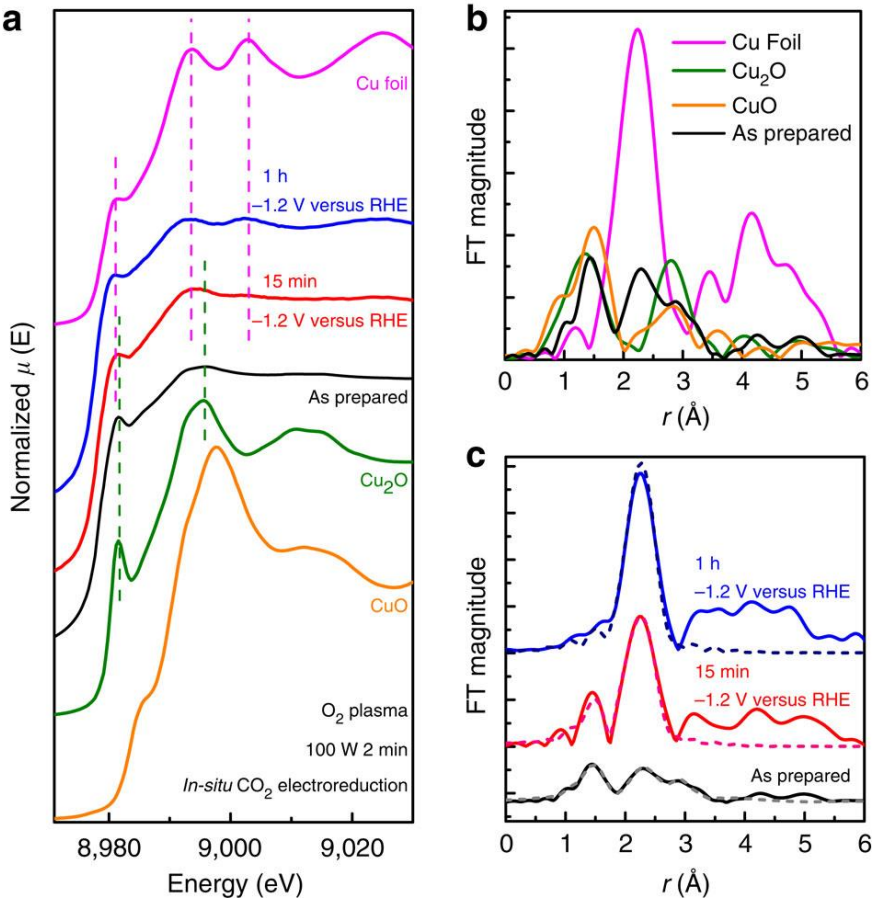

Figure 33. *Operando* structural and chemical characterization during CO_2 electroreduction. (a) XANES spectra of the O_2 100 W 2 min treated sample measured under *operando* conditions in 0.1 M $KHCO_3$ during the first 15 min and after 1 h of reaction at −1.2 V versus RHE. Bulk Cu, Cu_2O and CuO spectra are plotted as reference. (b) EXAFS spectrum of the as-prepared sample plotted with references. (c) EXAFS spectra and fits (dashed lines) of the sample measured under *operando* conditions. Fourier transforms are k^2-weighted.

The catalytic activity and selectivity of the plasma-activated copper foils were studied by performing bulk electrolysis in 0.1 M potassium bicarbonate ($KHCO_3$) at a constant potential and analyzing the reaction products via chromatographic techniques. Figure 34 shows the geometric current density as a function of applied potential. The plasma treatment has a clear effect on the activity of Cu towards CO_2RR which can partially be attributed to the surface roughness. In general, longer and higher power O_2 plasma treatment increases the roughness factor (Table 8), which is an estimate of the active surface area derived by measuring the double layer capacity and normalizing by the electropolished foil. However, roughness effects alone cannot explain all of our experimental findings satisfactorily. In fact, the initial oxidation state of the sample also affects the current density. This is particularly evident when we compare the catalytic activity of the O_2 100 W 2 min and O_2 100 W 2 min+H_2 plasma-treated Cu. Although both samples have a similar surface roughness, as shown in Table 8, their catalytic activity is significantly different. The H_2 plasma treatment on the oxidized sample reduces the activity by about two times compared with the oxidized sample without H_2 treatment. The H_2 plasma treatment depletes the oxide species available initially in the sample, as shown in Figure 32g, while having minimal effect on the surface roughness. This result is an indication that the Cu oxide species are critical for improved current density. As demonstrated by our STEM-EDS data, even after 1 h of CO_2RR, patches of Cu_2O are still observed near the sample surface.

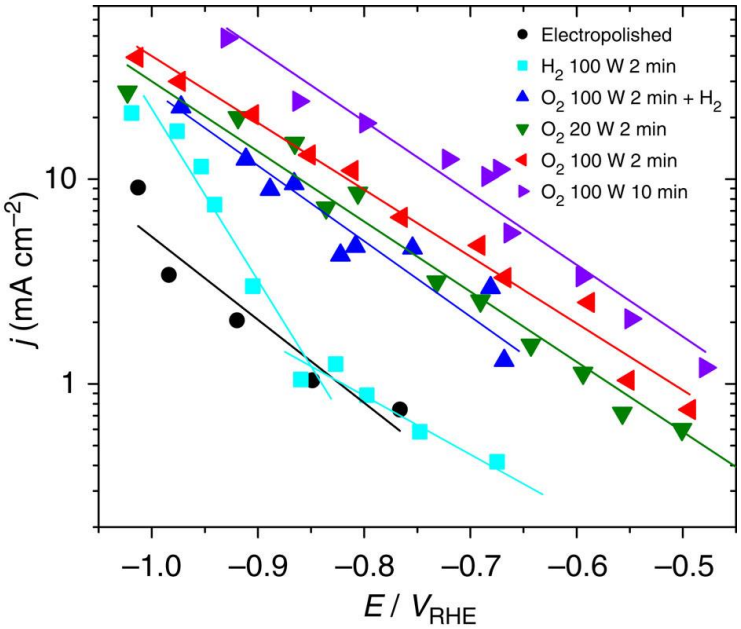

Figure 34. Electrochemical activity during CO_2 electroreduction. Geometric reduction current density as a function of applied potential.

Table 8. Roughness factors estimated through capacitance measurements.

Sample	Roughness Factor
Electropolished	1.0
H_2 100W 2 min	1.5
O_2 20W 2 min	26.4
O_2 100W 2 min	43.7
O_2 100W 2 min+H_2	48.3
O_2 100W 10 min	89.7

Figure 35 shows the faradaic selectivity of the CO_2RR products for the plasma-activated Cu samples as a function of applied potential. The plasma treatments not only affect the activity of copper, but more importantly, they also have a remarkable effect on selectivity. The

selectivity change is most drastic on the O_2 treated samples: on one hand, this treatment clearly suppresses methane formation (Figure 35c), while on the other hand, it enhances the formation of the other products of CO_2RR (CO, formate and ethylene). Consistent with results from Kanan and co-workers,[184] we observe that the onset potential towards CO and formate ($HCOO^-$) is shifted to lower overpotentials. Furthermore, for our plasma-oxidized Cu, the selectivity towards CO reaches a maximum of 60% at −0.5 V versus RHE, which is three times higher than for electropolished Cu foil. In our study, the onset of ethylene production is also shifted from approximately −0.85 V versus RHE for metallic Cu foils to as low as −0.5 V versus RHE for the most oxidized Cu foils. In addition, we observe a remarkably high selectivity towards ethylene, reaching 60% at −0.9 V versus RHE for the O_2 20 W 2 min plasma-treated sample. This value is higher than other oxide-derived Cu catalysts synthesized from thermal oxidation,[184] which show <10% ethylene efficiency at these potentials, or from electrodepositon of Cu_2O.[283-285] In addition, the most oxidized foils in this study also produce trace amounts of ethanol. Interestingly, the 100 W O_2 plasma-treated samples, which have been exposed to a stronger oxygen plasma treatment and are characterized by the highest roughness factors, also produce trace amounts of ethane, but nonetheless exhibit lower C_2H_4 selectivities. These results indicate that there is an optimal oxidation treatment to favor ethylene formation, in agreement with results from Ren et al.[284] We hypothesize that this trend could be related to mass diffusion limiting ethylene formation on the most roughened surfaces where high geometric currents are achieved. This is also consistent with our observation that at high overpotentials—at which high geometric current densities are also achieved—ethylene selectivity is suppressed.

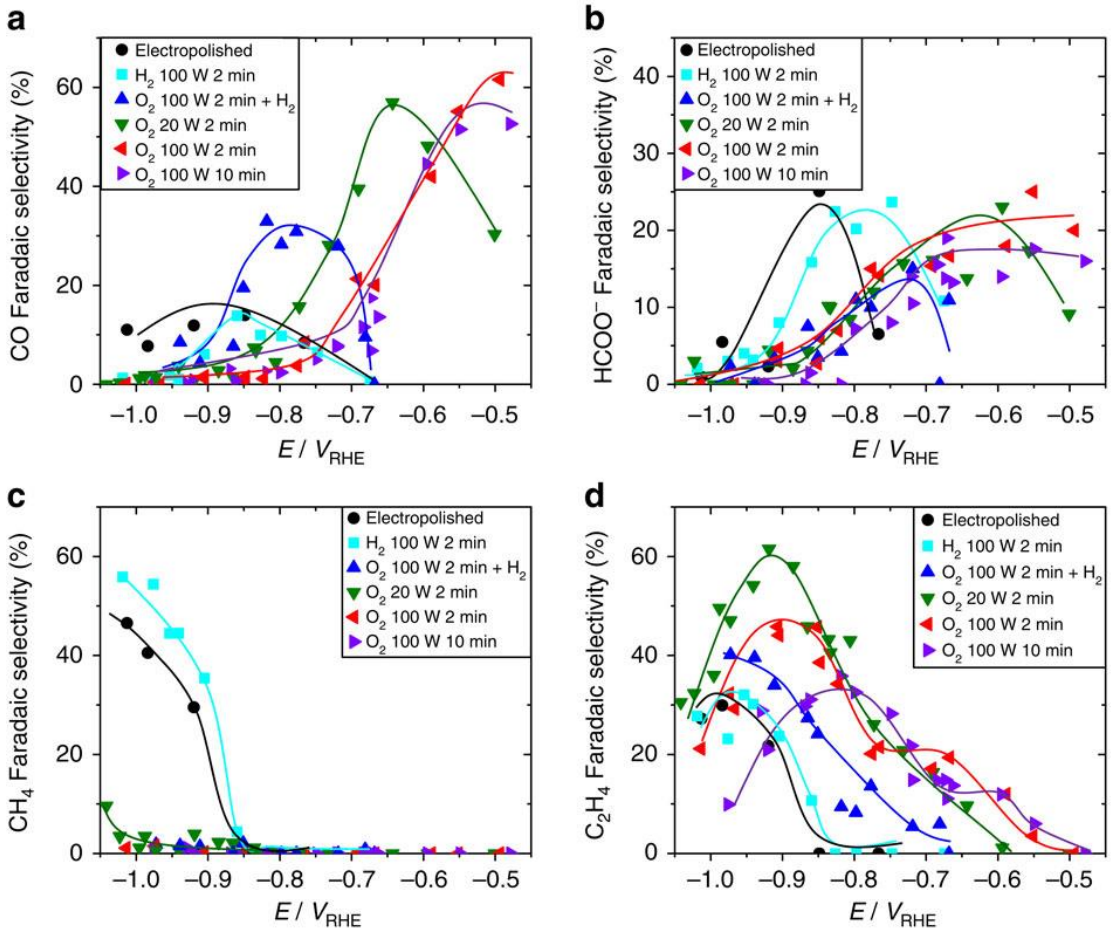

Figure 35. Faradaic selectivities of the main CO_2RR products. Data were acquired after 60 min of CO_2 electrolysis at a constant potential in CO_2 saturated 0.1 M $KHCO_3$. (a) CO, (b) formate, (c) CH_4 (d) C_2H_4. Solid lines are guides for the eye. The remaining selectivity is due to H_2.

To confirm that the selectivity trend for the oxidized samples is due to the oxidation state, not the surface roughness, we can compare the O_2 100 W 2 min treated sample with the same sample which was exposed to an identical O_2 plasma treatment plus H_2 plasma. Despite their similar roughness (Table 8), their selectivity is drastically different. On both samples, methane formation is suppressed, however on the former sample, which was only treated with O_2 plasma,

the onset potential for the formation of CO, $HCOO^-$ and C_2H_4 is clearly shifted to less negative potentials. The main difference between these two samples is the availability of Cu^+ sites in their initial state. Thus, by depleting the Cu^+ sites using the H_2 plasma, we have reduced the number of active sites available for C_2H_4 formation, and therefore altered the selectivity.

We also observed that the H_2 100 W 2 min plasma-treated sample, which has a similar roughness to the electropolished Cu foil, has an improved catalytic performance towards CO_2RR compared with the polished foil. The H_2 plasma-treated sample exhibits an earlier onset potential for formate production and a higher faradaic selectivity towards methane. An explanation for this effect could be improved CO_2 reduction on defect sites generated by the plasma treatment. Another possible mechanism could be cleaning of contaminants or the native oxide from the Cu surface by the H_2 plasma, which may improve the CO_2RR performance in comparison to the electropolished sample. XPS shows that the small adventitious carbon 1s peak present on the electropolished foil is diminished after the H_2 plasma treatment, although the oxidation state of the surface of the foil is not changed.

Discussion

Figure 36 shows a summary of the hydrocarbon selectivity as a function of the plasma treatment of the Cu foils. Two competing effects are controlling the reactivity of the plasma-treated Cu foils: the surface roughness and the oxidation state of the surface layer. As described above, after oxidizing the surface layer with O_2 plasma, we see an almost complete suppression of methane formation. As the foils are more oxidized, the surface roughness increases, and there is a drop in the ethylene selectivity, likely due to mass diffusion limitations.

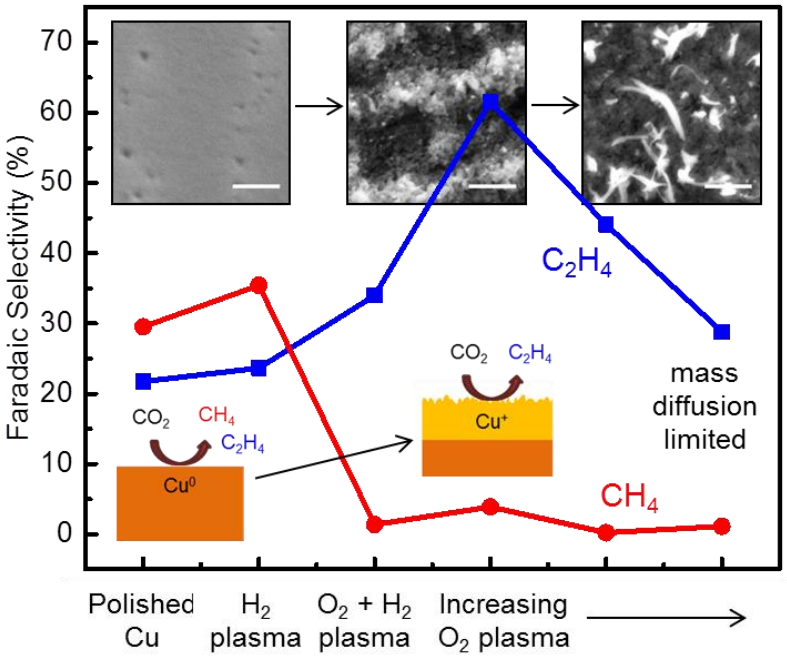

Figure 36. Summary of hydrocarbon selectivity of plasma-treated Cu foils. From left to right, the insets show SEM images of the low surface area H_2 plasma-treated metallic Cu foil, the O_2 20 W 2 min plasma-treated Cu foil with optimal ethylene selectivity, and the high surface area nanoneedles on the O_2 100 W 10 min oxidized sample after the reaction (500 nm scale bars).

Previous studies have proposed that the catalytic behavior of such oxygen-derived Cu catalysts can be attributed to a roughness effect or to the presence of strongly binding defect sites such as grain boundaries. Recent work in Verdaguer-Casadevall et al.[282] have shown that CO-binding energy on oxide-derived Cu is higher than on metallic copper. This high-binding energy could explain the early onset potential for CO_2RR, but does not explain why subsequent H_2 plasma treatment would suppress the ethylene selectivity of the 100 W 2 min oxidized sample in our study.

Another proposed mechanism for the behavior of oxide-derived CO_2RR catalysts is a pH effect. It is expected that during the catalytic reaction on these rough surfaces there is a significant rise in the local pH, suppressing the pH-dependent CO protonation that leads to methane formation.[186,244] The pH-independent pathway via CO dimerization, however, is not affected, resulting in high ethylene selectivities.[295,306,307] Consistently, all samples with some initial oxidation treatment (rough surfaces) exhibit suppression of methane, as shown in Figure 36, which may be attributed to the pH effect. However, the lower onset potential for ethylene production observed in the oxygen-treated samples (Figure 35d) cannot be attributed to a local pH effect. In fact we observed that that the increasing oxidation treatment leads to a decrease in the overpotential for C_2H_4 production, indicating that high activity for ethylene can be related to the oxidation–reduction treatment and not to a local pH effect.

By comparing the catalytic performance of O_2 plasma 100 W 2 min+H_2 and O_2 plasma 100 W 2 min Cu, we have demonstrated that purely a roughness effect cannot explain the reactivity trends of our plasma-activated oxide-derived Cu catalysts, since these catalysts with nearly the same roughness, but different oxide content have significantly different reactivity and selectivity. In addition, while the high local pH could explain the suppression of CH_4, it cannot explain the earlier onset potential for CO_2RR. Since surface roughness and pH effects cannot fully explain the reactivity of our plasma-activated Cu, it is clear that another mechanism is also involved in controlling the reactivity. Based on our STEM-EDS and *operando* XAFS measurement we conclude that, contrary to common belief, Cu^+ species are stable under reaction conditions and play a determining role in the reactivity of oxide-derived Cu. These species may

interact with negatively charged CO_2 reduction intermediates which may play an important role in determining selectivity.[244]

The mechanism behind the stability of Cu^+ species under the thermodynamically unfavorable conditions of CO_2RR is still under investigation; however, several mechanisms may explain this phenomenon. One possibility is that the highly roughened surfaces with low-coordinated sites which are formed after O_2 plasma treatment may bind more strongly to oxygen, helping to stabilize oxides during the reaction. Strain in the surface caused by the oxidation and reduction of the surface may also cause strong oxygen binding. The highly porous nature of the films formed might also serve as favorable oxygen reservoir. Another possibility is that the high local pH could help to stabilize Cu^+ by negatively shifting the overpotential for Cu_2O reduction. Recent studies of nanostructured tin oxide catalysts for CO_2 electroreduction have also suggested that oxide species are stable during the reaction and play a controlling role in their selectivity. Sn oxides and not metallic Sn were shown to be the active species for CO_2 reduction to formic acid and are metastable during the reaction at reducing potentials, even though the oxides are thermodynamically unstable under these conditions.[243,308,309] While similar stability of Cu^+ has been suggested for oxide-derived Cu catalysts[285,298,310], we provide here the first direct evidence that Cu^+ species are stable during CO_2RR and are key for controlling selectivity.

Conclusion

In summary, we have synthesized superior oxygen-derived Cu catalysts using plasma treatments and used a synergistic combination of advanced ex situ, *in situ* and *operando* techniques to reveal the key mechanisms behind the improved performance of oxide-derived copper catalysts. Plasma treatment was found to be a facile method to rapidly oxidize Cu foils,

which resulted in stable oxide layers with a unique surface structure. These plasma-oxidized catalysts achieve lower onset potentials for CO, formate and ethylene, as well as outstanding ethylene selectivity of 60% at −0.9 V versus RHE. In addition, using STEM-EDS and *operando* XAFS, we have found that the oxides in the surface layer are surprisingly stable against reduction, with a significant amount of oxide species and dissolved oxygen remaining after 1 h of reaction at relatively high potentials (−0.91 V versus RHE). Furthermore, ethylene synthesis and methane suppression are due to the presence of these oxides. It is expected that the fundamental understanding extracted from our experimental study could aid the further design and optimization of oxide-derived Cu catalysts.

APPENDIX A: LIST OF PUBLICATIONS

1. Mistry, H.; Reske, R.; Strasser, P.; Roldan Cuenya, B. *Catal. Today* **2016**, in print.
2. Ahmadi, M.; Mistry, H.; Roldan Cuenya, B. *J. Phys. Chem. Lett.* **2016**, *7*, 3519.
3. Mistry, H.; Varela, A. S.; Bonifacio, C. S.; Zegkinoglou, I.; Sinev, I.; Choi, Y.; Kisslinger, K.; Stach, E. A.; Yang, J. C.; Strasser, P.; Roldan Cuenya, B. *Nat. Commun.* **2016**, *7*, 12123.
4. Choi, Y.; Sinev, I.; Mistry, H.; Zegkinoglou, I.; Roldan Cuenya, B. *ACS Catal.* **2016**, *6*, 3396.
5. Mistry, H.; Varela, A. S.; Kühl, S.; Strasser, P.; Roldan Cuenya, B. *Nature Rev. Mater.* **2016**, *1*, 16009.
6. Mistry, H.; Behafarid, F.; Reske, R.; Varela, A. S.; Strasser, P.; Roldan Cuenya, B. *ACS Catal.* **2016**, *6*, 1075.
7. Ahmadi, M.; Cui, C.; Mistry, H.; Strasser, P.; Roldan Cuenya, B. *ACS Nano* **2015**, *9*, 10686.
8. Mistry, H.; Reske, R.; Zeng, Z.; Zhao, Z.-J.; Greeley, J.; Strasser, P.; Roldan Cuenya, B. *J. Am. Chem. Soc.* **2014**, *136*, 16473.
9. Reske, R.; Mistry, H.; Behafarid, F.; Roldan Cuenya, B.; Strasser, P. *J. Am. Chem. Soc.* **2014**, *136*, 6978.
10. Mistry, H.; Behafarid, F.; Zhou, E.; Ono, L. K.; Zhang, L.; Roldan Cuenya, B. *ACS Catal.* **2014**, *4*, 109.
11. Mistry, H.; Behafarid, F.; Bare, S. R.; Roldan Cuenya, B. *ChemCatChem* **2014**, *6*, 348.

APPENDIX B: COPYRIGHT PERMISSIONS

Title: Shape-Dependent Catalytic Oxidation of 2-Butanol over Pt Nanoparticles Supported on γ-Al2O3

Author: H. Mistry, F. Behafarid, E. Zhou, et al

Publication: ACS Catalysis

Publisher: American Chemical Society

Date: Jan 1, 2014

PERMISSION/LICENSE IS GRANTED FOR YOUR ORDER AT NO CHARGE

This type of permission/license, instead of the standard Terms & Conditions, is sent to you because no fee is being charged for your order. Please note the following:

- Permission is granted for your request in both print and electronic formats, and translations.
- If figures and/or tables were requested, they may be adapted or used in part.
- Please print this page for your records and send a copy of it to your publisher/graduate school.
- Appropriate credit for the requested material should be given as follows: "Reprinted (adapted) with permission from (COMPLETE REFERENCE CITATION). Copyright (YEAR) American Chemical Society." Insert appropriate information in place of the capitalized words.
- One-time permission is granted only for the use specified in your request. No additional uses are granted (such as derivative works or other editions). For any other uses, please submit a new request.

BACK CLOSE WINDOW

JOHN WILEY AND SONS LICENSE TERMS AND CONDITIONS

Oct 12, 2016

This Agreement between Hemma Mistry ("You") and John Wiley and Sons ("John Wiley and Sons") consists of your license details and the terms and conditions provided by John Wiley and Sons and Copyright Clearance Center.

License Number	3966561325682
License date	Oct 12, 2016
Licensed Content Publisher	John Wiley and Sons
Licensed Content Publication	ChemCatChem
Licensed Content Title	Pressure-Dependent Effect of Hydrogen Adsorption on Structural and Electronic Properties of Pt/γ-Al2O3 Nanoparticles
Licensed Content Author	Hemma Mistry,Farzad Behafarid,Simon R. Bare,B. Roldan Cuenya
Licensed Content Date	Nov 15, 2013
Licensed Content Pages	5
Type of use	Dissertation/Thesis
Requestor type	Author of this Wiley article
Format	Print
Portion	Full article
Will you be translating?	No
Title of your thesis / dissertation	Model Nanocatalysts with Tunable Reactivity: Tailoring the Structure and Surface Chemistry of Nanomaterials for Energy and Alternative Fuels Catalysis
Expected completion date	Dec 2016
Expected size (number of pages)	170
Requestor Location	Hemma Mistry 4000 Central Florida Blvd Building 121, PS430 ORLANDO, FL 32816 United States Attn: Hemma Mistry
Publisher Tax ID	EU826007151
Billing Type	Invoice
Billing Address	Hemma Mistry 4000 Central Florida Blvd Building 121, PS430 ORLANDO, FL 32816 United States Attn: Hemma Mistry
Total	0.00 USD
Terms and Conditions	

TERMS AND CONDITIONS

RightsLink®

Home | Create Account | Help | Live Chat

Title: Exceptional Size-Dependent Activity Enhancement in the Electroreduction of CO2 over Au Nanoparticles

Author: Hemma Mistry, Rulle Reske, Zhenhua Zeng, et al

Publication: Journal of the American Chemical Society

Publisher: American Chemical Society

Date: Nov 1, 2014

LOGIN

If you're a copyright.com user, you can login to RightsLink using your copyright.com credentials. Already a RightsLink user or want to learn more?

PERMISSION/LICENSE IS GRANTED FOR YOUR ORDER AT NO CHARGE

This type of permission/license, instead of the standard Terms & Conditions, is sent to you because no fee is being charged for your order. Please note the following:

- Permission is granted for your request in both print and electronic formats, and translations.
- If figures and/or tables were requested, they may be adapted or used in part.
- Please print this page for your records and send a copy of it to your publisher/graduate school.
- Appropriate credit for the requested material should be given as follows: "Reprinted (adapted) with permission from (COMPLETE REFERENCE CITATION). Copyright (YEAR) American Chemical Society." Insert appropriate information in place of the capitalized words.
- One-time permission is granted only for the use specified in your request. No additional uses are granted (such as derivative works or other editions). For any other uses, please submit a new request.

BACK CLOSE WINDOW

Copyright Clearance Center RightsLink®

Home | Create Account | Help | Live Chat

ACS Publications Most Trusted. Most Cited. Most Read.

Title:	Particle Size Effects in the Catalytic Electroreduction of CO2 on Cu Nanoparticles
Author:	Rulle Reske, Hemma Mistry, Farzad Behafarid, et al
Publication:	Journal of the American Chemical Society
Publisher:	American Chemical Society
Date:	May 1, 2014

LOGIN

If you're a copyright.com user, you can login to RightsLink using your copyright.com credentials. Already a **RightsLink user** or want to learn more?

PERMISSION/LICENSE IS GRANTED FOR YOUR ORDER AT NO CHARGE

This type of permission/license, instead of the standard Terms & Conditions, is sent to you because no fee is being charged for your order. Please note the following:

- Permission is granted for your request in both print and electronic formats, and translations.
- If figures and/or tables were requested, they may be adapted or used in part.
- Please print this page for your records and send a copy of it to your publisher/graduate school.
- Appropriate credit for the requested material should be given as follows: "Reprinted (adapted) with permission from (COMPLETE REFERENCE CITATION). Copyright (YEAR) American Chemical Society." Insert appropriate information in place of the capitalized words.
- One-time permission is granted only for the use specified in your request. No additional uses are granted (such as derivative works or other editions). For any other uses, please submit a new request.

BACK CLOSE WINDOW

REFERENCES

(1) Mistry, H.; Varela, A. S.; Kuehl, S.; Strasser, P.; Roldan Cuenya, B. *Nat. Rev. Mater.* **2016**, *1*, 16009.

(2) Reske, R.; Mistry, H.; Behafarid, F.; Roldan Cuenya, B.; Strasser, P. *J. Am. Chem. Soc.* **2014**, *136*, 6978.

(3) Mistry, H.; Reske, R.; Zeng, Z.; Zhao, Z.-J.; Greeley, J.; Strasser, P.; Cuenya, B. R. *J. Am. Chem. Soc.* **2014**, *136*, 16473.

(4) Mistry, H.; Reske, R.; Strasser, P.; Roldan Cuenya, B. *Catal. Today* **2016**.

(5) Kleis, J.; Greeley, J.; Romero, N.; Morozov, V.; Falsig, H.; Larsen, A. H.; Lu, J.; Mortensen, J. J.; Dułak, M.; Thygesen, K. S. *Catal. Lett.* **2011**, *141*, 1067.

(6) Naitabdi, A.; Ono, L.; Roldan Cuenya, B. *Appl. Phys. Lett.* **2006**, *89*, 043101.

(7) Narayanan, R.; El-Sayed, M. A. *J. Phys. Chem. B* **2005**, *109*, 12663.

(8) Narayanan, R.; El-Sayed, M. A. *Nano Lett.* **2004**, *4*, 1343.

(9) Yin, A.-X.; Min, X.-Q.; Zhang, Y.-W.; Yan, C.-H. *J. Am. Chem. Soc.* **2011**, *133*, 3816.

(10) Tian, N.; Zhou, Z.-Y.; Yu, N.-F.; Wang, L.-Y.; Sun, S.-G. *J. Am. Chem. Soc.* **2010**, *132*, 7580.

(11) Mistry, H.; Behafarid, F.; Zhou, E.; Ono, L.; Zhang, L.; Roldan Cuenya, B. *ACS Catal.* **2013**, *4*, 109.

(12) Ahmadi, M.; Behafarid, F.; Holse, C.; Nielsen, J. H.; Roldan Cuenya, B. *J. Phys. Chem. C* **2015**, *119*, 29178.

(13) Mistry, H.; Behafarid, F.; Bare, S. R.; Roldan Cuenya, B. *ChemCatChem* **2014**, *6*, 348.

(14) Mager-Maury, C.; Bonnard, G.; Chizallet, C.; Sautet, P.; Raybaud, P. *ChemCatChem* **2011**, *3*, 200.

(15) Ahmadi, M.; Mistry, H.; Roldan Cuenya, B. *J. Phys. Chem. Lett.* **2016**, *7*, 3519.

(16) Kitchin, J. R.; Nørskov, J. K.; Barteau, M. A.; Chen, J. G. *Phys. Rev. Lett.* **2004**, *93*, 156801.

(17) Kitchin, J.; Nørskov, J. K.; Barteau, M.; Chen, J. *J. Chem. Phys.* **2004**, *120*, 10240.

(18) Stamenkovic, V.; Mun, B. S.; Mayrhofer, K. J.; Ross, P. N.; Markovic, N. M.; Rossmeisl, J.; Greeley, J.; Nørskov, J. K. *Angew. Chem.* **2006**, *118*, 2963.

(19) Hammer, B.; Nørskov, J. K. *Advances in catalysis* **2000**, *45*, 71.

(20) Mavrikakis, M.; Hammer, B.; Nørskov, J. K. *Phys. Rev. Lett.* **1998**, *81*, 2819.

(21) Zhou, W. P.; Lewera, A.; Larsen, R.; Masel, R. I.; Bagus, P. S.; Wieckowski, A. *J. Phys. Chem. B* **2006**, *110*, 13393.

(22) Strasser, P.; Koh, S.; Anniyev, T.; Greeley, J.; More, K.; Yu, C.; Liu, Z.; Kaya, S.; Nordlund, D.; Ogasawara, H.; Toney, M. F.; Nilsson, A. *Nat Chem* **2010**, *2*, 454.

(23) Kibler, L. A.; El-Aziz, A. M.; Hoyer, R.; Kolb, D. M. *Angew. Chem. Int. Ed.* **2005**, *44*, 2080.

(24) Lima, F. H. B.; Zhang, J.; Shao, M. H.; Sasaki, K.; Vukmirovic, M. B.; Ticianelli, E. A.; Adzic, R. R. *J. Phys. Chem. C* **2007**, *111*, 404.

(25) Gorzkowski, M. T.; Lewera, A. *J. Phys. Chem. C* **2015**, *119*, 18389.

(26) Gao, F.; Goodman, D. W. *Chem. Soc. Rev.* **2012**, *41*, 8009.

(27) Chen, M.; Kumar, D.; Yi, C.-W.; Goodman, D. W. *Science* **2005**, *310*, 291.

(28) Karamad, M.; Tripkovic, V.; Rossmeisl, J. *ACS Catal.* **2014**, *4*, 2268.

(29) Slanac, D. A.; Hardin, W. G.; Johnston, K. P.; Stevenson, K. J. *J. Am. Chem. Soc.* **2012**, *134*, 9812.

(30) Lu, C.; Rice, C.; Masel, R.; Babu, P.; Waszczuk, P.; Kim, H.; Oldfield, E.; Wieckowski, A. *J. Phys. Chem. B* **2002**, *106*, 9581.

(31) Simonsen, S. B.; Chorkendorff, I.; Dahl, S.; Skoglundh, M.; Sehested, J.; Helveg, S. *J. Catal.* **2011**, *281*, 147.

(32) Simonsen, S. B.; Chorkendorff, I.; Dahl, S.; Skoglundh, M.; Sehested, J.; Helveg, S. *J. Am. Chem. Soc.* **2010**, *132*, 7968.

(33) Behafarid, F.; Pandey, S.; Diaz, R. E.; Stach, E. A.; Cuenya, B. R. *PCCP* **2014**, *16*, 18176.

(34) Matos, J.; Ono, L.; Behafarid, F.; Croy, J.; Mostafa, S.; DeLaRiva, A.; Datye, A.; Frenkel, A.; Cuenya, B. R. *PCCP* **2012**, *14*, 11457.

(35) Choi, Y.; Sinev, I.; Mistry, H.; Zegkinoglou, I.; Roldan Cuenya, B. *ACS Catal.* **2016**, *6*, 3396.

(36) Xin, H. L.; Pach, E. A.; Diaz, R. E.; Stach, E. A.; Salmeron, M.; Zheng, H. *ACS Nano* **2012**, *6*, 4241.

(37) Porsgaard, S.; Merte, L. R.; Ono, L. K.; Behafarid, F.; Matos, J.; Helveg, S.; Salmeron, M.; Roldan Cuenya, B.; Besenbacher, F. *ACS nano* **2012**, *6*, 10743.

(38) Lira, E.; Merte, L.; Behafarid, F.; Ono, L.; Zhang, L.; Roldan Cuenya, B. *ACS Catal.* **2014**, *4*, 1875.

(39) Paredis, K.; Ono, L. K.; Behafarid, F.; Zhang, Z.; Yang, J. C.; Frenkel, A. I.; Cuenya, B. R. *J. Am. Chem. Soc.* **2011**, *133*, 13455.

(40) Ahmadi, M.; Cui, C.; Mistry, H.; Strasser, P.; Roldan Cuenya, B. *ACS Nano* **2015**, *9*, 10686.

(41) Papaefthimiou, V.; Diebold, M.; Ulhaq-Bouillet, C.; Doh, W. H.; Blume, R.; Zafeiratos, S.; Savinova, E. R. *ChemElectroChem* **2015**, *2*, 1519.

(42) Tao, F. F.; Zhang, S.; Nguyen, L.; Zhang, X. *Chem. Soc. Rev.* **2012**, *41*, 7980.

(43) Hori, Y. In *Modern aspects of electrochemistry*; Springer: 2008, p 89.

(44) Hori, Y.; Murata, A.; Takahashi, R. *J. Chem. Soc. Farad. T. 1* **1989**, *85*, 2309.

(45) Vajda, S.; Pellin, M. J.; Greeley, J. P.; Marshall, C. L.; Curtiss, L. A.; Ballentine, G. A.; Elam, J. W.; Catillon-Mucherie, S.; Redfern, P. C.; Mehmood, F. *Nat. Mater.* **2009**, *8*, 213.

(46) Nielsen, J. H.; Hansen, T. W.; Nilsson, A.; Stephens, I.; Chorkendorff, I. *Nat. Chem* **2014**, *6*, 732.

(47) Kaden, W. E.; Wu, T.; Kunkel, W. A.; Anderson, S. L. *Science* **2009**, *326*, 826.

(48) Ahmadi, T. S.; Wang, Z. L.; Green, T. C.; Henglein, A.; El-Sayed, M. A. *Science* **1996**, *272*, 1924.

(49) Somorjai, G. A.; Park, J. Y. *Top. Catal.* **2008**, *49*, 126.

(50) You, H.; Yang, S.; Ding, B.; Yang, H. *Chem. Soc. Rev.* **2013**, *42*, 2880.

(51) Varela, A. S.; Ranjbar Sahraie, N.; Steinberg, J.; Ju, W.; Oh, H.-S.; Strasser, P. *Angew. Chem. Int. Ed.* **2015**, *54*, 10758.

(52) Guo, D.; Shibuya, R.; Akiba, C.; Saji, S.; Kondo, T.; Nakamura, J. *Science* **2016**, *351*, 361.

(53) Gong, K.; Du, F.; Xia, Z.; Durstock, M.; Dai, L. *science* **2009**, *323*, 760.

(54) Zhuang, Z.; Giles, S. A.; Zheng, J.; Jenness, G. R.; Caratzoulas, S.; Vlachos, D. G.; Yan, Y. *Nat. Commun.* **2016**, *7*, 10141.

(55) Radnik, J.; Mohr, C.; Claus, P. *PCCP* **2003**, *5*, 172.

(56) Roldan Cuenya, B.; Baeck, S.-H.; Jaramillo, T. F.; McFarland, E. W. *J. Am. Chem. Soc.* **2003**, *125*, 12928.

(57) Howard, A.; Clark, D. N. S.; Mitchell, C. E. J.; Egdell, R. G.; Dhanak, V. R. *Surf. Sci.* **2002**, *518*, 210.

(58) Wertheim, G.; DiCenzo, S. *Phys. Rev. B* **1988**, *37*, 844.

(59) Ravel, B.; Newville, M. *J. Synchrotron Radiat.* **2005**, *12*, 537.

(60) Ankudinov, A.; Ravel, B.; Rehr, J.; Conradson, S. *Phys. Rev. B* **1998**, *58*, 7565.

(61) Azalim, S.; Franco, M.; Brahmi, R.; Giraudon, J.-M.; Lamonier, J.-F. *J. Hazard. Mater.* **2011**, *188*, 422.

(62) Spivey, J. J. *Industrial & Engineering Chemistry Research* **1987**, *26*, 2165.

(63) Papaefthimiou, P.; Ioannides, T.; Verykios, X. E. *Appl. Catal. B: Environ.* **1997**, *13*, 175.

(64) Hermia, J.; Vigneron, S. *Catal. Today* **1993**, *17*, 349.

(65) Everaert, K.; Baeyens, J. *J. Hazard. Mater.* **2004**, *109*, 113.

(66) Papaefthimiou, P.; Ioannides, T.; Verykios, X. *Appl. Therm. Eng.* **1998**, *18*, 1005.

(67) Abbasi, Z.; Haghighi, M.; Fatehifar, E.; Saedy, S. *J. Hazard. Mater.* **2011**, *186*, 1445.

(68) Takamitsu, Y.; Yoshida, S.; Kobayashi, W.; Ogawa, H.; Sano, T. *Journal of Environmental Science and Health, Part A* **2013**, *48*, 667.

(69) Wang, Z.; Ma, H.; Zhu, W.; Wang, G. *React. Kinet. Catal. Lett.* **2002**, *76*, 271.

(70) Hou, W.; Dehm, N. A.; Scott, R. W. *J. Catal.* **2008**, *253*, 22.

(71) Yan, T.; Gong, J.; Mullins, C. B. *J. Am. Chem. Soc.* **2009**, *131*, 16189.

(72) Fang, D.; Ren, W.; Liu, Z.; Xu, X.; Xu, L.; Lü, H.; Liao, W.; Zhang, H. *Journal of Natural Gas Chemistry* **2009**, *18*, 179.

(73) Vinod, C. P.; Wilson, K.; Lee, A. F. *J. Chem. Technol. Biotechnol.* **2011**, *86*, 161.

(74) Nahar, G.; Madhani, S. *Int. J. Hydrogen Energy* **2010**, *35*, 98.

(75) Wang, W.; Cao, Y. *Int. J. Hydrogen Energy* **2011**, *36*, 2887.

(76) Wang, W.; Cao, Y. *Int. J. Hydrogen Energy* **2010**, *35*, 13280.

(77) Dagaut, P.; Sarathy, S.; Thomson, M. *Proceedings of the combustion Institute* **2009**, *32*, 229.

(78) Croy, J. R.; Mostafa, S.; Liu, J.; Sohn, Y.-h.; Roldan Cuenya, B. *Catal. Lett.* **2007**, *118*, 1.

(79) Mostafa, S.; Behafarid, F.; Croy, J. R.; Ono, L. K.; Li, L.; Yang, J. C.; Frenkel, A. I.; Roldan Cuenya, B. *J. Am. Chem. Soc.* **2010**, *132*, 15714.

(80) Xu, R.; Wang, D.; Zhang, J.; Li, Y. *Chem.–Asian J.* **2006**, *1*, 888.

(81) Bratlie, K. M.; Lee, H.; Komvopoulos, K.; Yang, P.; Somorjai, G. A. *Nano Lett.* **2007**, *7*, 3097.

(82) Zaera, F. *J. Phys. Chem. Lett.* **2010**, *1*, 621.

(83) Roldan Cuenya, B. *Thin Solid Films* **2010**, *518*, 3127.

(84) Croy, J. R.; Mostafa, S.; Liu, J.; Sohn, Y.; Heinrich, H.; Roldan Cuenya, B. *Catal. Lett.* **2007**, *119*, 209.

(85) Comotti, M.; Li, W.-C.; Spliethoff, B.; Schüth, F. *J. Am. Chem. Soc.* **2006**, *128*, 917.

(86) Sathish, M.; Viswanath, R. *Catal. Today* **2007**, *129*, 421.

(87) Bonanni, S.; Aït-Mansour, K.; Harbich, W.; Brune, H. *J. Am. Chem. Soc.* **2012**, *134*, 3445.

(88) Singh, J.; Alayon, E.; Tromp, M.; Safonova, O. V.; Glatzel, P.; Nachtegaal, M.; Frahm, R.; van Bokhoven, J. A. *Angew. Chem. Int. Ed.* **2008**, *47*, 9260.

(89) Ackermann, M.; Pedersen, T.; Hendriksen, B.; Robach, O.; Bobaru, S.; Popa, I.; Quiros, C.; Kim, H.; Hammer, B.; Ferrer, S. *Phys. Rev. Lett.* **2005**, *95*, 255505.

(90) Balint, I.; Miyazaki, A.; Aika, K.-i. *J. Catal.* **2003**, *220*, 74.

(91) Merte, L. R.; Ahmadi, M.; Behafarid, F.; Ono, L. K.; Lira, E.; Matos, J.; Li, L.; Yang, J. C.; Roldan Cuenya, B. *ACS Catal.* **2013**, *3*, 1460.

(92) Li, Z.; Tysoe, W. T. *Surf. Sci.* **2010**, *604*, 1377.

(93) Lambert, S.; Cellier, C.; Ferauche, F.; Gaigneaux, É. M.; Heinrichs, B. *Catal. Commun.* **2007**, *8*, 2032.

(94) Sedjame, H.-J.; Lafaye, G.; Barbier, J. *Appl. Catal. B: Environ.* **2013**, *132*, 132.

(95) Wang, T.; Shou, H.; Kou, Y.; Liu, H. *Green Chem.* **2009**, *11*, 562.

(96) Roldan Cuenya, B. *Acc. Chem. Res.* **2012**, *46*, 1682.

(97) Ma, R.; Semagina, N. *J. Phys. Chem. C* **2010**, *114*, 15417.

(98) Newville, M. *J. Synchrotron Radiat.* **2001**, *8*, 322.

(99) Ankudinov, A.; Bouldin, C.; Rehr, J.; Sims, J.; Hung, H. *Phys. Rev. B* **2002**, *65*, 104107.

(100) Roldan Cuenya, B.; Frenkel, A.; Mostafa, S.; Behafarid, F.; Croy, J.; Ono, L.; Wang, Q. *Phys. Rev. B* **2010**, *82*, 155450.

(101) Roldan Cuenya, B.; Croy, J. R.; Mostafa, S.; Behafarid, F.; Li, L.; Zhang, Z.; Yang, J. C.; Wang, Q.; Frenkel, A. I. *J. Am. Chem. Soc.* **2010**, *132*, 8747.

(102) Frenkel, A. I.; Hills, C. W.; Nuzzo, R. G. *J. Phys. Chem. B* **2001**, *105*, 12689.

(103) Paredis, K.; Ono, L. K.; Mostafa, S.; Li, L.; Zhang, Z.; Yang, J. C.; Barrio, L.; Frenkel, A. I.; Roldan Cuenya, B. *J. Am. Chem. Soc.* **2011**, *133*, 6728.

(104) Ono, L. K.; Croy, J. R.; Heinrich, H.; Roldan Cuenya, B. *J. Phys. Chem. C* **2011**, *115*, 16856.

(105) Wang, C.-B.; Yeh, C.-T. *J. Catal.* **1998**, *178*, 450.

(106) Xu, Y.; Shelton, W. A.; Schneider, W. F. *J. Phys. Chem. B* **2006**, *110*, 16591.

(107) Arnby, K.; Assiks, J.; Carlsson, P.-A.; Palmqvist, A.; Skoglundh, M. *J. Catal.* **2005**, *233*, 176.

(108) Völter, J.; Lietz, G.; Spindler, H.; Lieske, H. *J. Catal.* **1987**, *104*, 375.

(109) Carlsson, P.-A.; Mollner, S.; Arnby, K.; Skoglundh, M. *Chem. Eng. Sci.* **2004**, *59*, 4313.

(110) Yazawa, Y.; Yoshida, H.; Hattori, T. *Appl. Catal. A: Gen.* **2002**, *237*, 139.

(111) Radic, N.; Grbic, B.; Terlecki-Baricevic, A. *Appl. Catal. B: Environ.* **2004**, *50*, 153.

(112) Garetto, T. F.; Apesteguía, C. R. *Catal. Today* **2000**, *62*, 189.

(113) Garetto, T. F.; Apesteguía, C. R. *Appl. Catal. B: Environ.* **2001**, *32*, 83.

(114) Otto, K.; Andino, J. M.; Parks, C. L. *J. Catal.* **1991**, *131*, 243.

(115) Gololobov, A. M.; Bekk, I. E.; Bragina, G. O.; Zaikovskii, V. I.; Ayupov, A. B.; Telegina, N. S.; Bukhtiyarov, V. I.; Stakheev, A. Y. *Kinet. Catal.* **2009**, *50*, 830.

(116) Briot, P.; Auroux, A.; Jones, D.; Primet, M. *Applied Catalysis* **1990**, *59*, 141.

(117) Carballo, L. M.; Wolf, E. E. *J. Catal.* **1978**, *53*, 366.

(118) Yang, J.; Tschamber, V.; Habermacher, D.; Garin, F.; Gilot, P. *Appl. Catal. B: Environ.* **2008**, *83*, 229.

(119) Zaera, F. *PCCP* **2013**, *15*, 11988.

(120) Rylander, P. N.; Academic Press: New York, NY, 1967.

(121) Cui, C.; Ahmadi, M.; Behafarid, F.; Gan, L.; Neumann, M.; Heggen, M.; Cuenya, B. R.; Strasser, P. *Faraday Discuss.* **2013**, *162*, 91.

(122) Wieckowski, A.; Savinova, E. R.; Vayenas, C. G. *Catalysis and electrocatalysis at nanoparticle surfaces*; CRC Press, 2003.

(123) Li, Y.; Yang, R. T. *J. Phys. Chem. C* **2007**, *111*, 11086.

(124) Wang, L.; Yang, R. T. *J. Phys. Chem. C* **2008**, *112*, 12486.

(125) Mukerjee, S. *J. Appl. Electrochem.* **1990**, *20*, 537.

(126) Yamauchi, M.; Kobayashi, H.; Kitagawa, H. *ChemPhysChem* **2009**, *10*, 2566.

(127) Vaarkamp, M.; Miller, J. T.; Modica, F. S.; Koningsberger, D. C. *J. Catal.* **1996**, *163*, 294.

(128) Zhou, C.; Wu, J.; Nie, A.; Forrey, R. C.; Tachibana, A.; Cheng, H. *J. Phys. Chem. C* **2007**, *111*, 12773.

(129) Behafarid, F.; Ono, L.; Mostafa, S.; Croy, J.; Shafai, G.; Hong, S.; Rahman, T.; Bare, S. R.; Roldan Cuenya, B. *PCCP* **2012**, *14*, 11766.

(130) Oudenhuijzen, M. K.; van Bokhoven, J. A.; Miller, J. T.; Ramaker, D. E.; Koningsberger, D. C. *J. Am. Chem. Soc.* **2005**, *127*, 1530.

(131) Spenadel, L.; Boudart, M. *J. Phys. Chem.* **1960**, *64*, 204.

(132) Kip, B. J.; Duivenvoorden, F. B. M.; Koningsberger, D. C.; Prins, R. *J. Catal.* **1987**, *105*, 26.

(133) Singh, J.; Nelson, R. C.; Vicente, B. C.; Scott, S. L.; van Bokhoven, J. A. *PCCP* **2010**, *12*, 5668.

(134) Bus, E.; van Bokhoven, J. A. *PCCP* **2007**, *9*, 2894.

(135) Petkov, P. S.; Petrova, G. P.; Vayssilov, G. N.; Rösch, N. *J. Phys. Chem. C* **2010**, *114*, 8500.

(136) Vargas, A.; Santarossa, G.; Baiker, A. *J. Phys. Chem. C* **2011**, *115*, 10661.

(137) Hu, C. H.; Chizallet, C.; Mager-Maury, C.; Corral-Valero, M.; Sautet, P.; Toulhoat, H.; Raybaud, P. *J. Catal.* **2010**, *274*, 99.

(138) Lei, Y.; Jelic, J.; Nitsche, L. C.; Meyer, R.; Miller, J. *Top. Catal.* **2011**, *54*, 334.

(139) Sanchez, S. I.; Menard, L. D.; Bram, A.; Kang, J. H.; Small, M. W.; Nuzzo, R. G.; Frenkel, A. I. *J. Am. Chem. Soc.* **2009**, *131*, 7040.

(140) Rupprechter, G.; Freund, H.-J. *Top. Catal.* **2000**, *14*, 3.

(141) Chen, L.; Zhou, C.-g.; Wu, J.-p.; Cheng, H.-s. *Front. Phys. China* **2009**, *4*, 356.

(142) Small, M. W.; Sanchez, S. I.; Marinkovic, N. S.; Frenkel, A. I.; Nuzzo, R. G. *ACS Nano* **2012**, *6*, 5583.

(143) Jensen, C.; Buck, D.; Dilger, H.; Bauer, M.; Phillipp, F.; Roduner, E. *Chem. Commun.* **2013**, *49*, 588.

(144) Ji, Y.; Koot, V.; van der Eerden, A. M. J.; Weckhuysen, B. M.; Koningsberger, D. C.; Ramaker, D. E. *J. Catal.* **2007**, *245*, 415.

(145) Guo, N.; Fingland, B. R.; Williams, W. D.; Kispersky, V. F.; Jelic, J.; Delgass, W. N.; Ribeiro, F. H.; Meyer, R. J.; Miller, J. T. *PCCP* **2010**, *12*, 5678.

(146) Alexeev, O. S.; Li, F.; Amiridis, M. D.; Gates, B. C. *J. Phys. Chem. B* **2005**, *109*, 2338.

(147) Kubota, T.; Asakura, K.; Ichikuni, N.; Iwasawa, Y. *Chem. Phys. Lett.* **1996**, *256*, 445.

(148) Ramaker, D. E.; Koningsberger, D. C. *PCCP* **2010**, *12*, 5514.

(149) Reifsnyder, S. N.; Otten, M. M.; Sayers, D. E.; Lamb, H. H. *J. Phys. Chem. B* **1997**, *101*, 4972.

(150) Bordiga, S.; Groppo, E.; Agostini, G.; van Bokhoven, J. A.; Lamberti, C. *Chem. Rev.* **2013**, *113*, 1736.

(151) Teliska, M.; O'Grady, W. E.; Ramaker, D. E. *J. Phys. Chem. B* **2004**, *108*, 2333.

(152) Roldan Cuenya, B.; Alcántara Ortigoza, M.; Ono, L. K.; Behafarid, F.; Mostafa, S.; Croy, J. R.; Paredis, K.; Shafai, G.; Rahman, T. S.; Li, L.; Zhang, Z.; Yang, J. C. *Phys. Rev. B* **2011**, *84*, 245438.

(153) Bare, S. R.; Yang, N.; Kelly, S. D.; Mickelson, G. E.; Modica, F. S. *Catal. Today* **2007**, *126*, 18.

(154) Stakheev, A. Y.; Zhang, Y.; Ivanov, A. V.; Baeva, G. N.; Ramaker, D. E.; Koningsberger, D. C. *J. Phys. Chem. C* **2007**, *111*, 3938.

(155) Di Vece, M.; Grandjean, D.; Van Bael, M. J.; Romero, C. P.; Wang, X.; Decoster, S.; Vantomme, A.; Lievens, P. *Phys. Rev. Lett.* **2008**, *100*, 236105.

(156) Hakamada, M.; Furukawa, T.; Yamamoto, T.; Takahashi, M.; Mabuchi, M. *Mater. Trans.* **2011**, *52*, 806.

(157) Bus, E.; Miller, J. T.; Kropf, A. J.; Prins, R.; van Bokhoven, J. A. *PCCP* **2006**, *8*, 3248.

(158) Hu, B.; Guild, C.; Suib, S. L. *J. CO2 Util.* **2013**, *1*, 18.

(159) Whipple, D. T.; Kenis, P. J. *J. Phys. Chem. Lett.* **2010**, *1*, 3451.

(160) Hori, Y.; Kikuchi, K.; Suzuki, S. *Chem. Lett.* **1985**, *14*, 1695.

(161) Hori, Y.; Takahashi, I.; Koga, O.; Hoshi, N. *J. Phys. Chem. B* **2002**, *106*, 15.

(162) Schouten, K.; Kwon, Y.; Van der Ham, C.; Qin, Z.; Koper, M. *Chemical Science* **2011**, *2*, 1902.

(163) Schouten, K. J. P.; Qin, Z.; Gallent, E. P. r.; Koper, M. T. *J. Am. Chem. Soc.* **2012**, *134*, 9864.

(164) Peterson, A. A.; Abild-Pedersen, F.; Studt, F.; Rossmeisl, J.; Nørskov, J. K. *Energ. Eviron. Sci.* **2010**, *3*, 1311.

(165) Peterson, A. A.; Nørskov, J. K. *J. Phys. Chem. Lett.* **2012**, *3*, 251.

(166) Hansen, H. A.; Varley, J. B.; Peterson, A. A.; Nørskov, J. K. *J. Phys. Chem. Lett.* **2013**, *4*, 388.

(167) Jhong, H.-R. M.; Ma, S.; Kenis, P. J. A. *Curr. Opin. Chem. Eng.* **2013**, *2*, 191.

(168) Noda, H.; Ikeda, S.; Yamamoto, A.; Einaga, H.; Ito, K. *Bull. Chem. Soc. Jpn.* **1995**, *68*, 1889.

(169) Hori, Y.; Murata, A.; Kikuchi, K.; Suzuki, S. *J. Chem. Soc., Chem. Commun.* **1987**, 728.

(170) Chen, Y.; Li, C. W.; Kanan, M. W. *J. Am. Chem. Soc.* **2012**, *134*, 19969.

(171) Kauffman, D. R.; Alfonso, D.; Matranga, C.; Qian, H.; Jin, R. *J. Am. Chem. Soc.* **2012**, *134*, 10237.

(172) Zhu, W.; Zhang, Y.-J.; Zhang, H.; Lv, H.; Li, Q.; Michalsky, R.; Peterson, A. A.; Sun, S. *J. Am. Chem. Soc.* **2014**, *136*, 16132.

(173) Feng, X.; Jiang, K.; Fan, S.; Kanan, M. W. *J. Am. Chem. Soc.* **2015**, *137*, 4606.

(174) Ono, L.; Sudfeld, D.; Roldan Cuenya, B. *Surf. Sci.* **2006**, *600*, 5041.

(175) Ono, L. K.; Roldan Cuenya, B. *J. Phys. Chem. C* **2008**, *112*, 4676.

(176) Zhu, W.; Michalsky, R.; Metin, O. n.; Lv, H.; Guo, S.; Wright, C. J.; Sun, X.; Peterson, A. A.; Sun, S. *J. Am. Chem. Soc.* **2013**, *135*, 16833.

(177) Shi, C.; Hansen, H. A.; Lausche, A. C.; Nørskov, J. K. *PCCP* **2014**, *16*, 4720.

(178) Greeley, J.; Jaramillo, T. F.; Bonde, J.; Chorkendorff, I.; Nørskov, J. K. *Nat. Mater.* **2006**, *5*, 909.

(179) Greeley, J.; Nørskov, J. K.; Kibler, L. A.; El-Aziz, A. M.; Kolb, D. M. *ChemPhysChem* **2006**, *7*, 1032.

(180) Greeley, J.; Nørskov, J. K. *Surf. Sci.* **2007**, *601*, 1590.

(181) Gattrell, M.; Gupta, N.; Co, A. *J. Electroanal. Chem.* **2006**, *594*, 1.

(182) Hori, Y.; Takahashi, R.; Yoshinami, Y.; Murata, A. *J. Phys. Chem. B* **1997**, *101*, 7075.

(183) Durand, W. J.; Peterson, A. A.; Studt, F.; Abild-Pedersen, F.; Nørskov, J. K. *Surf. Sci.* **2011**, *605*, 1354.

(184) Li, C. W.; Kanan, M. W. *J. Am. Chem. Soc.* **2012**, *134*, 7231.

(185) Tang, W.; Peterson, A. A.; Varela, A. S.; Jovanov, Z. P.; Bech, L.; Durand, W. J.; Dahl, S.; Nørskov, J. K.; Chorkendorff, I. *PCCP* **2012**, *14*, 76.

(186) Nie, X.; Esopi, M. R.; Janik, M. J.; Asthagiri, A. *Angew. Chem. Int. Ed.* **2013**, *52*, 2459.

(187) Christophe, J.; Doneux, T.; Buess-Herman, C. *Electrocatal.* **2012**, *3*, 139.

(188) Vollmer, S.; Witte, G.; Wöll, C. *Catal. Lett.* **2001**, *77*, 97.

(189) Molodkina, E. B.; Ehrenburg, M. R.; Polukarov, Y. M.; Danilov, A. I.; Souza-Garcia, J.; Feliu, J. M. *Electrochim. Acta* **2010**, *56*, 154.

(190) Oezaslan, M.; Hasché, F.; Strasser, P. *J. Electrochem. Soc.* **2012**, *159*, B444.

(191) Reske, R.; Duca, M.; Oezaslan, M.; Schouten, K. J. P.; Koper, M. T.; Strasser, P. *J. Phys. Chem. Lett.* **2013**, *4*, 2410.

(192) Coq, B.; Figueras, F. *Coord. Chem. Rev.* **1998**, *178–180, Part 2*, 1753.

(193) Bond, G. C. *Surf. Sci.* **1985**, *156*, 966.

(194) Li, L.; Larsen, A. H.; Romero, N. A.; Morozov, V. A.; Glinsvad, C.; Abild-Pedersen, F.; Greeley, J.; Jacobsen, K. W.; Nørskov, J. K. *J. Phys. Chem. Lett.* **2012**, *4*, 222.

(195) Tritsaris, G.; Greeley, J.; Rossmeisl, J.; Nørskov, J. K. *Catal. Lett.* **2011**, *141*, 909.

(196) Bezemer, G. L.; Bitter, J. H.; Kuipers, H. P. C. E.; Oosterbeek, H.; Holewijn, J. E.; Xu, X.; Kapteijn, F.; van Dillen, A. J.; de Jong, K. P. *J. Am. Chem. Soc.* **2006**, *128*, 3956.

(197) den Breejen, J. P.; Radstake, P. B.; Bezemer, G. L.; Bitter, J. H.; Frøseth, V.; Holmen, A.; Jong, K. P. d. *J. Am. Chem. Soc.* **2009**, *131*, 7197.

(198) Argo, A. M.; Odzak, J. F.; Gates, B. C. *J. Am. Chem. Soc.* **2003**, *125*, 7107.

(199) Jacobsen, C. J. H.; Dahl, S.; Hansen, P. L.; Törnqvist, E.; Jensen, L.; Topsøe, H.; Prip, D. V.; Møenshaug, P. B.; Chorkendorff, I. *J. Mol. Catal. A: Chem.* **2000**, *163*, 19.

(200) Subramanian, V.; Wolf, E. E.; Kamat, P. V. *J. Am. Chem. Soc.* **2004**, *126*, 4943.

(201) Guczi, L.; Beck, A.; Pászti, Z. *Catal. Today* **2012**, *181*, 26.

(202) Ishida, T.; Kinoshita, N.; Okatsu, H.; Akita, T.; Takei, T.; Haruta, M. *Angew. Chem. Int. Ed.* **2008**, *47*, 9265.

(203) Cunningham, D. A. H.; Vogel, W.; Kageyama, H.; Tsubota, S.; Haruta, M. *J. Catal.* **1998**, *177*, 1.

(204) Kumar, S.; Zou, S. *Langmuir* **2009**, *25*, 574.

(205) Overbury, S. H.; Schwartz, V.; Mullins, D. R.; Yan, W.; Dai, S. *J. Catal.* **2006**, *241*, 56.

(206) Haruta, M.; Tsubota, S.; Kobayashi, T.; Kageyama, H.; Genet, M. J.; Delmon, B. *J. Catal.* **1993**, *144*, 175.

(207) Heiz, U.; Sanchez, A.; Abbet, S.; Schneider, W. D. *J. Am. Chem. Soc.* **1999**, *121*, 3214.

(208) Chin, Y.-H.; Iglesia, E. *J. Phys. Chem. C* **2011**, *115*, 17845.

(209) Bond, G. C. *Molecules* **2012**, *17*, 1716.

(210) Kinoshita, K. *J. Electrochem. Soc.* **1990**, *137*, 845.

(211) Mayrhofer, K. J. J.; Blizanac, B. B.; Arenz, M.; Stamenkovic, V. R.; Ross, P. N.; Markovic, N. M. *J. Phys. Chem. B* **2005**, *109*, 14433.

(212) Shao, M.; Peles, A.; Shoemaker, K. *Nano Lett.* **2011**, *11*, 3714.

(213) Nesselberger, M.; Ashton, S.; Meier, J. C.; Katsounaros, I.; Mayrhofer, K. J. J.; Arenz, M. *J. Am. Chem. Soc.* **2011**, *133*, 17428.

(214) Mukerjee, S.; McBreen, J. *J. Electroanal. Chem.* **1998**, *448*, 163.

(215) Corradini, P. G.; Pires, F. I.; Paganin, V. A.; Perez, J.; Antolini, E. *J. Nanopart. Res.* **2012**, *14*, 1080.

(216) Jirkovský, J.; Makarova, M.; Krtil, P. *Electrochem. Commun.* **2006**, *8*, 1417.

(217) Kwon, G.; Ferguson, G. A.; Heard, C. J.; Tyo, E. C.; Yin, C.; DeBartolo, J.; Seifert, S.; Winans, R. E.; Kropf, A. J.; Greeley, J.; Johnston, R. L.; Curtiss, L. A.; Pellin, M. J.; Vajda, S. *ACS Nano* **2013**, *7*, 5808.

(218) Reier, T.; Oezaslan, M.; Strasser, P. *ACS Catal.* **2012**, *2*, 1765.

(219) Park, S.; Xie, Y.; Weaver, M. J. *Langmuir* **2002**, *18*, 5792.

(220) Diao, P.; Zhang, D. F.; Guo, M.; Zhang, Q. *J. Catal.* **2007**, *250*, 247.

(221) Jaramillo, T. F.; Baeck, S.-H.; Cuenya, B. R.; McFarland, E. W. *J. Am. Chem. Soc.* **2003**, *125*, 7148.

(222) Watanabe, M.; Sei, H.; Stonehart, P. *Journal of Electroanalytical Chemistry and Interfacial Electrochemistry* **1989**, *261*, 375.

(223) Merte, L. R.; Behafarid, F.; Miller, D. J.; Friebel, D.; Cho, S.; Mbuga, F.; Sokaras, D.; Alonso-Mori, R.; Weng, T.-C.; Nordlund, D.; Nilsson, A.; Roldan Cuenya, B. *ACS Catal.* **2012**, *2*, 2371.

(224) Firsova, A. A.; Khomenko, T. I.; Il'ichev, A. N.; Korchak, V. N. *Kinet. Catal.* **2011**, *52*, 434.

(225) Liou, Y. H.; Lo, S. L.; Lin, C. J. *Water Res.* **2007**, *41*, 1705.

(226) Ono, L.; Yuan, B.; Heinrich, H.; Roldan Cuenya, B. *J. Phys. Chem. C* **2010**, *114*, 22119.

(227) Croy, J. R.; Mostafa, S.; Heinrich, H.; Roldan Cuenya, B. *Catal. Lett.* **2009**, *131*, 21.

(228) Kuhl, K. P.; Cave, E. R.; Abram, D. N.; Jaramillo, T. F. *Energ. Eviron. Sci.* **2012**, *5*, 7050.

(229) Hori, Y.; Takahashi, I.; Koga, O.; Hoshi, N. *J. Mol. Catal. A: Chem.* **2003**, *199*, 39.

(230) Xu, X.; Vesecky, S.; He, J. W.; Goodman, D. *J. Vac. Sci. Technol., A* **1993**, *11*, 1930.

(231) Xu, X.; He, J.-W.; Goodman, D. W. *Surf. Sci.* **1993**, *284*, 103.

(232) Nørskov, J. K.; Bligaard, T.; Logadottir, A.; Kitchin, J.; Chen, J. G.; Pandelov, S.; Stimming, U. *J. Electrochem. Soc.* **2005**, *152*, J23.

(233) Gupta, N.; Gattrell, M.; MacDougall, B. *J. Appl. Electrochem.* **2006**, *36*, 161.

(234) Ono, L. K.; Roldán-Cuenya, B. *Catal. Lett.* **2007**, *113*, 86.

(235) Eckle, S.; Denkwitz, Y.; Behm, R. *J. Catal.* **2010**, *269*, 255.

(236) Eckle, S.; Augustin, M.; Anfang, H.-G.; Behm, R. J. *Catal. Today* **2012**, *181*, 40.

(237) Eckle, S.; Anfang, H.-G.; Behm, R. J. *Appl. Catal. A: Gen.* **2011**, *391*, 325.

(238) Wang, L.; Yamauchi, Y. *Chem.–Asian J.* **2010**, *5*, 2493.

(239) Malgras, V.; Ataee-Esfahani, H.; Wang, H.; Jiang, B.; Li, C.; Wu, K. C. W.; Kim, J. H.; Yamauchi, Y. *Adv. Mater.* **2016**, *28*, 993.

(240) Li, C.; Malgras, V.; Aldalbahi, A.; Yamauchi, Y. *Chem.–Asian J.* **2015**, *10*, 316.

(241) Bligaard, T.; Nørskov, J. K. *Electrochim. Acta* **2007**, *52*, 5512.

(242) Artrith, N.; Kolpak, A. M. *Nano Lett.* **2014**, *14*, 2670.

(243) Dutta, A.; Kuzume, A.; Rahaman, M.; Vesztergom, S.; Broekmann, P. *ACS Catal.* **2015**, *5*, 7498.

(244) Kortlever, R.; Shen, J.; Schouten, K. J. P.; Calle-Vallejo, F.; Koper, M. T. *J. Phys. Chem. Lett.* **2015**, *6*, 4073.

(245) Kuhl, K. P.; Hatsukade, T.; Cave, E. R.; Abram, D. N.; Kibsgaard, J.; Jaramillo, T. F. *J. Am. Chem. Soc.* **2014**, *136*, 14107.

(246) Li, Y.; Sun, Q. *Adv. Energy Mater.* **2016**, *6*, 1600463.

(247) Lu, Q.; Rosen, J.; Jiao, F. *ChemCatChem* **2015**, *7*, 38.

(248) Kauffman, D. R.; Ohodnicki, P. R.; Kail, B. W.; Matranga, C. *J. Phys. Chem. Lett.* **2011**, *2*, 2038.

(249) Hirunsit, P.; Soodsawang, W.; Limtrakul, J. *J. Phys. Chem. C* **2015**, *119*, 8238.

(250) Rasul, S.; Anjum, D. H.; Jedidi, A.; Minenkov, Y.; Cavallo, L.; Takanabe, K. *Angew. Chem.* **2015**, *127*, 2174.

(251) Guo, X.; Zhang, Y.; Deng, C.; Li, X.; Xue, Y.; Yan, Y.-M.; Sun, K. *Chem. Commun.* **2015**, *51*, 1345.

(252) Plana, D.; Flórez-Montano, J.; Celorrio, V.; Pastor, E.; Fermín, D. J. *Chem. Commun.* **2013**, *49*, 10962.

(253) Kortlever, R.; Peters, I.; Koper, S.; Koper, M. T. *ACS Catal.* **2015**, *5*, 3916.

(254) Watanabe, M.; Shibata, M.; Kato, A.; Azuma, M.; Sakata, T. *J. Electrochem. Soc.* **1991**, *138*, 3382.

(255) Varela, A. S.; Schlaup, C.; Jovanov, Z. P.; Malacrida, P.; Horch, S.; Stephens, I. E.; Chorkendorff, I. *J. Phys. Chem. C* **2013**, *117*, 20500.

(256) Lim, H.-K.; Shin, H.; Goddard III, W. A.; Hwang, Y. J.; Min, B. K.; Kim, H. *J. Am. Chem. Soc.* **2014**, *136*, 11355.

(257) Hansen, H. A.; Shi, C.; Lausche, A. C.; Peterson, A. A.; Norskov, J. K. *PCCP* **2016**, *18*, 9194.

(258) Hirunsit, P. *J. Phys. Chem. C* **2013**, *117*, 8262.

(259) Kim, D.; Resasco, J.; Yu, Y.; Asiri, A. M.; Yang, P. *Nat. Commun.* **2014**, *5*.

(260) Friebel, D.; Mbuga, F.; Rajasekaran, S.; Miller, D. J.; Ogasawara, H.; Alonso-Mori, R.; Sokaras, D.; Nordlund, D.; Weng, T.-C.; Nilsson, A. *J. Phys. Chem. C* **2014**, *118*, 7954.

(261) Monzó, J.; Malewski, Y.; Kortlever, R.; Vidal-Iglesias, F. J.; Solla-Gullón, J.; Koper, M.; Rodriguez, P. *J. Mater. Chem. A* **2015**, *3*, 23690.

(262) Xu, Z.; Lai, E.; Shao-Horn, Y.; Hamad-Schifferli, K. *Chem. Commun.* **2012**, *48*, 5626.

(263) Zhao, W.; Yang, L.; Yin, Y.; Jin, M. *J. Mater. Chem. A* **2014**, *2*, 902.

(264) Lysgaard, S.; Mýrdal, J. S.; Hansen, H. A.; Vegge, T. *PCCP* **2015**, *17*, 28270.

(265) Jia, F.; Yu, X.; Zhang, L. *J. Power Sources* **2014**, *252*, 85.

(266) Schlaup, C.; Horch, S.; Chorkendorff, I. *Surf. Sci.* **2015**, *631*, 155.

(267) Yeh, J. J.; Lindau, I. *At. Data Nucl. Data Tables* **1985**, *32*, 1.

(268) Kuhn, M.; Sham, T. K. *Phys. Rev. B* **1994**, *49*, 1647.

(269) Vitos, L.; Ruban, A. V.; Skriver, H. L.; Kollár, J. *Surf. Sci.* **1998**, *411*, 186.

(270) Jiang, P.; Porsgaard, S.; Borondics, F.; Köber, M.; Caballero, A.; Bluhm, H.; Besenbacher, F.; Salmeron, M. *J. Am. Chem. Soc.* **2010**, *132*, 2858.

(271) Back, S.; Yeom, M. S.; Jung, Y. *ACS Catal.* **2015**, *5*, 5089.

(272) Pareek, A.; Borodin, S.; Bashir, A.; Ankah, G. N.; Keil, P.; Eckstein, G. A.; Rohwerder, M.; Stratmann, M.; Gründer, Y.; Renner, F. U. *J. Am. Chem. Soc.* **2011**, *133*, 18264.

(273) Tsuda, Y.; Oka, K.; Makino, T.; Okada, M.; Dino, W. A.; Hashinokuchi, M.; Yoshigoe, A.; Teraoka, Y.; Kasai, H. *PCCP* **2014**, *16*, 3815.

(274) Liao, H.; Fisher, A.; Xu, Z. J. *Small* **2015**, *11*, 3198.

(275) Volker, E.; Williams, F. J.; Calvo, E. J.; Jacob, T.; Schiffrin, D. J. *PCCP* **2012**, *14*, 7448.

(276) Jovanov, Z. P.; Hansen, H. A.; Varela, A. S.; Malacrida, P.; Peterson, A. A.; Nørskov, J. K.; Stephens, I. E.; Chorkendorff, I. *J. Catal.* **2016**, http://dx.doi.org/10.1016/j.jcat.2016.04.008.

(277) Liu, X.; Wang, A.; Li, L.; Zhang, T.; Mou, C.-Y.; Lee, J.-F. *J. Catal.* **2011**, *278*, 288.

(278) Wang, A.; Liu, X. Y.; Mou, C.-Y.; Zhang, T. *J. Catal.* **2013**, *308*, 258.

(279) Llorca, J.; Dominguez, M.; Ledesma, C.; Chimentao, R. J.; Medina, F.; Sueiras, J.; Angurell, I.; Seco, M.; Rossell, O. *J. Catal.* **2008**, *258*, 187.

(280) Liao, X.; Chu, W.; Dai, X.; Pitchon, V. *Appl. Catal. B: Environ.* **2013**, *142*, 25.

(281) Meitzner, G.; Via, G.; Lytle, F.; Sinfelt, J. *J. Chem. Phys.* **1985**, *83*, 4793.

(282) Verdaguer-Casadevall, A.; Li, C. W.; Johansson, T. P.; Scott, S. B.; McKeown, J. T.; Kumar, M.; Stephens, I. E.; Kanan, M. W.; Chorkendorff, I. *J. Am. Chem. Soc.* **2015**, *137*, 9808.

(283) Kas, R.; Kortlever, R.; Milbrat, A.; Koper, M. T.; Mul, G.; Baltrusaitis, J. *PCCP* **2014**, *16*, 12194.

(284) Ren, D.; Deng, Y.; Handoko, A. D.; Chen, C. S.; Malkhandi, S.; Yeo, B. S. *ACS Catal.* **2015**, *5*, 2814.

(285) Kim, D.; Lee, S.; Ocon, J. D.; Jeong, B.; Lee, J. K.; Lee, J. *PCCP* **2015**, *17*, 824.

(286) Mistry, H.; Varela, A. S.; Bonifacio, C. S.; Zegkinoglou, I.; Sinev, I.; Choi, Y.-W.; Kisslinger, K.; Stach, E. A.; Yang, J. C.; Strasser, P.; Roldan Cuenya, B. *Nat. Commun.* **2016**, *7*, 12123.

(287) Croy, J. R.; Mostafa, S.; Hickman, L.; Heinrich, H.; Roldan Cuenya, B. *Appl. Catal. A: Gen.* **2008**, *350*, 207.

(288) Mistry, H.; Behafarid, F.; Reske, R.; Varela, A. S.; Strasser, P.; Roldan Cuenya, B. *ACS Catal.* **2015**, *6*, 1075.

(289) Baturina, O. A.; Lu, Q.; Padilla, M. A.; Xin, L.; Li, W.; Serov, A.; Artyushkova, K.; Atanassov, P.; Xu, F.; Epshteyn, A. *ACS Catal.* **2014**, *4*, 3682.

(290) Manthiram, K.; Beberwyck, B. J.; Alivisatos, A. P. *J. Am. Chem. Soc.* **2014**, *136*, 13319.

(291) Chen, C. S.; Handoko, A. D.; Wan, J. H.; Ma, L.; Ren, D.; Yeo, B. S. *Catal. Sci. Tech.* **2015**, *5*, 161.

(292) Roberts, F. S.; Kuhl, K. P.; Nilsson, A. *Angew. Chem.* **2015**, *127*, 5268.

(293) Sen, S.; Liu, D.; Palmore, G. T. R. *ACS Catal.* **2014**, *4*, 3091.

(294) Li, C. W.; Ciston, J.; Kanan, M. W. *Nature* **2014**, *508*, 504.

(295) Varela, A. S.; Kroschel, M.; Reier, T.; Strasser, P. *Catal. Today* **2016**, *260*, 8.

(296) Kas, R.; Kortlever, R.; Yılmaz, H.; Koper, M.; Mul, G. *ChemElectroChem* **2015**, *2*, 354.

(297) Schouten, K. J. P.; Gallent, E. P.; Koper, M. T. *J. Electroanal. Chem.* **2014**, *716*, 53.

(298) Lee, S.; Lee, J. *ChemSusChem* **2015**.

(299) Shibata, H.; Moulijn, J. A.; Mul, G. *Catal. Lett.* **2008**, *123*, 186.

(300) Zhang, Y.-J.; Peterson, A. A. *PCCP* **2015**, *17*, 4505.

(301) Nie, X.; Griffin, G. L.; Janik, M. J.; Asthagiri, A. *Catal. Commun.* **2014**, *52*, 88.

(302) Le, M.; Ren, M.; Zhang, Z.; Sprunger, P. T.; Kurtz, R. L.; Flake, J. C. *J. Electrochem. Soc.* **2011**, *158*, E45.

(303) Menard, L. D.; Xu, F.; Nuzzo, R. G.; Yang, J. C. *J. Catal.* **2006**, *243*, 64.

(304) Zou, J.-J.; Liu, C.-J.; Zhang, Y.-P. *Langmuir* **2006**, *22*, 2334.

(305) Zhou, Y.; Holme, T.; Berry, J.; Ohno, T. R.; Ginley, D.; O'Hayre, R. *J. Phys. Chem. C* **2009**, *114*, 506.

(306) Calle-Vallejo, F.; Koper, M. *Angew. Chem.* **2013**, *125*, 7423.

(307) Montoya, J. H.; Shi, C.; Chan, K.; Norskov, J. K. *J. Phys. Chem. Lett.* **2015**.

(308) Baruch, M. F.; Pander III, J. E.; White, J. L.; Bocarsly, A. B. *ACS Catal.* **2015**, *5*, 3148.

(309) Chen, Y.; Kanan, M. W. *J. Am. Chem. Soc.* **2012**, *134*, 1986.

(310) Lee, S.; Kim, D.; Lee, J. *Angew. Chem.* **2015**, *127*, 14914.